A SEAGLIDER'S VIEW OF HAWAI'I

A THESIS SUBMITTED TO THE GRADUATE DIVISION OF THE UNIVERSITY OF HAWAI'I AT MĀNOA IN PARTIAL FULFILLMENT OF THE REQUIREMENTS FOR THE DEGREE OF

MASTER OF SCIENCE

IN

OCEANOGRAPHY

MAY 2015

By
Kelly A. Pearson

Thesis Committee:

Glenn Carter, Chairperson
Roger Lukas
Bo Qiu

Abstract

Wind Driven Currents South of Oahu

Variation in the waters off the south shore of Oahu and near Station ALOHA have been observed. Both high salinity anomalies (≤ 35.2) and water properties from varying source regions are investigated using Seaglider data. Observed salinity anomalies that can exceed the average profile by up to 0.3 occur approximately once a month and exist in the upper 50 m of the water column. Anomalies coincide with the presence of a cyclonic eddy both north and south of the main Hawaiian Islands. The eddy south of the islands outcrops the $100 - 120$ m isotherms lifting high salinity water (subsurface salinity maxima) to the surface. Eddy interaction and eddy-island interaction cause deformation of the cyclonic eddies resulting in advection of the high salinity water away from the eddy, along equipotential surfaces, into the study site.

For two sites (PacIOOS and ALOHA), the mean regional profiles calculated by Lumpkin [1998] were compared to observed T-S relationships. A RMS calculation was used to identify regions with the most similar water properties. While the entire profile is used in the comparison, most of the variation is in the upper waters (especially at ALOHA) with a secondary STD maximum at PacIOOS at the salinity minimum. Surprisingly, variation indictive of multiple source regions was found at both sites. Of particular interest, most of the observed water properties at PacIOOS (60%) match those found north of the islands. HYCOM 1/12 degree model velocities were used to assess flow in the region and possible advective pathways for the observed T-S curves.

Acknowledgements

I would like to thank my committee for all of their help in doing this research. In particular, I would like to thank Dr. Glenn Carter for always being a calm in the storm, as well as a backboard to bounce ideas off. Also, many thanks to Dr. Roger Lukas for his enthusiasm and dedication to knowledge and research. I can only hope to reach your expertise while maintaining such high levels of joy and interest.

Thank you Dr. Randall Scalise and Dr. Robert Kehoe for putting me on the path of research. I wouldn't have found such joy in science with out your guidance.

Thank you to Lora Van Uffelen, Fernando Santiago-Mandujano, Brian Powell, and James Potemra for their time, assistance, and discussions. Dave Karl and Steve Poulos for collecting the ALOHA Seaglider data. Katie, and Gen for an outlet from work.

Finally, thank you to my Hawaii family: Alex, Michelle, Angela, Jojo, and Dave. You all have been so kind with your time and energies. Alex and Michelle, thank you for always having prosciutto or ice cream. Dave, Angela, and Jojo thank you for giving me good laughs, free food, and warm homes.

Joseph, you've been wonderful at taking my mind off problems and providing time away from work. I always appreciate your perspective and the joy you bring to life.

Lucille, thank you for the long conversations and laughter. Although you never seemed to understand what I was talking about, you tried really hard to make it seem like you did. A sister could never ask for more.

Finally, parents, thank you for always being supportive. I couldn't imagine traveling on this journey with out the two of you and your ever present pride and joy. You both provide the best examples of success in work and in life, thank you for showing me what life can be.

...

Contents

TABLE 1: Definitions of all acronyms used throughout the thesis.

ACRONYM	DEFINITION
ADCP	Acoustic Doppler Current Profiler
ALOHA	A long-term Oliogotrophic Habitat Assessment
AUV	Autonomous Underwater Vehicle
CT	Conductivity-Temperature
CTD	Conductivity-Temperature-Depth
ECMWF	European Center for Medium-Range Weather Forecasts
GFDL	Geophysical Fluid Dynamics Laboratory
GPS	Global Positioning System
HLC	Hawaiian Lee Current
HLCC	Hawaiian Lee Counter Current
HOT	Hawaii Ocean Time-series
HYCOM	Hybrid Coordinate Ocean Model
IOOS	Integrated ocean observing system
NCEP	National Centers for Environmental Prediction
NCODA	Navy coupled ocean data assimilation
NEC	North Equatorial Current
NHRC	North Hawaiian Ridge Current
NPIW	North Pacific Intermediate Water
NRL NCOM	Naval Research Laboratory Naval Coastal Ocean Model
PacIOOS	Pacific Islands integrated ocean observing system
P-E	Precipitation minus Evaporation
RMS	Root mean square
ROMS	Regional ocean model system
SBE	Sea-Bird Electronics
SODA-POP	Simple Ocean Data Assimilation-Parallel Ocean Program
SSH	Sea Surface Height
SSS	Sea Surface Salinity
SST	Sea Surface Temperature
SSW	Subtropical Subsurface Waters
STC	Subtropical cell

Continued on next page.

Table 1 – *Continued from previous page*

Acronym	Definition
T-S	Temperature-Salinity
WOA	World Ocean Atlas
XBT	Expendable bathythermograph

List of Figures

List of Tables

With love for my family.

Chapter 1

Introduction

The Hawaiian Islands are located in a highly variable region of the North Pacific Ocean. The region is known to have high levels of eddy activity [Chelton et al., 2007; Yoshida et al., 2011], as well as, complex currents flowing around the islands and through their associated channels. Additionally, the islands are located within a North-South decreasing (increasing) salinity (temperature) gradient, which spanning from the surface down to the thermocline. All of these can affect the distribution of temperature and salinity found around Hawaiian Islands.

With the objective of understanding the water properties and their variations in the waters surrounding the island of Oahu, this work focuses on Seaglider data from two locations, referred to as ALOHA and PacIOOS, spanning from 2008-2013. The ALOHA site is north east of Station ALOHA, approximately 100 km north of Oahu. The PacIOOS site is south of Oahu situated between Mamala Bay and

Penguin Bank and is a component of the IOOS which covers all US territories in the Pacific. Each of these regions beyond simply having different water properties are dominated by distinct mesoscale systems.

Several regional studies have been attempted in detail to gain insight into the water properties surrounding the Hawaiian Islands [Alford et al., 2006; Dickey et al., 2007; Eich et al., 2004; Lukas and Santiago-Mandujano, 2001, 2008; Lumpkin, 1998] but a comprehensive look at these small-scale regions or a direct comparison north and south of the islands has not been attempted. Here we use the detailed description of the regions provided by the Seaglider to look at the two regions individually and comparatively. Variations are analyzed in detail to provide potential physical processes. Chapter 2 elaborates on the region, and physical processes scaling down from the mesoscale (eddies and currents) to anomalies. Chapter 3 further describes the plethora of data and model results used with an in-depth description of the Seaglider. Chapter 3 also discusses the methods used to analyze the data. Chapter 4 describes the anomalies and trends observed in the data, information about temporal and spatial variation, and a summary of the observations extended over the entirety of the year. Chapter 5 summarizes the regional variations, discusses the implications for the extent of the Hawaiian Islands region, and how well the instrument works for regional observations.

Chapter 2

Scientific background

2.1 Hawaiian Islands Region

The Hawaiian Archipelago consists of eight major islands and numerous atolls and spans 2400 km WNW from the island of Hawaii to Kure Atoll. Land outcrops with the islands predominantly in the southeast, near the main Hawaiian Islands. The ridge is considered porous above the 500 m isobath [Roden, 1991]. The Hawaiian ridge is located in the North Pacific Subtropical Gyre where surface tropical waters are more dense than waters to the south. After initially traveling north, because of Ekman transport, these higher density waters subduct under the less dense waters as they travel south-southwest. The water masses formed via subduction include central waters and subtropical underwaters, which has a salinity maximum formed from the central subtropical gyre E-P max waters.

A salinity gradient spanning from the surface high salinity pool at approximately 30°N to fresher waters south of the islands, sets up a region of spatially distinct T-S curves around the Hawaiian Islands [Lumpkin, 1998]. Large T-S differences are observed between $5° \times 10°$ subregions (Fig. 2.1; Lumpkin [1998]). South of the Hawaiian Islands (Fig. 2.1: panels 16 - 25) have less NPIW due to the existence of modified NPIW (salinity maximum at $\approx 8°$C).

There are nine channels in the main Hawaii Island chain. From north to south they are Alalakeiki, Kealaikahiki, Auau, Pailolo, Kaulakahi, Ka'ie'ie, Kaiwi, Kawai and Alenuihaha channels (Fig. 2.2). The PacIOOS Seaglider path is located at the base of the Kaiwi channel (Fig. 2.2 insert). Satellite sea surface contours as well as model output show eddies interacting through the Kaiwi channel.

Mamala Bay spans from Barbers Point in the west to Diamond Head in the east (Fig. 2.2 insert), with average depths of between 400 and 500 m, and a ridge to the west. Previous studies [Hamilton et al., 1995; Eich et al., 2004; Alford et al., 2006; Martini et al., 2007] have found central Mamala Bay to have large (35 m amplitude) vertical displacements of the isopycnals by the internal tide, large baroclinic velocities, energy fluxes, elevated dissipation rates and partially standing waves. Semi-diurnal internal tides are generated at the Kaena Ridge and off Makapuu. It is waves from these two sources that converge in Mamala bay [Martini et al., 2007; Carter et al., 2008]. Kaiwi Channel, the channel between Oahu and Molokai, is 26 miles wide and 700 m deep . The channel has a subinertial flow of ≈ 6 cm/s.

The second Seagilder location was Station ALOHA, located $\approx$ 100 km north of Oahu where the ocean depth is $\approx$ 4800 m. Station ALOHA is a 6 nautical mile radius circle centered at 158°W, 22.75°N. A long term time-series (Hawaii Ocean Time-series) consisting of approximately monthly shipboard observations is taken at Station ALOHA. Additionally there is also the long term WHOTS mooring and occasionally Seaglider missions. Previous studies have looked at eddies in the region [Nolan, 2008; Lukas and Santiago-Mandujano, 2001], as well as water masses [Lumpkin, 1998; Lukas and Santiago-Mandujano, 2008].

2.1.1 Water masses

A water mass is a volume of water with a common formation history. Almost all are formed by surface processes in specific locations, sink, displacing or interleaving with neighboring water masses. Generally, water mass movement occurs slowly, allowing an image of the ocean circulation to be formed by mapping water properties [Tomczak and Godfrey, 1994].

Water masses commonly found near the Hawaiian Islands are described below.

North Pacific Tropical Water (NPTW) is found between 100 and 200 m depth, with a temperature signature of about 20°C and a salinity above 34.5 [Tomczak and Godfrey, 1994]. Surface waters in the northern part of the subtropical gyre are denser than further south. Just south of 30°N evaporation exceeds precipitation causing a high salinity pool at the surface [Tomczak and Godfrey, 1994]. As the higher density waters are advected southward by the anticyclonic circulation of the gyre, they must either change to lower density by increasing temperature and/or decreasing salinity, or slide below the less dense surface waters to the south. The surface waters generally subduct under the fresher less dense waters to the south, reaching depths of 100 m to 120 m south of the Hawaiian Islands and 100 m to 140 m at Station ALOHA [Suga et al., 2000]. Interannual variations resulting from ENSO can cause formation of NPTW at Station ALOHA resulting in high salinity waters in the surface mixed layer [Lukas and Santiago-Mandujano, 2008].

Eastern North Pacific Subtropical Mode Water (ESMW) is fresher than NPTW and is found between 24 and 25.4 σ_θ. At Station ALOHA either ESMW and NPTW can exist in the near surface. ESMW is formed in 25 - 30°N, 135 - 140° [Hautala and Roemmich, 1998; Hosoda et al., 2001].

Shallow Salinity Minima (SSM) is formed between 35 and 50°N, and 145 - 160°W in between 25.1 and 26.2 σ_θ and are carried by the California Current and NEC to Hawaii. At Station ALOHA, SSM are found above the salinity minimum of NPIW and act as a bridge between NPIW and NPTW [Fiedler and Talley, 2006; Yuan and Talley, 1992].

North Pacific Intermediate Water (NPIW) has temperatures between 6° and 12°C and salinities as low as 34. Originally it was hypothesized that NPIW's low salinity and high oxygen signature were attained through direct ventilation in the

Okhotsk Sea by means of sea ice formation [Wust, 1930]. More recently NIPW has been found to form east of Japan, between the Kuroshio and Oyashio waters. The water is formed through the mixing of relatively fresh, recently ventilated Oyashio water formed in the subpolar gyre and high salinity, low oxygen, Kuroshio water, resulting in a salinity minimum [Shimizu et al., 2004; Talley et al., 1995].

Modified North Pacific Intermediate Water (Modified NPIW) is identified as a salinity maximum of about 34.7 at 10°C. Modified NPIW was first identified by Wyrtki [1977] who hypothesized this water is formed through mixing of NPIW with AAIW in the North Equatorial Current/Countercurrent region. Lumpkin [1998] found the presence of modified NPIW at 20°N, 150°W and between 20°N and 10°N, 140°W and 180°W.

2.1.2 Currents

Emery and Dewar [1982] suggested the islands directly affect the wind-driven subtropical gyre as they are located near the latitude where the North Pacific Subtropic Gyre flow turns westward forming the NEC. As the NEC encounters with the Big Island it bifurcates forming two currents [Roden, 1991]. The northern branch, NHRC, travels along the island ridge to Kauai where it turns westward [Mysak and Magaard, 1983; White, 1983; Roden, 1980; Talley and de Szoeke, 1986]. The NHRC is highly variable pseudo-western boundary current dominated by mesoscale eddies with no prominent annual cycle [Price et al., 1994; Bingham, 1997; Qiu et al., 1997; Firing, 1996]. The southern branch (HLC), running between the southern edge of the islands and the northern edge of the cyclonic equatorial gyre, can accelerate up to speeds of 20 cm/s south of the Big Island [Lumpkin, 1998]. The NHRC joins with the HLC (after flowing around Kauai and Ni'ihau) to form a narrow westward current at 22°N. The HLCC flows along the northern edge of the North Equatorial Ridge at 19.5°N, between $160° - 168°$W, at speeds of up to 10 cm/s [Latham, 1967], separating the mean paths of cyclonic and anticyclonic eddies [Lumpkin, 1998]. Seasonal and inter annual timescale variations in strength and location ($19 - 20°$N) occur in response to changes in the wind stress field [Kobashi and Kawamura, 2002; Yoshida et al., 2011], and the zonal extent of the HLCC varies amongst studies [Qiu et al., 1997; Yu et al., 2003; Xie et al., 2001; Lumpkin and Flament, 2013].

2.1.3 Wind

The pressure gradient between the East Pacific High and the Inter-Tropical Convergence Zone that causes trade winds is distorted by the islands' orography creating areas of positive and negative vorticity in the island lees [Patzert, 1968; Chavanne et al., 2002; Trujillo, 2014]. The surface wind vorticity forms cyclonic and anticyclonic eddies that can dominate the regional flow patterns [Price et al., 1994] (described in more detail in Section 2.2.1).

2.1.4 Rain

Orographic rainfall associated with the trade winds occurs in all seasons, with middle-latitude storms primarily occurring in the winter and tropical systems producing rainfall summer through fall. These winter rains are negatively correlated to the latitude and strength of the jet stream, while summer rains are not correlated to the jet stream.

2.1.5 Evaporation

Evaporation is high in the subtropics, due to high winds and temperature, and leads to high salinities at the surface. Evaporation can be calculated using the bulk formula [Gill, 1982]:

$$E = \rho_a C_E |U_{10}| (q_s - q_a) \tag{2.1}$$

where

$C_E = 1.3 \times 10^{-3}$

q_a = specific humidity at the standard level (10 m)

q_s = saturation humidity at sea surface temperature

U_{10} = wind speed at 10 m

ρ_a = density of air at sea level (≈ 1.178 kg/m^3)

2.2 Mesoscale

Mesoscale is defined as comparable to the Rossby radius of deformation (the length scale at which rotational effects become important) for the first baroclinic mode, this is ≈ 100 km. The large scale ocean currents (Section 2.1.2) and eddies (Section 2.2.1) lead to stirring causing filaments of all oceanic tracers including salinity and temperature. The Reynolds-averaged equation shows the contributions of the turbulent motions to the evolution of a tracer [Levy et al., 2012]:

$$\partial_t \bar{C} + \bar{u} \cdot \bigtriangledown \bar{C} = - \bigtriangledown_H \cdot \overline{u'C'} - \partial_z \overline{w'C'} + \partial_z (\overline{k_z \partial_z C}) + \overline{B(C)} \tag{2.2}$$

This is broken down into it's relative contributions of the turbulent motions as follows:

Local time variation + Mean advection = − Mesoscale − Submesoscale + Microscale + Sources and sinks

where

C = the concentration of a tracer averaged over a time/spatial scale larger than mesoscale field

Over bars = time average

$'$ = Eddy fluctuations over spatio-temporal scale

k_z = vertical diffusion coefficient

B(C) = Sources and sinks

2.2.1 Eddies

Hawaii has long been known as a region of high eddy activity. McGary [1951] identified eddies forming in the lee of the Big Island. Data showing eddy activity dates back to the Wind Zone study [Seckel, 1969]. The Hawaiian Islands lie within a band of high SSH variability [Wyrtki, 1975; Aoki and Imawaki, 1996; Qiu, 1999]. Two distinct baroclinic mesoscale eddy regimes exist within a few hundred miles of the islands. Eddies to the north of the islands that have propagated westward into the region or have formed locally, and eddies to the south of the islands have formed in the lee of the Big Island.

These two systems of eddies interact, influencing the local dynamics and water mass properties [Toner et al., 2003; Nof and Simon, 1987; Mied and Lindemann, 1982]. Eddy dynamics are altered in the presence of barriers (such as the Hawaiian Island), producing eddy-island interactions as well as preventing direct eddy-eddy interaction [Calil et al., 2007; Patzert, 1968]. Due to the islands blocking direct interaction of the two eddy systems, the eddies are limited to interacting through the channels between the islands [Lumpkin, 1998; Jia et al., 2011; Leonardi et al., 1998; Price et al., 1994; Patzert, 1968].

Cushman-Roisin [1994] defines an eddy as a closed circulation in which the rotational period of a parcel of water is shorter than the lifetime of the structure. Cyclonic eddies rotate: counterclockwise in the northern hemisphere and clockwise in the southern hemisphere, in association with a negative sea level anomaly. The core of cyclonic eddies have shallower the isopycnals relative to the surrounding environment, known as doming of the isopycnals. Anticyclonic eddies rotate clockwise in the northern hemisphere and counterclockwise in the southern hemisphere in conjunction with a positive sea level anomaly. Anticyclonic eddies have isopycnals that are deeper relative to the surrounding environment, known as bowling of the isopycnals. Mesoscale eddies can have significant localized impacts [Lumpkin, 1998], as they transport momentum, salinity, and heat and are an important means of transporting energy [Tomczak and Godfrey, 1994]. Eddies are also important for the large-scale heat budgets [Roemmich and Gilson, 2001], as they traverse the ocean eddies are able to advect water mass properties far from their generation region [McDonald, 1999].

Following Tropea et al. [2007], eddies are defined as having an overall SSH change of 10 cm across the radius of the eddy. A cyclonic, or cold core, eddy is identified by a negative SSH anomaly and occasionally a low SST in its core due to the doming of cold waters from below. An anticyclonic, or warm core, eddy can be identified by a positive SSH anomaly, and occasionally by increased temperature.

2.2.1.1 Eddy evolution

There are three phases of an eddy's life cycle: generation, maturity and decay. Eddy generation, or spin-up, can occur from multiple mechanisms such as oceanic flow around a barrier, wind shear due to atmospheric flow around an atmospheric barrier, flow instabilities (e.g. Gulf Stream meanders) and flows over seamounts. Of particular relevance here, deformation of wind blowing around mountains (the Big Island and Maui) can create surface currents that cause localized convergence or divergence of surface waters leading to eddy formation [Yoshida et al., 2010; Jia et al., 2011; Calil et al., 2007]. The center of the eddy sometimes maintains the water properties of the formation region, and the associated transport is known as bolus transport [Lukas and Santiago-Mandujano, 2001; Nolan, 2008]. While bolus transport occurs in both cyclonic and anticyclonic eddies, at Station ALOHA it is only observed in anticyclonic eddies [Nolan, 2008]. A possible explanation is that anticyclonic eddies are more stable (pressure gradient and centrifugal forces are balanced by the Coriolis force) than cyclonic eddies (pressure gradient force is balanced by coriolis and centrifugal forces), and the more stable setup (anticyclone) is able to maintain the water signature longer. Maturity is reached when the eddy reaches quasi-geostrophic* balance. During the decay phase, the eddy spins down and its energy transfers into smaller scales where it can be dissipated [Nolan, 2008].

2.2.2 Lee eddies

Eddies are formed in the lee of the Big Island of Hawaii approximately once a month and have been the focus of a number of papers [eg. Patzert, 1968; Lumpkin, 1998]. Most of the eddies in the region just south of the Hawaiian islands, both

*Quasi-geostrophic motion occurs when flow is nearly geostrophic and the advective derivative terms (momentum equation) are an order of magnitude smaller than the Coriolis and the pressure gradient forces.

cyclonic and anticyclonic, have been formed in the lee of the Big Island. Yoshida et al. [2010] identify two regions of eddy formation: a region directly adjacent to the lee of the island and a region at about 160°W (south of Kauai). In the lee of the Big Island, formation occurs almost year round due to the consistency of the trade winds [Sanderson, 1993]. A typical radius of lee eddies is between 40 and 150 km [Lumpkin, 1998]. Currents within the eddy reach velocities up to 100 cm/s [Nencioli et al., 2008]. Cyclonic eddies formed in the lee of the big island fall into one of three categories: propagating northwestward [Lumpkin, 1998; Calil et al., 2007], nearly stationary [Dickey et al., 2007; Patzert, 1968], and southward propagating [Dickey et al., 2007; Patzert, 1968]. The life span of lee cyclonic eddies is a month to several months, including spin-up. At times, inconsistent generation conditions cause an eddy to decay during the spin-up phase.

In 2005, the E-Flux experiment [Nencioli et al., 2008] attempted to quantify the physical and biogeochemical interactions within cyclonic eddies formed in the lee of the Big Island throughout their lifetimes. The experiment consisted of three phases studying different eddies. Temperature, salinity, current, optical and biogeochemical profiles were made. During the portion of E-Flux looking at a mature quasi-stationary eddy (E-FLUX III), a survey of six cross-center transects, a time series in the center of the eddy, and a time series outside the eddy were made across a mature eddy. Depth profiles of temperature, salinity, and density showed doming of isothermals, isohalines and isopycnals. Isopycnals with background depths of $100 - 120$ m were observed to outcrop, lifting water to the surface [Nencioli et al., 2008] (Fig. 2.3). During CTD cross-sections a +0.3 anomaly at the surface and a corresponding −0.2 anomaly at the subsurface salinity maxima were observed.

At the start of E-Flux III, the eddy was stationary and in solid body rotation†. During solid-body rotation eddy waters are isolated from surrounding waters. A week into the experiment, the eddy started to move from its position adjacent to Hawaii, and subsequently started to spin down from solid body rotation.

2.2.3 Eddies north of the Islands

There is limited literature describing the eddies north of the islands. Mitchum [1996] using the first two years of Topex/Poseidon data, was able to identify a signal of periodicity 100 days propagating north of the Hawaiian Islands. Nolan [2008], using gridded maps of merged satellite altimitry and an eddy identification and tracking algorithm [Chelton et al., 2007], found the periodicity to be 90 days. The average radius of northern eddies was 100 km, with a westward propagation of approximately 6 cm/s [Nolan, 2008; Gill, 1982]. They can be cyclonic or anticyclonic and last from $70-90$ days [Nolan, 2008] . Nolan [2008] found no significant difference between cyclonic and anticyclonic eddies characteristics. The direction of eddy rotation seems to alternate between groups of eddies: multiple cyclonic

†Solid body rotation occurs when the period of rotation of all particles in the vortex and around the vortex center are the same. Then, the angular velocity is proportional to the radius of the streamline for any point in the vortex. All fluid particles in the vortex have constant vorticity and behave as a rigid, rotating solid, hence solid-body rotation [Lumpkin, 1998; Kundu and Cohen, 2004].

eddies occur followed by multiple anticyclonic eddies. These eddies are primarily caused by baroclinic instabilities [Bernstein and White, 1974; Wyrtki, 1982].

Eddies north of the islands are baroclinic and have maximum isopycnal displacement around 1000 m depth [Nolan, 2008]. From 1988 through 2008 the most extreme doming observed was 60 m with no outcropping at the surface and the most intense bowling was 90 m [Nolan, 2008]. The doming or bowling of the isopycnals due to the passage of one of these eddies is not as large as the doming or bowling of the isopycnals due to the lee eddies.

2.2.4 Eddy-eddy interaction

Interactions amongst eddies are highly nonlinear and complex, and can determine how and where eddies will redistribute heat, momentum and water-mass characteristics during their life cycle [Mied and Lindemann, 1982]. They can also have significant impacts on eddy propagation [Cresswell, 1982]. The majority of the time, eddy energy is transferred down to smaller scales, but in the case of eddy-eddy interaction is it quite common for energy to transfer to larger scales.

Vorticies interact through filamentation and submesoscale processes. The distance between eddies for eddy-eddy interaction varies based on eddy size, rotational velocity, eddy life phase, and position relative to the islands and other eddies. Two eddies located north and south of the islands interact resulting in a deformation of all involved eddies, or the translational speed of the eddies will be affected while maintaining their shape [Nolan, 2008]. The shape of the eddies are maintained if the shear strain rate ($\frac{dv_x}{dy}$) between features is less than the rotational velocity inside of the vortex. Otherwise, the shear strain rate describes the deformation of the vortex [McWilliams, 2006].

Eddy-eddy interaction causes the eddy system to deviate from an equilibrium. In an effort maintain potential vorticity the system the eddy can return to its original latitude, change its vorticity or stretch/shrink. It is possible for mass to be exchanged between two eddies but this results in an extreme deformation. Toner et al. [2003] used chlorophyll as a tracer for eddy-eddy advection. The eddies interact and create hyperbolic trajectories stretching the water parcels along one axis and compressing along the other axis. These material curves are called the inflowing and outflowing manifolds, respectively [Berfloff et al., 2002; Carstoiu, 1954; Jones and Winkler, 2000].

Currently, the only research on eddy-eddy interaction in the Hawaiian Islands region is by Jia et al. [2011]. Numerical simulations showed that interaction of a northern anticyclonic eddy and the formation of a southern cyclonic eddy, through the Alenuihaha Channel, increased the strength of the southern eddy. They also showed eddy-eddy interaction occurs through channels further up the island chain.

2.2.4.1 Filamentation

Toner et al. [2003] found inter-eddy advective transport provides pathways for chlorophyll to transit between two interacting eddies. In the Gulf of Mexico, they found inter-eddy advection events had a timescale of approximately ten days. By limiting the pathways available for eddy-eddy interaction, the channels between the islands, restrict the time scales associated with inter-eddy advection. Both eddy systems are propagating westward [Nolan, 2008; Lumpkin, 1998] albeit at different speeds. The simultaneous westward propagation allows for multiple eddy interactions in the region, as well as, varying interaction time scales dependent on relative positioning, westward velocity and channel size. This interaction creates a means for transfer of momentum and/or mass. As the two eddies interact, angular momentum can be transferred, however the vorticity of the system will attempt to remain constant through changes in relative vorticity and latitude as well as by interacting with the islands.

2.3 Submesoscale

The submesoscale is important for the transfer of energy from the mesoscale to small-scales [Thomas et al., 2008]. It is not fully 3-D, quasi-geostrophic, nor non-hydrostatic. The submesoscale is predominant in the upper ocean due to: lateral density gradients, vertical shear, weak stratification, surface boundary and relatively small rossby radius. The submesoscale has a horizontal scale of $\mathcal{O}(1-10)$ km, a vertical scale of $\mathcal{O}(100)$ m and a time scale of $\mathcal{O}(1)$ day [Levy et al., 2012]. The submesoscale causes enhanced cyclonic and downward velocities resulting in large vertical velocities that cause the transfer of properties and tracers between the surface and interior ocean. The role of the submesoscale has only been recently recognized so the submesoscale term in Eqn. 2.2 does not have a well defined magnitude, distribution, or contribution to the vertical and horizontal fluxes [Levy et al., 2012].

2.4 Anomalies observed around Oahu

Two different means of generating salinity anomalies have been observed around Oahu, one in the lee eddies and the other in the northern eddies. Nencioli et al. [2008] found salinity anomalies to occur during the cross section of an eddy formed in the lee of Hawaii. A region of high negative salinity anomalies (relative to average salinity of all CTD casts made outside of the eddy) (about -0.4) below a shallower region of high positive anomalies (about $+0.2$) were observed near the core. The eddy-induced doming of the isotherms lifted more saline waters to the surface, establishing the shallow region of positive anomaly. Doming of the isotherms also lifted deeper, less saline waters to depths usually occupied by the deep salinity maximum, which produced the deeper region of negative anomalies [Nencioli et al., 2008].

North of Oahu, the anticyclonic eddies are known to maintain bolus transport. Lukas and Santiago-Mandujano [2001] found a high salinity anomaly (relative to the long term mean provided by HOT) which was trapped in the center of anti-cyclonic eddy. They infered that the water trapped in the core during formation was advected from the formation region, off the coast of Mexico, to Hawaii with minimal changes in characteristics.

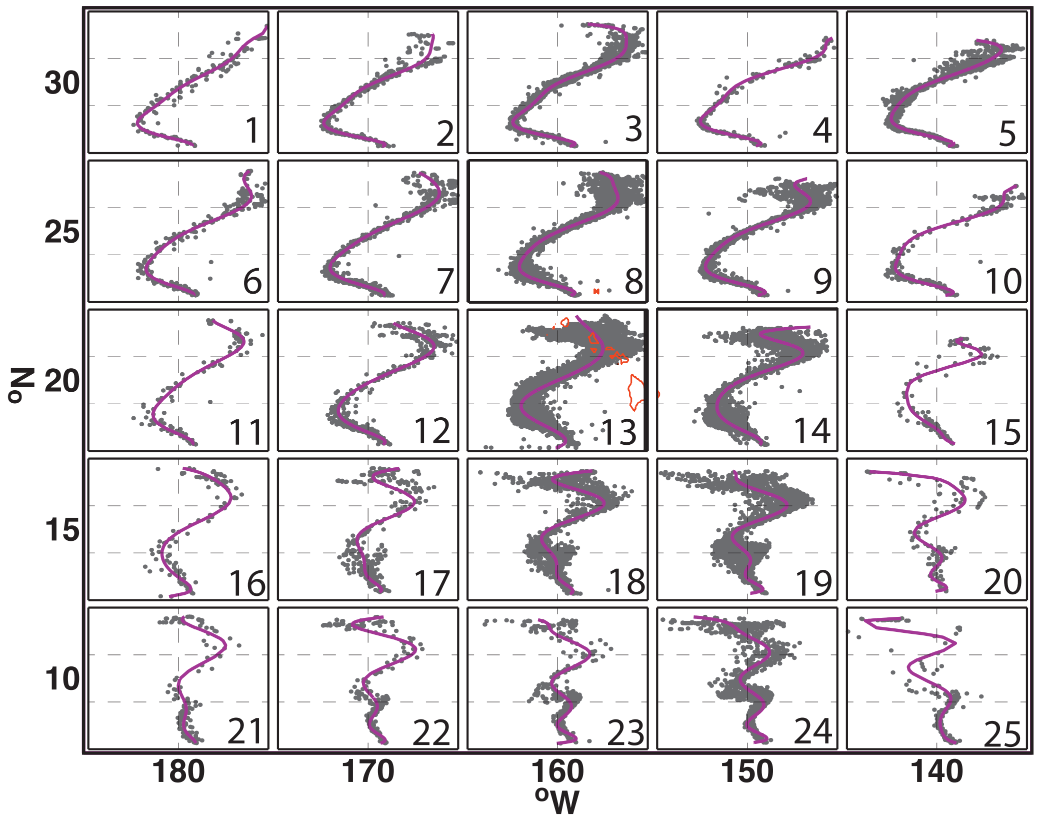

FIGURE 2.1: Lumpkin [1998] calculated the average T-S curve (magenta) for each of the 5° by 10° regions from all CTD profiles available for the region (gray). In each regional cell the two horizontal dashed lines occur at 10° and 20°C and the vertical dashed line occurs at 34.5. The Hawaiian Islands and the two Seaglider nominal routes (red) are plotted in their region to provide a perspective on the distribution of TS curves relative to the regions and their respective water properties. Regions are numbered 1 - 25 row wise from left to right.

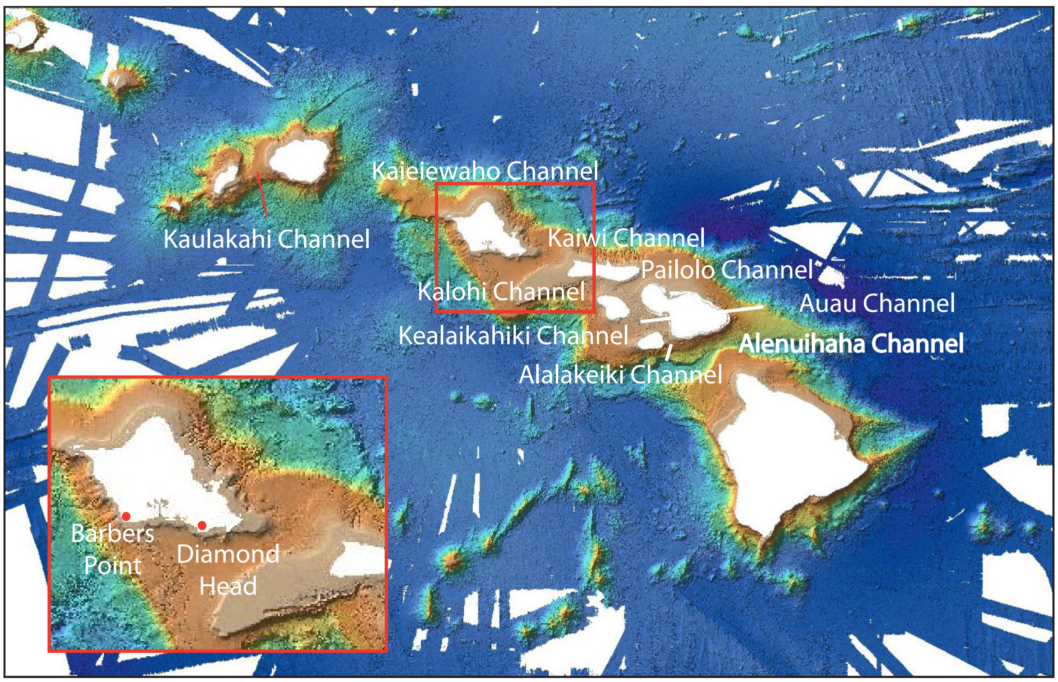

Figure 2.2: The locations of the Hawaiian Island Channels with an insert (red) showing a zoomed in view of Oahu and the Kaiwi channel.

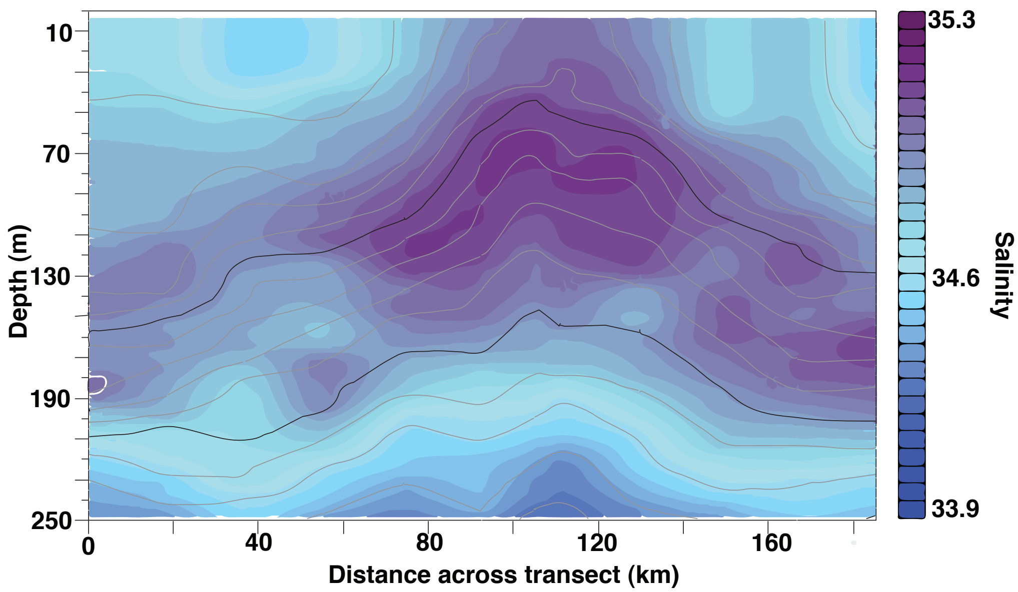

FIGURE 2.3: E-Flux III found the 24.4 σ isotherms, typically found $\approx 100 - 120$m depth, to outcrop near the center of the eddy Nencioli et al. [2008]. Contours (gray) are isotherms on 0.2 intervals while the black contours are 24 and $25\sigma_\theta$, the colors are salinity.

Chapter 3

Methods and Data

3.1 Seaglider

In 1989, Henry Stommel published the Slocum Mission, a short story, [Stommel, 1989], and inspired the fabrication of oceanic gliders as they exist today. Stommel imagined an autonomous underwater vehicle (AUV) that was able to travel throughout the ocean continuously collecting data. Gliders have now been used in studies looking at eddies, biological and physical fronts, in locations such as the West coast, Alaskan coast, Hawaii, and Labrador Sea [Davis et al., 2008; Hatun et al., 2007; Eriksen et al., 2001; Frajka-Williams et al., 2011]. Depending on configuration they can measure temperature, conductivity, fluorescence, sound, or velocity shear, and can derive CHL-a, surface and depth averaged currents, or salinity.

The gliders used in this research are Seagliders, which were designed at the University of Washington [Eriksen et al., 2001], and are approximately 1.8 m long and weigh 52 kg (Fig. 3.1). Like all ocean gliders they are designed to be reuseable and relatively cheap to operate [Eriksen et al., 2001; Davis et al., 2003; Rudnick et al., 2004]. Seaglider motion is controlled by: 1) pumping oil between the pressure case and an external bladder, thereby changing the glider's volume and hence buoyancy; 2) moving the battery along the glider axis to change pitch; and 3) pivoting the battery asymmetrically to turn the glider (roll). Seagliders are programmed to fly in a sawtooth pattern at about half a knot. Seagliders are pressure rated up to one thousand meters.

The Seaglider repeats the same steps (Fig. 3.2) until it is recovered (or reprogrammed), usually because of low batteries:

1. At the surface, the Seaglider downloads any new instructions including waypoints using the Iridium network.

2. A GPS position is taken.

3. Based on estimated currents, the Seaglider calculates the best heading and dive slope to make progress towards the target waypoint.

4. The Seaglider begins the dive (one down then up pattern) cycle by decreasing its volume and adjusting the battery position to achieve the required glide slope. At intervals the glider checks if its heading has deviated from

the target and makes roll corrections as needed. Due to the slow speeds, light weight and sometimes mechanical issues the Seaglider was occasionally pushed off course by the currents.

5. At the target depth the glider pumps oil into the external bladder, adjusts the battery position to be nose up. The PacIOOS Seaglider reached typical depths of 450 m and the ALOHA Seaglider reached depths of 800 m. If its vertical rise rate drops below a user set threshold it will pump more oil.

6. On reaching the surface, the glider orientates itself to have the antenna pointing skyward. A GPS position is taken, before sending and receiving data via satellite. A typical dive lasts 3 hours for the PacIOOS Seaglider and 4.5 hours for the ALOHA Seaglider.

The difference between the two GPS positions, before and after the data transfer, gives an estimate of the surface current, and the difference between the actual surfacing location and one predicted by a flight model algorithm gives an estimate of depth-averaged current. Errors on horizontal speed are $\approx 1 - 1.5$ cm/s [Eriksen et al., 2001]. The Seaglider dead reckons between GPS fixes using pitch, roll, heading. A kalman filter* is used for prediction for mean and oscillatory currents using a sum of the mean, diurnal and semidiurnal components. A target depth is input by the pilot for surface to near-bottom dives.

*A kalman filter is a weighted algorithm using measurements over time to produce an estimate of unknown variables.

The ALOHA data used in this work was collected to give a larger spatial coverage for the HOT (described in section 3.4.3) with crossings occurring approximately every 8 days. The position of the nominal route was chosen to allow the glider path to cross through the ALOHA Station circle but to avoid the WHOTS mooring, the moored profiler, or the a research vessel. The PacIOOS data used in this work was collected for real time assimilation in the PacIOOS ROMS model (described in section 2.3.8). The route off the south shore of Oahu was chosen to avoid the shallows of Penguin Bank and main shipping lanes.

These gliders were equipped with Sea-Bird temperature, conductivity and dissolved oxygen sensors, as well as a WET Labs fluorometer-optical backscatter sensor. Only data from the temperature and conductivity sensors were used in this analysis. The data sampling rate was varied with depth to conserve battery, with one sample every 5 seconds in the upper 30 m and every 10 seconds throughout the rest of the water column. Along with the variable speed of the glider this leads to non-uniform sample spacing in the vertical.

Twelve missions were conducted periodically from 2008 through 2011 (Table 3.1). The majority of the glider missions occurred during the spring and summer months. Only two missions, ALOHA 3 and PacIOOS 4, collected data through the fall.

PacIOOS 1. Data will not be used due to an unresolved 0.5 salinity offset when compared to alternative data: CTD, Argo profiles and later Seaglider missions.

Table 3.1: Seaglider Missions.

	Start Date	End Date
PacIOOS 1	April 10, 2008	May 06, 2008
PacIOOS 2	July 09, 2008	August 20, 2008
PacIOOS 3	April 12, 2010	July 14, 2010
PacIOOS 4	July 27, 2010	November 10, 2010
PacIOOS 5	April 5, 2011	May 24, 2011
PacIOOS 6	June 13, 2011	July 30, 2011
PacIOOS 7	April 25, 2013	July 26, 2013
ALOHA 1	May 31, 2008	July 31, 2008
ALOHA 2	August 13, 2008	October 11, 2008
ALOHA 3	August 13, 2010	November 17, 2010
ALOHA 4	May 10, 2011	August 3, 2011
ALOHA 5	May 23, 2013	September 17, 2013

PacIOOS 2. The glider was deployed for 42 days. The reason for recovery was nearing the end of its battery life. The glider completed 297 dives.

PacIOOS 3. After 94 days the glider was recovered as it was nearing the end of its battery life. The glider completed 749 dives. On dive 514 the WET Labs BB2F-VMG sensor was disabled to conserve power. This mission was also a test of wild life Argo tag as a back up positioning device.

PacIOOS 4. The glider was deployed for 107 days. The reason for recovery was nearing the end of its battery life. The glider completed 877 dives.

PacIOOS 5. The glider went into recovery mode after dive 436 due to the failure of the linear potentiometer on the pitch mechanism and was recovered. The glider was deployed for 52 days. The glider completed 436 dives.

PacIOOS 6. The glider was deployed for 47 days. The reason for recovery was nearing the end of its battery life. The glider completed 499 dives.

PacIOOS 7. The glider was deployed for 93 days. The reason for recovery was a spiraling underwater track. The glider completed 803 dives.

ALOHA 1. The glider was deployed for 62 days. The reason for recovery was nearing the end of its battery life. The glider completed 555 dives.

ALOHA 2. The glider was deployed for 59 days. The reason for recovery was nearing the end of its battery life. The glider completed 493 dives.

ALOHA 3. The glider was deployed for 97 days. The reason for recovery was nearing the end of its battery life. The glider completed 669 dives.

ALOHA 4. The glider was deployed for 86 days. The reason for recovery was nearing the end of its battery life. The glider completed 627 dives.

ALOHA 5. The glider went into recovery mode after dive 478 due to failure of the pitch mechanism after 118 days.

PacIOOS 1 and 2 nominally surveyed a straight line between waypoints (21°01.00'N, 157°46.00'W; 21°10.00'N, 157°56.00'W). PacIOOS 3 through 7 nominally surveyed a triangle with vertices (20°57.92.00'N, 157°49.87'W; 21°05.18'N, 157°42.92'W; 21°08.33'N, 158°02.07'W). ALOHA 1 through 5 nominally surveyed a bow tie with vertices (22°58.12'N, 157°55.12'W; 22°49.12'N, 157°55.12'W; 22°48.36'N, 157°42.00'W;

Table 3.2: Seagiider calibration information. The last two columns refer to the SeaBird TC sensor.

Mission	Glider ID Number	Sensor	Calibration Date
PacIOOS 2	SG139	0066	June 24, 2007
PacIOOS 3	SG139	0066	November 16, 2008
PacIOOS 4	SG139	0066	November 16, 2008
PacIOOS 5	SG139	0143	November 15, 2009
PacIOOS 6	SG523	0154	February 15, 2010
PacIOOS 7	SG523	0073	January 17, 2012
ALOHA 1	SG146	0073	September 24, 2007
ALOHA 2	SG148	0141	September 24, 2007
ALOHA 3	SG146	0141	November 15, 2009
ALOHA 4	SG146	0142	November 15, 2009
ALOHA 5	SG148	0141	June 12, 2013

22°57.36'N, 157°42.00'W). Temperature and salinity from all missions is spatially and temporally aliased.

3.1.1 Calibrations

Table 3.2 lists the Seaglider and sensors used, and the sensor calibration dates. Due to variation in Seagliders, sensors and non-frequent calibration (only PacIOOS 2 and PacIOOS 3 use the same sensor) back calibration is not used. Calibrations occurred at the Seabird facility. Fig. 3.3 and Fig. 3.4 show while there was no significant drift in the conductivity cell, the temperature drift was 3-5 millidegrees.

3.1.2 Biofouling

After each mission the conductivity cells were cleaned of biology using Triton X. Only Seaglider missions that had long periods on the surface due to mechanical failure showed noticeable biological growth. The movement of the glider appears to be sufficient to prevent most biofouling. The PacIOOS missions occurred near the coastal zone, but because of the mission velocities and dive depths the Seaglider was not conducive to biological growth. In addition to deeper dive depths, the ALOHA missions occurred in a oligotrophic zone. The most common interaction between the Seaglider and biology was temporary systematic errors caused by biology passing through the conductivity cell. Several Seagliders experienced a shark attack. An attack on the wing caused the Seaglider to fly abnormally and eventually forced the mission to be aborted, whereas an attack on the fiberglass shell caused increased drag but allowed continuation of the mission.

3.1.3 Pressure sensor

The Paine pressure sensor used on the Seagliders has an error of 0.1% of the pressure sensor full scale. This error is a best estimate as pressure sensors can have larger errors depending on type and calibration. In future Seaglider missions, a log with pressure measurements upon deployment and recovery will recorded. There is an offset between the pressure sensor and the sail that would introduce errors into the measurements.

3.1.4 Timebase

In an experiment using Seagliders equipped with a Seascan in addition to the Seaglider CF2 clock, Uffelen et al. [2013] were able to compare the two time measurements. The Seascan is accurate to 1.5 seconds over the course of a year ($\approx$ 1.1 ms per dive). The comparison between the two measurements (Fig. 3.5) shows $\approx \pm 0.4$ s error over a 400 dive mission, (Van Uffelen, personal communication).

3.1.5 GPS

The Seaglider is equipped with a Garmin 25 HVS with an error of ± 15 m [Garmin, 2000]. The Garmin 25 HVS is only able to take GPS measurements while at the surface. Uffelen et al. [2013] found the models use to predict the glider's position underwater have a RMS error of ± 106 m.

3.1.6 Quality control

Seaglider data varies both in time and space. For example, the data used in this research, measurements were taken every 5 seconds in the upper 30 m and every 10 seconds in the rest of the water column. In addition to variable temporal sampling rates in the vertical, the seaglider is moving horizontally through the water at $\approx$ 15 cm/s. Inconsistency of spacing between data points made it impossible to use methods based on time-domain or frequency-domain filtering (e.g. Seabird's wild-edit routine). I used threshold limits, as well as detection algorithms applied to the raw frequency counts from the Seabird temperature and conductivity sensors. By applying the threshold values and detection algorithm to the raw data, contamination from other measurements is avoided. The most errors occur at the depth extrema, by applying the threshold limits and then the detection algorithm, the efficiency of the detection algorithm is increased. Both temperature and conductivity are nonlinear functions of the sensor output frequencies. Temperature equation is

$$T = \frac{1}{g + h[ln(\frac{f_0}{f})] + i[ln^2(\frac{f_0}{f})] + j[ln^3(\frac{f_0}{f})]}, \tag{3.1}$$

where f is sensor frequency, f_0 is a reference frequency, and g, h, i, j are calibration coefficients. In addition to being a nonlinear function of frequency, conductivity is also a function of temperature and pressure.

$$C = \frac{k + l\omega^2 + m\omega^3 + n\omega^4}{10(1 + \delta t + \sigma p)}, \tag{3.2}$$

Where δ and σ are the thermal coefficient of expansion and bulk compressibility, respectively, ω is sensor frequency, and k, l, m, and n are calibration coefficients. Further, salinity is a nonlinear function of conductivity, temperature, and pressure [Commision, 2010]. Therefore an error in temperature frequency would result in errors in both the salinity and temperature.

The algorithms compare sequential data points. Each up and down is treated individually so as to minimize the effects of periods of no flow through the sensor (e.g. at the surface and at depth). The anomalous data filtering portion of quality control has a few steps that are applied to both temperature and conductivity frequencies. In order of application they are

1. Threshold values - to flag data beyond reasonable ranges of values
2. Spike Method - to flag single anomalous points
3. Plateau Method - to flag adjacent anomalous points, up to 3 adjacent points
4. A comparison of flagged points

Threshold values. This research used frequency counts equivalent to 33.5 and 36 (PacIOOS) and 33.5 and 36.5 (ALOHA) as the thresholds for salinity at and 4°C and 32° for temperature (PacIOOS and ALOHA). These values were chosen to be 0.5 above/below expected salinity extrema for the region between 0 and 450 m and 4°C above and below expected temperature values. Any values that exceed the threshold limits are flagged and set to NaN. The threshold frequencies are calculated by working backward from the temperature and salinity equations. The conversion from threshold values to frequency counts varies from sensor to sensor, as a result threshold limits were recalculated for each mission.

Spike method. This filter compared temporally adjacent points. Points that differ from both adjacent measurements by a user specified amount are flagged. In this research, 30 Hz was used for both conductivity frequency and temperature frequency. Thirty Hz was found to provide the most robust flagging of bad data compared to hand editing. Glider velocity is variable and at times there can be a large difference in temperature and salinity values, especially in the thermocline and pycnocline, between sequential good data points. On the other hand, points can be incorrectly deemed accurate if too large of a adjacent data difference is chosen. The filter was run on temperature and conductivity separately. Points that are found to have both temperature and conductivity frequencies flagged could be due to some physical process, and were kept. For example, large temperature gradients and low sampling frequency can lead to points being flagged in the thermocline, these points are not erroneous and should be kept. Otherwise, points deemed erroneous are set to NaN.

Plateau method. This filter identifies locations where two or three adjacent points differ from the surrounding profile by more than 15 Hz. Again this value was found through trial and error. The remaining process of the plateau portion mirrors the process described in the spike method description.

Overall, this method is successful. When applied to eight different glider missions it flagged approximately 82 percent of points flagged by hand editing. The major errors come from whole portions of the profile that veer off from the general T-S curve (most likely from the glider flying poorly or stalled, and maybe from material being temporarily lodged in the cell), which are easily hand edited. The T-S curve (see Section 3.4) of PacIOOS 3 is shown in Fig. 3.6. Blue dots are the data points that have been flagged by the filter and have been set to NaN. The areas circled in pink are sections of profiles that deviate from the mean profile, these would be hand edited out.

Processing errors

After applying quality control to the raw data, the data is gridded into 2 m spacing in the vertical. To do this, each sloped path (depth/time or depth/distance) is treated as a vertical profile. This introduces spatial and temporal aliasing (from tidal and higher frequency internal waves) into salinity, temperature, and σ_θ. Interpolation processes used do not account for larger gradients in the vertical than the horizontal, and can introduce artifacts into the results.

3.1.7 Data comparison

As an assessment of Seaglider data, Argo profiles from $20-22°$N and $157-159°$W were compared to the contemporary Seaglider profiles. The comparison looks at temperature-depth, salinity-depth, and T-S relationships. The distance between the Seaglider location and the comparable Argo profile is highly variable. In general, the closer the Argo profiler to the Seaglider location the more accurate the comparison of profiles. All available comparisons are shown in Appendix A.

3.1.7.1 Argo

The Argo program was started in 2000, and the complete array was achieved in 2007. At any given time there are over 3000 floats distributed approximately every 3° throughout the world's oceans. Yearly, the floats provide profiles of temperature, salinity, and pressure in the upper 2000 m. All floats are equipped with a pumped CTD with accuracy requirements of 0.005°C for temperature and 0.01 for salinity [Oka and Ando, 2004].

The Argo floats are free drifting, buoyancy controlled, park and profile instruments. The typical floating depth is 2000m. The average sampling rate is once every 10 days. Data is transmitted from the floats via the Argos satellites and iridium systems. Data is available within 12 hours of sampling. Data used in the current research were limited to the years of $2007 - 2013$, latitude of $20° - 22°$N and longitude of $157° - 159°$W. Salinity and temperature profiles during a glider mission were compared to Seaglider data (see Appendix A).

3.1.7.2 Aquarius

SSS estimates are available from the Aquarius satellite system starting on June $10, 2011$ [Vine et al., 2007]. The daily data, used in this research, has a spatial resolution of 100 km and global coverage every 7 days. Data is collected using 3 radiometers and a scatterometer. Nearshore data is inconsistent in availability and at times limits direct comparison. Analysis of satellite data, although imperfect, allowed us to get surface perspectives of the Hawaiian Islands region before, during and after each mission.

The Aquarius sea surface salinity measurements are only available concurrently with PacIOOS 7 and ALOHA 5, April-September 2013. Although gridding is coarse, salinities above 35 in the study region during time periods corresponding to high salinity anomalies in the Seaglider data were observed.

3.1.8 Physical lag and thermal inertia corrections

Conductivity is measured in a volume of water and is temperature dependent ($C = f\ (T,\ S,\ P)$). This means that any differences between the temperature measured by the temperature sensor and the actual temperature within the conductivity sensor lead to salinity and density, errors. There are two primary reasons for an offset: different water parcels being measured at each sensor and the thermal inertial of the conductivity cell itself. The former can be minimized by forcing the same water past the sensors using ducting and a pump. However, in order to maximize battery life the Seagliders use an unpumped, unducted CT system. The latter reason is due to the conductivity cell having a mass and thus storing heat. Heat will flow between the glass and the conductivity cell water sample based on the gradient of the temperature [Lueck and Picklo, 1990; Morison et al., 1994; Mensah et al., 2009]. This error is referred to as thermal inertia or the thermal lag. Corrections have been computed for various instruments, [Garau et al., 2011; Johnson et al., 2007]. Unfortunately at this point in time, no correction is available specifically for the Seaglider. C.C. Eriksen is working on an equation for the correction specifically for Seagliders, (personal communication).

The distinct offset in salinity between the up (blue) and down (black) portions of a dive, Fig. 3.7 (PacIOOS 5) clearly show the presence of some offset beyond expected variations in time or space between adjacent profiles. Figure 3.8 shows an example of the lag (thermal and physical) by comparing adjacent up and down profiles. The temperature/depths plot offset shows the effects of internal waves/tides. In addition to these environmental factors both physical lag and thermal inertia play a role in the offset in the salinity vs. depth plot.

Clearly, thermal inertia and physical lag are affecting the data and a correction needs to be applied. The thermal inertia and physical lag correction needs to be variable based on speed, sampling speed and temperature gradients. Here we use the thermal lag correction described by [Garau et al., 2011] for the Slocum CTD. This method is based of the schemes of Morison et al. [1994]; Mensah et al. [2009].

For each leg, the up and down cast are used as the perimeter of a polygon. The area of the polygon, the area between the up and down dives, is calculated using triangles in order to avoid issues caused by concavity and self-intersections. Using the MATLAB optimization toolbox four parameters: α_0, τ_0, the offsets and α_s, τ_s the slopes are estimated. These are used in the Morison et al. [1994] equations

Table 3.3: Flow velocities for PacIOOS missions

Mission	**Average flow velocity** (cm/s)	**Minimum velocity** (cm/s)	**Maximum velocity** (cm/s)
2	12.48	0.60	31.41
3	15.98	1.59	68.56
4	15.86	0.27	50.54
5	13.70	0.35	50.14
6	17.27	0.64	64.74
7	19.11	0.17	40.97

relating the correction parameters and the flow speed.

$$\alpha(n) = \alpha_0 + \alpha_s V_f(n)^{-1} \tag{3.3}$$

$$\tau(n) = \tau_0 + \tau_s V_f(n)^{-1/2} \tag{3.4}$$

Where the calculated values of α is the amplitude of the error and τ is the time constant. V_f is the velocity of the flow. The variable n is the sample index.

We are able to indirectly calculate the velocity of the Seaglider (V_f) by using the depth integrated current. This current is calculated by subtracting the predicted location, where the glider would surface without any influence by the surrounding water, from the actual location, the initial GPS location measured upon surfacing. We use this perturbation distance over the time of the dive to get the depth integrated velocity. This model is limited to a narrow range of flow speeds. Garau et al. [2011] does not define the span of a narrow range. The average flow speed, minimum and maximum flow speeds for PacIOOS 2 - 7 are listed in Table 3.3.

To estimate the temperature inside of the conductivity cell we use [Garau et al., 2011]

$$T_T(n) = -bT_T(n-1) + a[T(n) - T(n-1)] \tag{3.5}$$

where,

$$a = \frac{4f_n\alpha\tau}{1+4f_n\tau} \tag{3.6}$$

$$b = 1 - \frac{2a}{\alpha} \tag{3.7}$$

Where f_n is the sampling frequency, T_T is the corrected temperature and T is the measured temperature. The correction is subtracted from the measured temperature. The corrected temperature (Fig. 3.10) is used solely for calculating the salinity from the measured conductivity.

A significant improvement is seen, when comparing the uncorrected and corrected salinities (Fig. 3.11). There are a few hours separating the legs of the dive so an exact match is not expected because of internal waves and/or spatial gradients in eddies.

3.2 HYCOM 1/12°

HYCOM is a data-assimilating model with isopycnal-sigma-pressure coordinates. Model output includes temperature, sea surface height, salinity, potential density, and velocity. HYCOM+NCODA Regional 1/12° Forecast for the Main Hawaiian

Islands spans from 170°E to 140.08°W (resolution of 0.08°) and from 10.028°N to 39.915°N, (resolution of 0.071°). In the vertical, the model has variable resolution ranging from 6 m near the surface to 5500 m at depth. The model output has daily temporal resolution. Assimilated ocean observations include GAC/LAC MCSST, Geostationary satellite system, ship based and buoy data from XBT, CTD, Profiling Autonomous Lagrangian Circulation Explorers (PALACE) floats, Sea Surface Height for altimeter and Special Sensor Microwave/Imager for sea ice (see Table 1 for list of acronyms).

HYCOM data covers all 7 missions. Figure 3.9 compares HYCOM [Bleck and Benjamin, 1993] to Seaglider data from PacIOOS 5 in T-S space, and shows large differences in the upper ocean salinity. The largest discrepancies, for all missions, occur at the surface, the subsurface salinity maximum, and at the salinity minimum.

3.3 Lagrangian Model

In order to distinguish the source region (the origin region of a specific set of water properties), a Lagrangian tracer model was developed which used velocities from 1/12 degree HYCOM+NCODA model output. High salinity tracer particles were introduced at the surface, daily, north of 24°N corresponding to where salinities above 35.2 are found in the model. Every 20 minutes, the tracer particles moved according to the corresponding HYCOM velocity field. Velocities changed daily, corresponding to the HYCOM output interval. The equations used in the lagrangian tracer model use the assumption that the velocity is constant for 24 hours, w is ignored and that the distance the particle moved is equal to velocity multiplied by time, i.e., the zonal and meridional positions are given by

$$x^{n+1} = x^n + u(x,y)\Delta t, \quad y^{n+1} = y^n + v(x,y)\Delta t \tag{3.8}$$

respectively. Where u is the zonal velocity and v is the meridional velocity. The assumption that the velocity is constant for 24 hours is necessary due to model output interval limitations of once daily. The assumption that w is ignored is applied to test the null hypothesis: high salinity water is advected along the surface from the formation region to the PacIOOS study site.

A weighted interpolation scheme was used to calculate the velocities in between the HYCOM grid points (Fig. 3.12). Let:

$$g(y) = \left(1 - \frac{y_{max} - y}{y_{max} - y_{min}}\right) \tag{3.9}$$

$$h(y) = \left(1 - \frac{y - y_{min}}{y_{max} - y_{min}}\right) \tag{3.10}$$

$$f(x) = \left(1 - \frac{x_{max} - x}{x_{max} - x_{min}}\right) \tag{3.11}$$

$$j(x) = \left(1 - \frac{x - x_{min}}{x_{max} - x_{min}}\right) \tag{3.12}$$

then,

$$u(x,y) = g(y) * f(x) * u(x_{max}, y_{max}) + f(x) * h(y) * u(x_{max}, y_{min}) + j(x) * h(y) * u(x_{min}, y_{min}) + g(y) * j(x) * u(x_{min}, y_{max}) \quad (3.13)$$

$$v(x,y) = g(y) * f(x) * v(x_{max}, y_{max}) + f(x) * h(y) * v(x_{max}, y_{min}) + j(x) * h(y) * v(x_{min}, y_{min}) + g(y) * j(x) * v(x_{min}, y_{max}) \quad (3.14)$$

Results show that high salinity waters do not advect to the study region along the surface. The model shows surface advection along filaments, and pathways between eddies (submesoscale processes) but the high salinity water does not reach the PacIOOS study region.

3.4 Average salinity and temperature

The distribution of salinity in the ocean varies in time and in space with near surface salinity variation altered through E-P. The E-P distribution closely matches that of the surface salinity [Talley, 2002]. In the subtropics high levels of evaporation lead to high salinities close to the sea surface. Initially these high salinity waters move northward due to Ekman transport, then convergence and equatorward advection along the subtropical gyre cause subduction. Below the near-surface salinity maximum, in the central subtropical gyre, salinity and temperature decrease smoothly to the salinity minimum.

3.4.1 Average profile calculations

The ALOHA site has a long term average profile for temperature and salinity available from the 25 year of HOT data. The PacIOOS site does not have such a data set to use, and in order to identify anomalies an average regional profile needed to be calculated. The low frequency variability in the region due to the eddies caused complications. A comparison of average profiles from glider data, HOT data, mooring data, Argo data, and various models was used to identify the most accurate average profile for the region (Fig. 3.13). This research used the average profiles of salinity and temperature over all six PacIOOS Seaglider missions.

Multiple models have output for the region of the Seaglider. Fig. 3.14 shows a comparison of models (red - ECMWF, green - GFDL, blue - HYCOM, purple - NCEP, pink - NRL NCOM, and orange - SODA-POP) to Seaglider data (grey - all data points from the 6 PacIOOS missions, and black - average profile for all missions). Model results vary. Only two models, ROMS (Section 3.4.2) and HYCOM (Section 3.2), with the spatial and temporal resolution for inclusion in subsequent analysis. Neither of these profiles match observed profiles. Yearly averages of salinity vs. depth profiles are indistinguishable from summer averages.

3.4.2 ROMS

ROMS is a free-surface, terrain-following, primitive equations ocean model. Data is input into the model on a staggered, irregular/curvilinear grid. The output is a 3-hourly forecast with an approximately 4 km distribution.

ROMS [Shchepetkin and McWilliams, 2009] output for Oahu [Matthews et al., 2012] is available from March 2011 until present, and therefore only covers ALOHA 5 and PacIOOS 5, 6, and 7. There are two different model outputs, data assimilating which includes data from the Seagliders and non-assimilating. Fig. 2.5 shows large differences in T-S between ROMS output and the values measured by the Seaglider with the largest difference ($\approx 0.2 - 0.3$) at the coldest temperatures. The non-assimilative data set has a high salinity maximum of approximately 35.6 while the assimilative data set has a salinity maximum of approximately 35.3.

Data is available from March 25, 2011 through June 25, 2013, -163.8°W to -152.5°W and 17.0°N to 23.9°N. ROMS provides a much more high resolution and detailed view of the near shore ocean than HYCOM or satellite data.

3.4.3 Hawaii Ocean Time-series Program (HOT)

HOT is a long term ocean time-series measuring hydrographic, chemical and biological data since October of 1988. Research cruises, including multiple CTD profiles, occur approximately once a month. Station ALOHA, a location of repeated CTD measurements, is located at 22° 45'N, 158° 00'W, 100 km north of Kahuku Point, Oahu in 4800 m of water. Measurements were made using a Sea-Bird SBE-9/11 Plus CTD package with dual temperature, salinity and oxygen sensors. Twenty-four 12 liter ballister bottle samples were taken during all casts to increase accuracy of CTD measurements. The long length of the time-series negates the influence of eddies on the average profiles of salinity and temperature.

Station ALOHA experiences the effects of the eddies north of the islands. Most of the limited research on these eddies is based on the HOT dataset [Lukas and Santiago-Mandujano, 2001; Letelier et al., 2000; Firing and Merrifield, 2004].

3.4.4 Wind and Precipitation

The hourly wind and precipitation data used in this research is from United States Air Force station 911820, Honolulu International Airport (21.3°N and 157.9°W, 2.1 m elevation). Data is available available from October 1, 1949 to present day.

3.4.5 World Ocean Atlas (WOA)

WOA 2009 is a one degree gridded product of in-situ temperature, salinity, dissolved oxygen, apparent oxygen utilization, percent oxygen saturation, phosphate, silicate, and nitrate at standard depth levels. These are analyzed to provide annual, seasonal and monthly compositing periods for the entirety of the World Ocean [Locarnini et al., 2010; Antonov et al., 2010].

3.4.6 Models

All model output was taken from the closest data point in space to each respective Seaglider route.

ECMWF model output used spans from January 15, 2008 - December 15, 2013 with a monthly resolution.

GFDL ecda_$v3.1$ model output used spans from January 15, 2008 - December 15, 2009 with a monthly resolution.

NCEP model output used spans from January 1, 2008 through February 1, 2013 with a monthly resolution.

NRL NCOM model output used spans from January 1, 2008 through March 18, 2013 with a daily resolution.

SODA-POP model output used spans from January 15, 2008 through December 15, 2013 with a monthly resolution.

3.5 TS curve comparison

T-S or θ-S diagrams, generated by plotting instantaneous measurements on a temperature/salinity plane, were first introduced by Helland-Hansen [1916]. Stommel [1962] found T-S diagrams to be similar over large areas of the ocean and to remain constant in time at many locations and consequently T-S relationships were the best way to identify water masses. At any location, the water column likely contains a number of identifiable water masses, each with somewhat arbitrary definitions of temperature and salinity ranges. Usually water masses have a fairly well defined depth range, but depth information is not represented on a traditional T-S plot. Variations from the typical T-S curve can be attributed to the intrusion of water masses originating elsewhere [Helland-Hansen, 1916] or mixing [Sverdrup et al., 1947]. Many migratory features (e.g., eddies and internal waves) displace water vertically and as the displaced water retains the same water properties, these motions do not alter the T-S diagram.

Conservative water properties are primarily set by interaction with the atmosphere and in limited cases by interior mixing. With sufficient hydrographic data, it is possible to trace water masses back to their source region. When water masses mix they do so along a straight line in T-S space [Mamayev, 1975], which means it is possible to determine the percentage contribution of source waters to a particular water sample. As the equation of state is nonlinear [Gill, 1982], isopycnal are curved in $\theta-$S space (Fig. 3.7) and mixing (along a straight line) can result in water that is more dense that either of the contributing water masses, a process known as cabeling. For a full description of a water mass it is necessary to include information about the degree of spatial and temporal variability during its formation [Tomczak and Godfrey, 1994], expressed through its standard deviation. The upper ocean has the largest variability because it is in contact with atmospheric forcing, whereas below the thermocline the standard deviation is usually small.

3.5.1 Volumetric T-S curves

Montgomery [1958] introduced the volumetric T-S diagram to represent the volumes of the water masses of the world's oceans. The two horizontal axes are temperature and salinity while the elevation represents the volumes of water with those particular T-S characteristics [Emery, 2003]. Since Montgomery [1958], volumetric T-S diagrams have been used to look at different regions of the oceans [McCartney, 1977; Emery and Dewar, 1982; Carmack and Foster, 1977; Dickson et al., 2002]. These authors made subjective estimates of the volume of a particular water masses. When profile data is used, the volumetric T-S curve can be interpreted as volume per unit area, or percentage of water column height, within a $\Delta T \Delta S$ grid cell. Percentage of water column T-S plots will be used in this work.

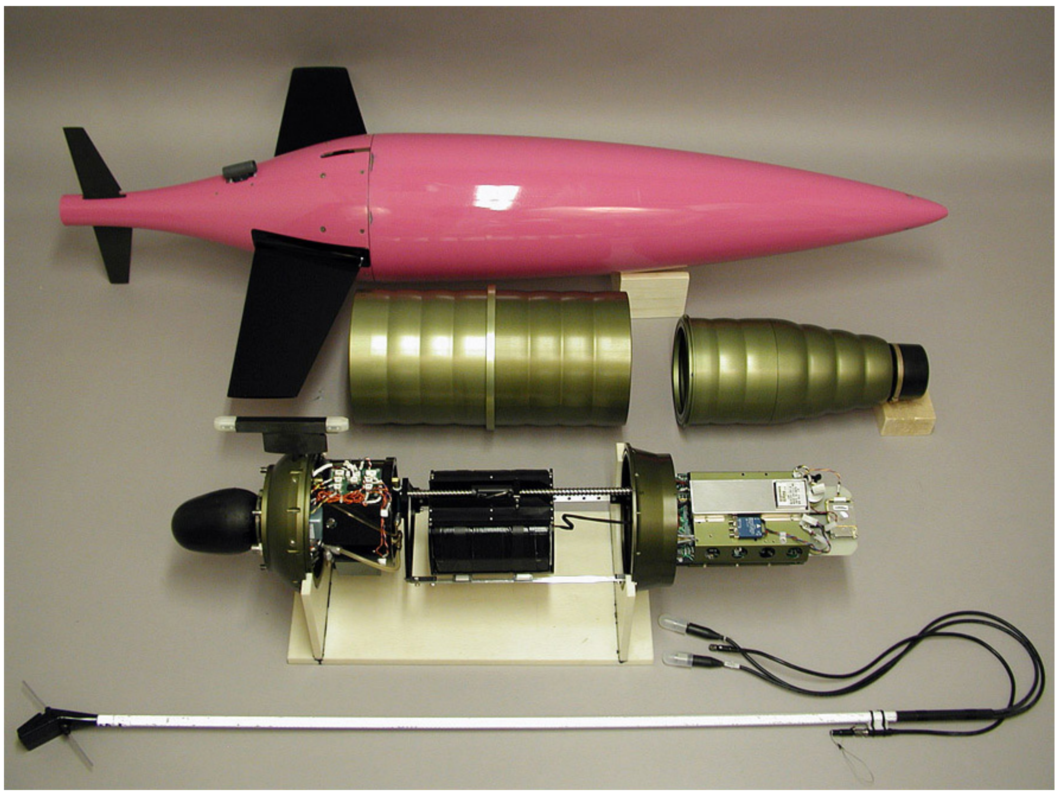

FIGURE 3.1: The components of a seaglider. From top to bottom: the lightweight fiberglass shell, pressure case, electronics and bladder, antenna. The battery (black component in the center) and its shifting mechanism (threaded horizontal bar). (Courtesy of Fritz Stahr, University of Washington Seaglider Fabrication Center)

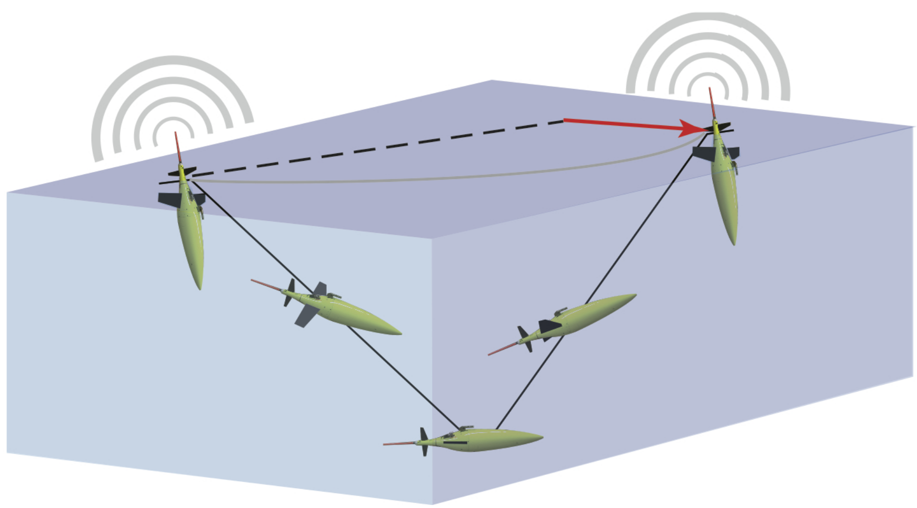

FIGURE 3.2: One dive cycle. The glider finishes transmitting data, takes a GPS position, starts to dive by deflating the oil bladder, once it reaches the target depth it inflates the bladder causing the glider to rise, upon reaching the surface it takes a GPS position and starts to transmit data. (Courtesy of G. Carter)

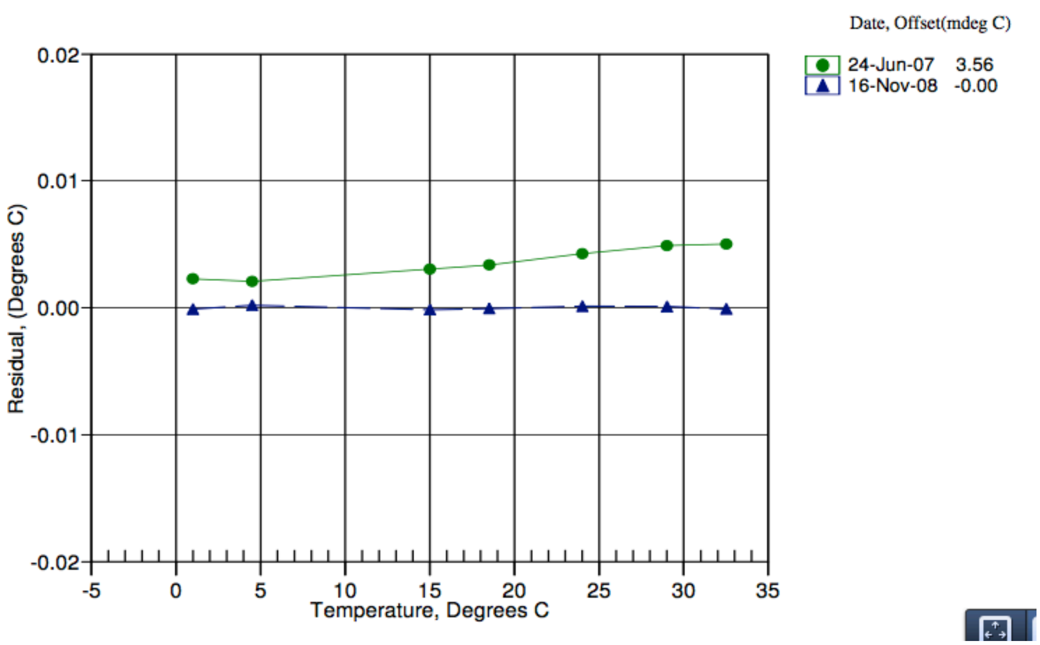

FIGURE 3.3: The effects of differences in temperature coefficients after calibration for PacIOOS 2 (green circle, calibrated June 24, 2007) and PacIOOS 3 (blue triangle, calibrated November 16, 2008) [Service report, Sea-Bird Electronics].

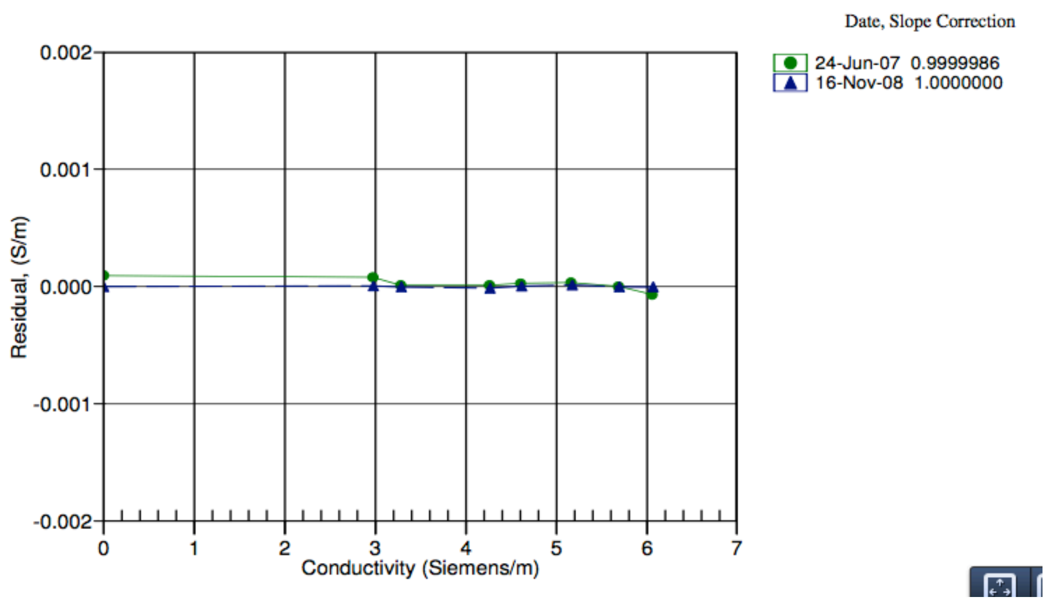

FIGURE 3.4: The effects of differences in conductivity coefficients after calibration for PacIOOS 2 (green circle, calibrated June 24, 2007) and PacIOOS 3 (blue triange, calibrated November 16, 2008) [Service report, Sea-Bird Electronics].

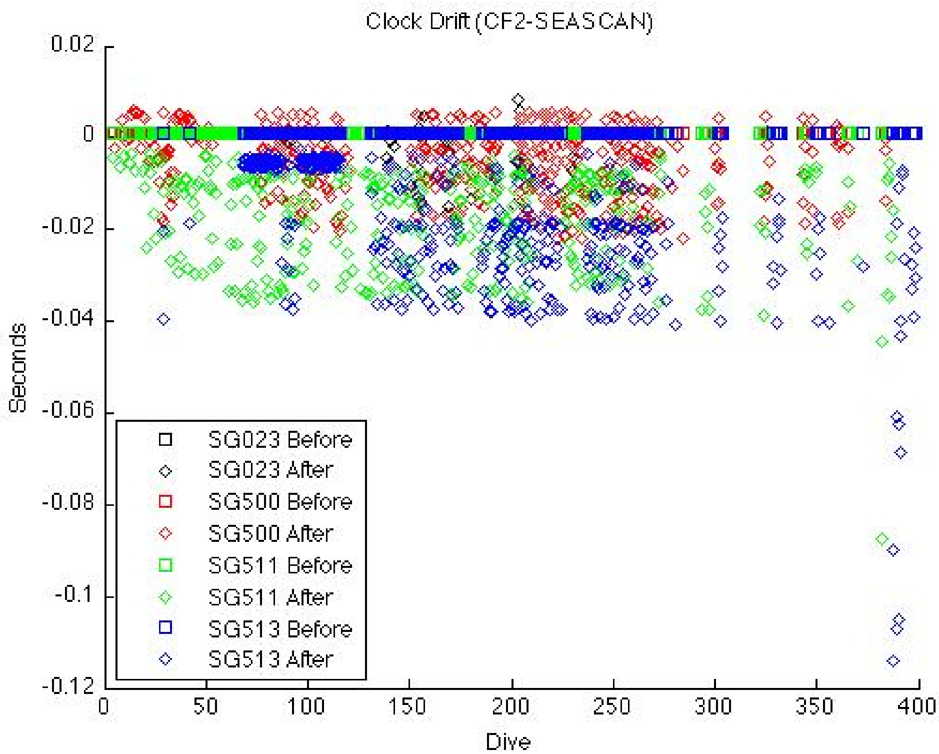

FIGURE 3.5: (Personal Communication, Van Uffelen) a comparison of the clock drift of a SeaScan clock accurate to 1.5 seconds over a year to the clock on the Seaglider. Except for SG513, the Seaglider clocks stays within 0.04 s of the SeaScan.

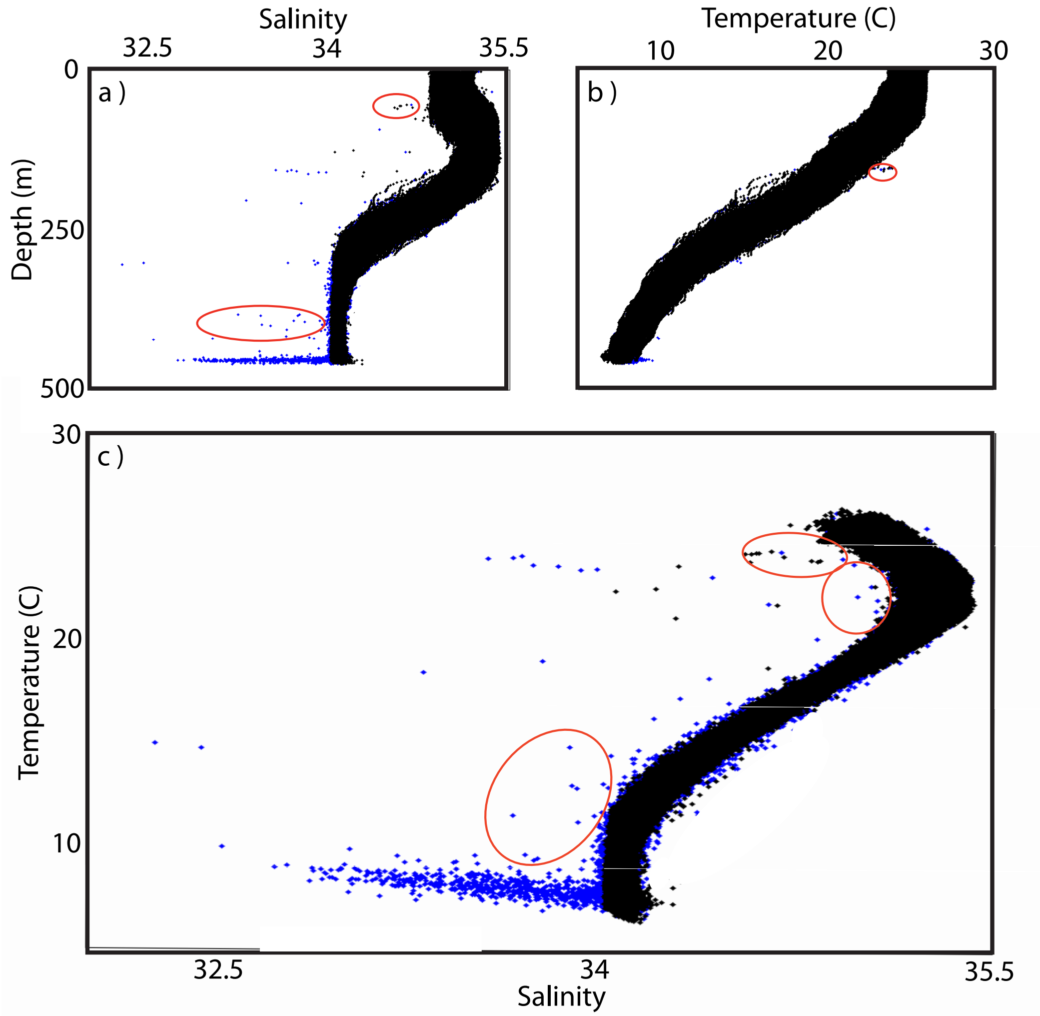

FIGURE 3.6: a) The salinity vs. depth profile of PacIOOS 3. b) The temperature vs. depth profile of mission 3. c) This is the T-S diagram of PacIOOS 3. The adjacent data difference was set to 30. Blue points were found to be erroneous and black points were found to be correct. Data circled in red would have to be hand edited.

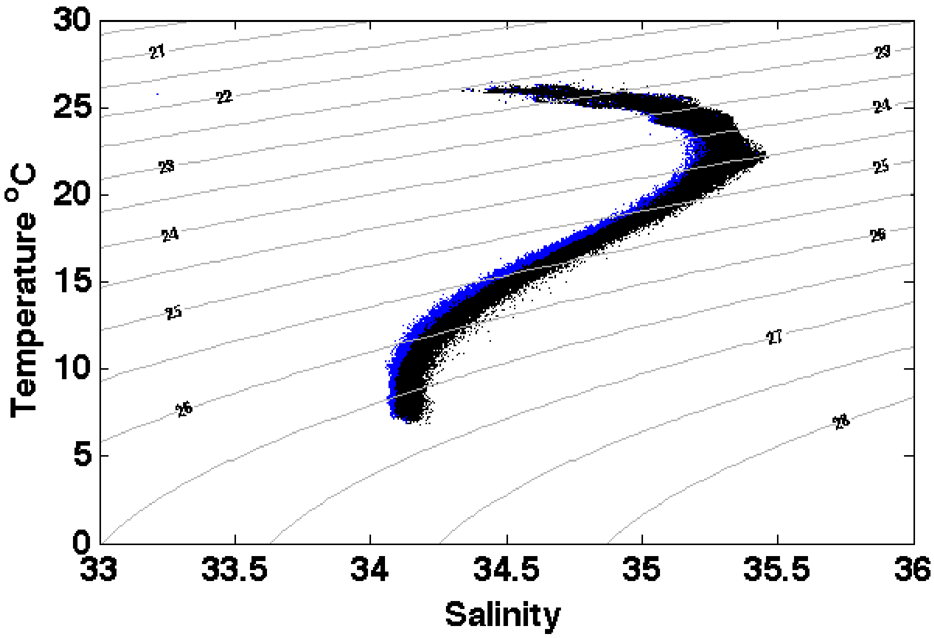

FIGURE 3.7: T-S plot for mission 5. The black dots represent the data collected during the down portion of a dive, the blue dots represent the data collected during the up portion of a dive.

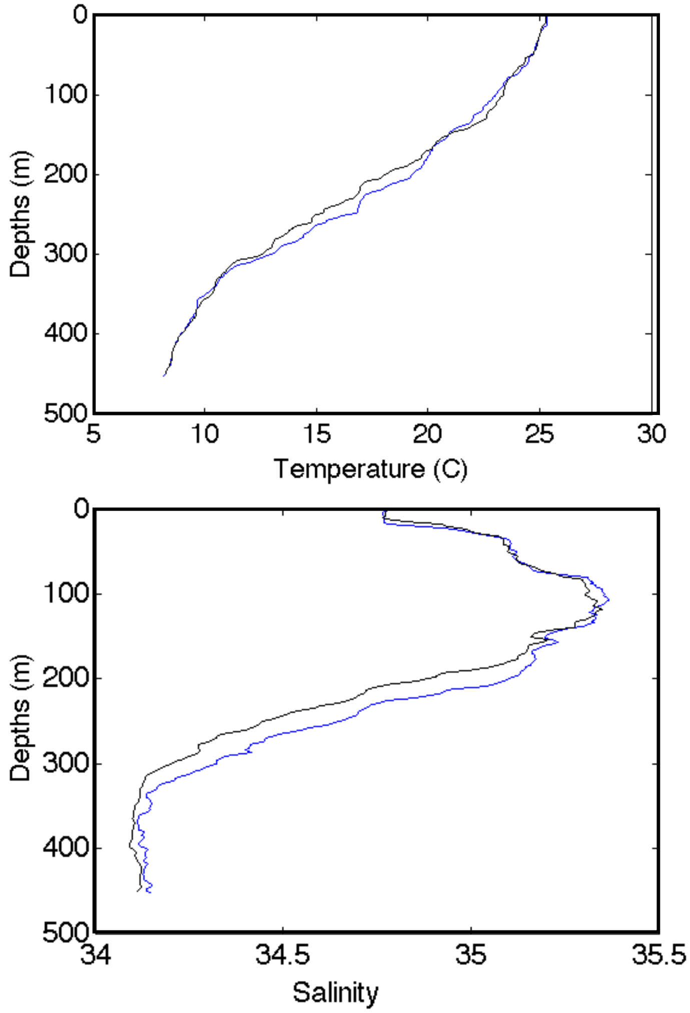

FIGURE 3.8: The black lines show the data collected during the up portion of a dive, while the blue lines represent the data collected during the down portion of a dive. Top temperature and bottom salinity for dive 200 of PacIOOS 5.

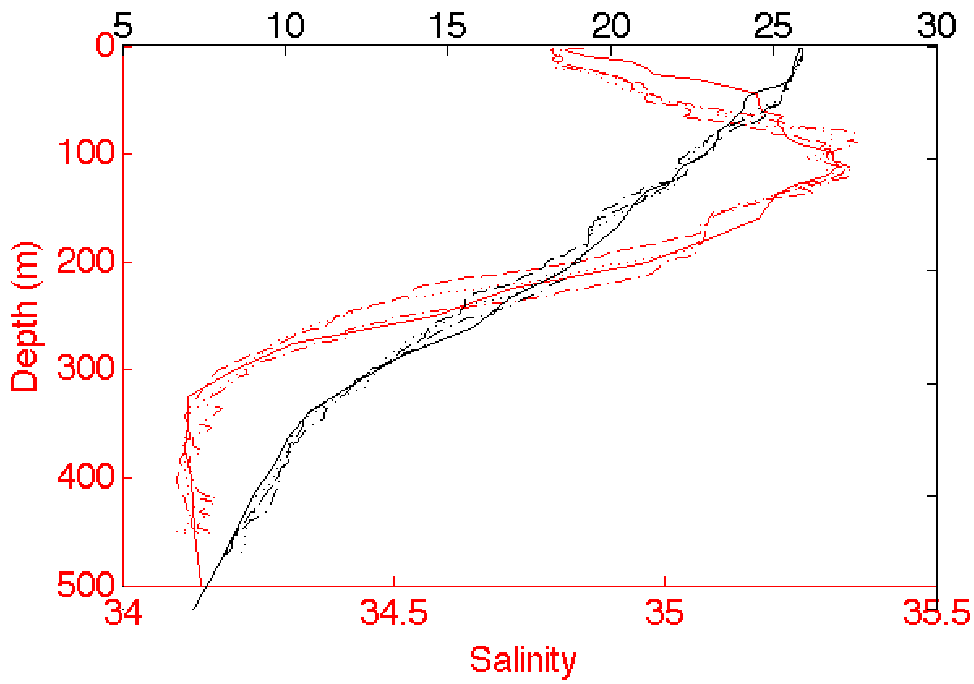

FIGURE 3.9: Temperature (black) and salinity (red) profiles for PacIOOS 5 (Dive 393 - concurrent dive - dotted, dives 392 and 394 - proceeding and following dives - dashed lines) compared to an Argo (float #5902157) profile (solid lines) 16.7 km apart on April 30, 2010 at 05:12 UTC.

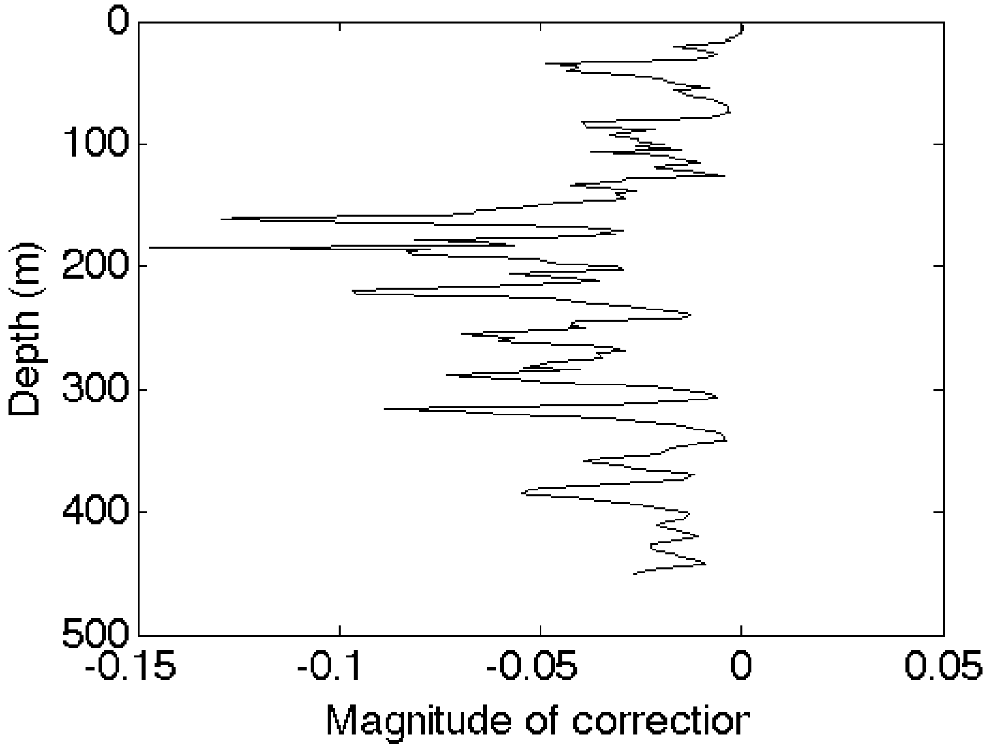

FIGURE 3.10: The magnitude of the temperature correction for (down) profile 393 of PacIOOS 5.

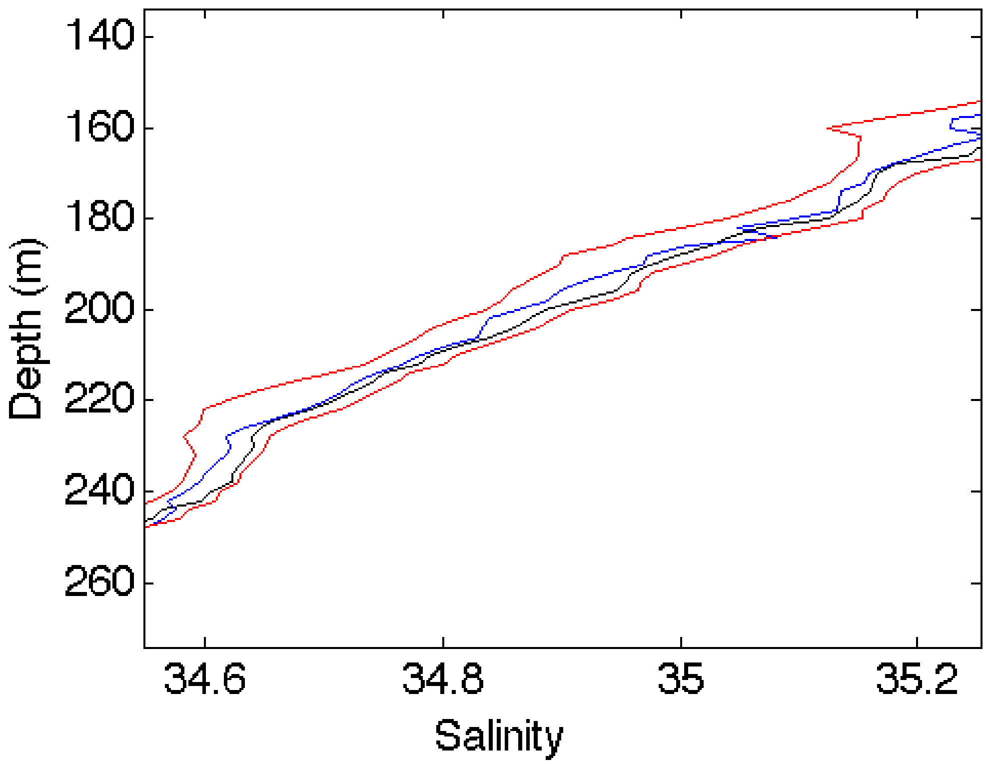

FIGURE 3.11: The corrected salinity for dive 181 (profiles 392 and 393), corresponds to previous Fig. 3.10 of PacIOOS 5. Black, down, and blue, up, are the corrected profiles while red is the uncorrected profile.

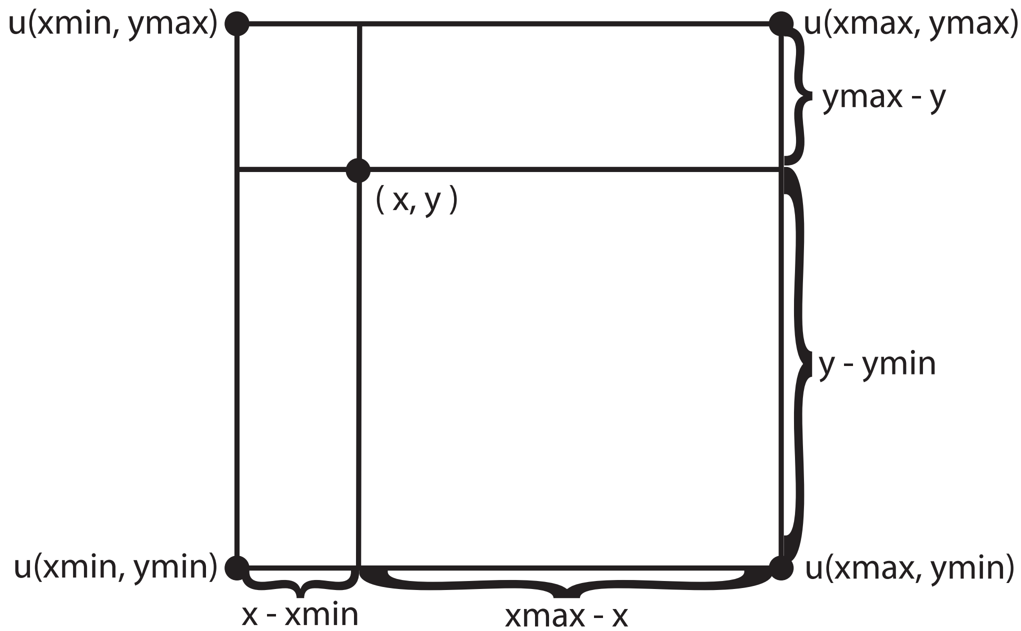

FIGURE 3.12: The weighting scheme used to calculate the value of the velocity vectors applied at each time step.

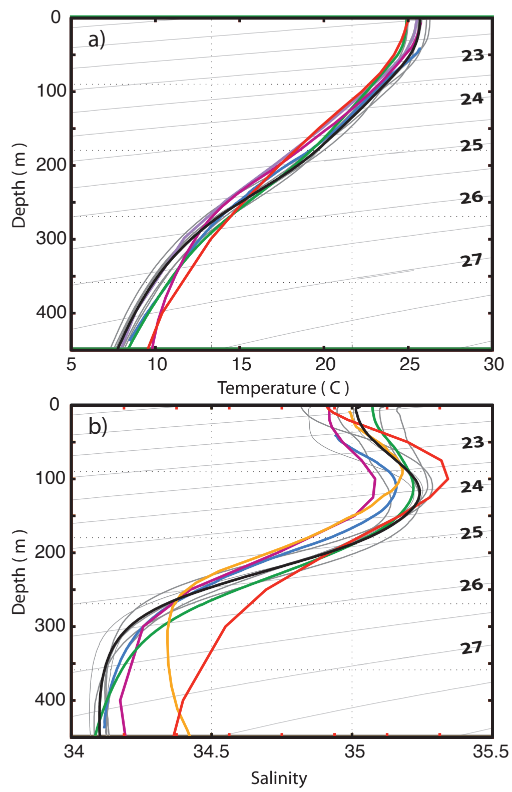

FIGURE 3.13: Top - The average salinity vs. depth profiles, bottom - the average salinity vs. depth profiles. Gray - Individual PacIOOS Seaglider mission averages, black - all PacIOOS Seaglider missions average, blue - mooring, magenta - HYCOM, green - HOT, red - ROMS, and orange - Argo.

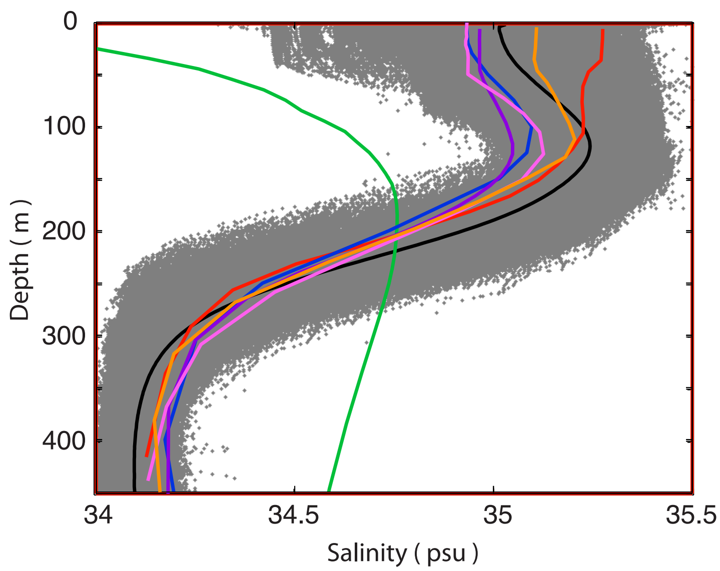

FIGURE 3.14: A comparison of the nearest point in space, averaged over the time of the 6 PacIOOS missions, model output (red - ECMWF, green - GFDL, blue - HYCOM, purple - NCEP, pink - NRL NCOM, and orange - SODA-POP) to Seaglider profiles (grey - data from all 6 missions, and black - average profile over all 6 PacIOOS missions).

Chapter 4

Results

4.1 Organization

This Section is organized such that Seaglider observations are investigated first looking at similarities then disparities with particular interest in anomalies and trends. Observations are compared to assess spatial distribution and physical processes. All missions are used to show a regional description and to assess the full Hawaiian Islands region over the entirety of the year.

4.2 Seaglider Observations

From the 12 Seaglider missions (Table 3.1) there are 5 periods of overlapping data between the PacIOOS Seagliders and the ALOHA Seagliders providing a perspective north and south of the islands (Fig. 4.1). The Seaglider at the ALOHA site nominally follows a bow tie path with 4 sections labelled A1 - A4. A1 and A3 are orientated north south and with the Seaglider traveling north and are 16.7 km and 15.7 km respectively. A4 is orientated and transversed by the Seaglider NE-SW and is 27.2 km long. A2 is orientated and transversed NW SE and is 27.8 km. The PacIOOS Seaglider nominally transverses a triangular route with legs referred to as legs, labelled P1 - P3. The leg lengths are 18.0 km, 28.6 km, and 33.6 km respectively, with the Seaglider predominantly transversing the route clockwise.

The overlapping period from Aug. 15 - Nov. 10, 2010 (PacIOOS 4 and ALOHA 3) lasts over three months and illustrates the differences north and south of the islands (Fig. 4.2). The white lines across the bottom of each Figure show a two day time step.

We observe higher salinity, in waters lighter than $25\sigma_\theta$, at the ALOHA site with the largest difference observed at the subsurface salinity maxima. During the later half of ALOHA 3 (after Oct. 10), the subsurface salinity maxima extends into a surface salinity maxima. This is due to an eddy at Station ALOHA and will be discussed further in Section 4.6. The average σ_θ-salinity plot (Fig. 4.2 c & d) for each mission is plotted in red while the average curve for the region is plotted in black (Sec. 3.4.1 & Sec. 3.4.3). It is found that the mission averages are comparable to the long term averages with the greatest differences lighter than 25.5 σ_θ in the ALOHA dataset. The ALOHA long term average uses data from throughout the year where the mission average uses data from August - November. The expected E-P for a year average is less than E-P for a summer/fall average meaning it is to be expected for the mission average to exceed the long term average. Figure 4.2 c & d (blue) shows the variability of each dataset compared to the mission averages. We see much larger variability near the surface at ALOHA than at PacIOOS (Fig. 4.2 c & d (blue)).

Freshening events (near surface, green) occur $\approx$ twice a month (Aug. 21, Sept. 3, Oct. 3, Oct. 19, Nov. 5), and correspond to rain events at the islands. These large events extending down 20 m are only observed in the PacIOOS dataset (Fig. 4.2 b), due to its relative closeness to shore and fresh water inputs. Rain events are usually coherent within the top 0.5 σ_θ of the water column. High surface salinities are defined as above the regional averages: 35.20 at ALOHA, and 35.06 at PacIOOS. In ALOHA 3 high salinity started October 8 and lasted through the end of the mission, corresponding to an eddy residing at the ALOHA study site (Sec. 4.6), and high salinity occurred approximately once a month in PacIOOS 4. Over all missions, the PacIOOS high sea surface salinity events can last between 3 and 7 days, with PacIOOS 4 anomalies lasting 4 and 7 days respectively.

4.3 Spatial versus temporal

The black lines and numbering along the top of Fig. 4.2 a & b show a turning point on each respective nominal path. Usually the Seaglider follows the route A4

- A3 - A2 - A1 or P1 - P2 - P3, from about noon on August 21 through the early hours of September 30, the Seaglider traveled back and forth on P3 resulting in 5 transverses of P3. This occurred due to strong north south currents pushing the Seaglider off course. Each leg is labeled with the corresponding labels A1 - A4, P1 - P3 as shown in Fig. 4.1. No spatial pattern, resulting from the different legs of the glider path, is discernible at the ALOHA site.

In order to further investigate spatial versus temporal in the datasets, the salinity values of ALOHA 3 and PacIOOS 4 were plotted in a time - latitude - density plot (Fig. 4.3) to show the spatial distribution over the time of the two missions. The black line along the top is the minimum σ_θ in time. During PacIOOS missions, low salinity is observed at a few (October 26 and November 2) but not all of the latitude minimums (September 30), (corresponding to the Seaglider transversing the southern corner of the nominal route). The observed low salinity corresponds to the low salinity bands observed in the PacIOOS 4 mission. These bands of ≈ 35.1 are observed spanning from 25 σ_θ up to the surface. Similar phenomena do not occur during any of the missions at ALOHA. Slopes range from 0.4707 $\frac{kg}{m^3\ km}$ to 2.2306 $\frac{kg}{m^3\ km}$. Banding only occurred while the Seaglider is in the region of the southeast corner, although not during all transverses. This indicates temporal as well as spatial variation causing the banding phenomena.

4.4 Variation in water properties

By looking at the salinity values for various features: salinity maximum ($24.2-25\ \sigma_\theta$), thermocline ($25-26\ \sigma_\theta$), and salinity minimum($25.1-26.2\ \sigma_\theta$), found at both Seaglider locations, distinct differences between the two locations are observed. The salinity maximum has higher salinity values at ALOHA than at PacIOOS. We do see increased noise occurring in the ALOHA salinity maximum starting October 8 (Fig. 4.4), the same time an eddy is observed at station ALOHA (Sec. 4.6). During the latter half of the eddy, starting October 26, the PacIOOS salinity maximum salinities fall below 35.2 (Fig. 4.4, second from top). No correlation between the salinity maximums is observed. In the thermoclines (Fig. 4.4, third from top & third from bottom) at both sites' salinities are relatively consistent: ALOHA around 35.2 and PacIOOS (larger variation) at 35.1. The salinity minimum at ALOHA has a large signal for the σ_θ range (Fig. 4.4, second from bottom). The high salinity events seem to have no relationship with any of the other observed salinity curves. No apparent relationship between the two sites can be determined from these two corresponding missions.

The lower salinity bands reaching vertically from $\approx 25\sigma_\theta$ to the surface in PacIOOS 4 (Fig. 4.2, second from top), correspond to the minimums observed in the PacIOOS salinity maximums (Fig. 4.4,second from top) and the maximums in in PacIOOS salinity minimum (Fig. 4.4, second from bottom).

4.5 Spatial distribution of T-S curves

Figure 4.5 shows the T-S curves of the entirety of ALOHA 3 (top) and PacIOOS 4 (bottom) with the depths plotted from green to blue to illustrate the depths of the specific water properties. The mission average ALOHA T-S curve (red line) (Fig. 4.5, top) is characteristic of the $22.5° - 27.5°$N and $155° - 165°$W region while the average PacIOOS T-S curve (Fig. 4.5, bottom) is characteristic of the $17.5° - 22.5°$N and $155° - 165°$W region as defined by Lumpkin [1998] (Fig. 2.1). Neither follows the Lumpkin [1998] T-S curve exactly, in particular the ALOHA curve has a higher salinity value above 20°C than is expected for the region. Various T-S curves are observed over the 12 missions, with the PacIOOS site observing the largest number of Lumpkin [1998] regional water masses. Each mission is compared to the various regional T-S and the region of origin is estimated.

Lumpkin [1998] calculated the average T-S curve for each 5° by 10° region from CTD casts shown in Fig. 2.1 as dark grey dots with the pink curve as the average curve. The Hawaiian Islands and the nominal Seaglider paths (red) are plotted in the relevant T-S regions. Each regional average T-S curve was compared to all Seaglider profiles through a RMS calculation and an "origin" region assigned to most profiles, 12% of profiles were in transition between regions.

The ALOHA 3 mission had four 'origin' regions, (Fig. 4.6, top). For a brief period, near the beginning of the mission (October 28), the T-S curve transitions from the region 8 to the region 9 T-S curve with the most distinct change occurring in the upper water column. Figure 4.7 shows HYCOM 1/12 degree velocities averaged over the upper 50 m of the water column. Water moves from region 9 (to the right of 205°) into the ALOHA Seaglider study site (blue bow tie) on August 28 following a potential route indicated by the red arrows. For most of the mission the ALOHA study site is isolated from the east and west due to strong northward and southward flows resulting from eddies. An example of this occurs on September 30 (Fig. 4.8), by this time the T-S curve has reverted back to the Region 8 T-S curve and the average velocity curves of the upper 50 m shows the isolation of the waters at the study site from the surrounding regions, note the red arrows highlighting the flow patterns. For the T-S curves from regions 8 and 9, the distribution of the water column is separated into the temperature maximum, the subsurface salinity maximum and the salinity minimum. The final T-S curve observed at the ALOHA site is distinct from all of the T-S curves of the surrounding regions, although the T-S curve is clearly defined and distinct, there is no matching Lumpkin [1998] regional T-S curve. The most similar curve originating from region 10. The unique T-S curve is observed when the eddy is present at the study site (Sec. 4.6). The percentage of the water column plot (Fig. 4.6, region 10) shows two groupings of large amounts of water at the temperature extremities. These two large water volumes and the relative straightness of the T-S curve between them indicate mixing between waters found on either side of 15° and 25°C.

During the period overlapping with ALOHA 3 (Fig. 4.2), PacIOOS 4 had three transitions to the water properties of another region. All four of the observed T-S curves are plotted in Fig. 4.9. Figure 4.9 (black) shows the percentage of water column T-S curve occurs immediately prior to the concurrent time series. The general curve matches the expected curve for the Seaglider's region, region 13, except for a high salinity nodule that is protruding from $\approx 24°$. The protrusion occurs to a minimal extent randomly throughout the remainder of the mission and is included in the region 13 T-S curve compilation (Fig. 4.9, red).

From the start of the PacIOOS 4 through August 23, the Seaglider observed six different curves, with the majority matching that of region 13. The T-S curve in Fig. 4.9 (blue) is distinct and only lasted for a short period of time ($\approx$ 1 day). The upper portion is most similar to the T-S curve from region 9 but the region immediately surrounding the salinity minimum is that of region 13. Figure 4.10 (August 23) shows a possible route of advection (red arrows) into the PacIOOS study site from the north east, or the approximate area of region 8. The velocity vectors below 300 m show minimal advection into the region (not shown). The final T-S curve (Fig. 4.9, red) shows how the water column reverts back to the expected values of region 13. Figure 4.11 shows there is minimal advection into the region on September 30 due to the strength of the eddy just south of the PacIOOS site.

4.6 The eddy at ALOHA

From October 9 through the end of the mission an eddy was at the ALOHA site. The doming of the isotherms shown in Fig. 4.12 identifies the eddy as anticyclonic. This is also observed in a negative SSH perturbation. Due to the uniqueness of T-S curve and the extreme aberrations from the average salinity values, it is proposed that the water has advected with the eddy from a region outside of the Lumpkin T-S curves (west of 135°W). In early 2000, the HOT encountered extreme water mass anomalies in CTD measurements at Station ALOHA [Lukas and Santiago-Mandujano, 2001]. They found high salinities at depths centered around 400 m, in this study we see high salinity anomalies are observed in the upper 50 m of the water column. Between 100 m and 350 m waters have anomalously low salinities.

4.7 Salinity anomalies

Over the course of the six PacIOOS missions, near surface, high salinity, anomalies (≥ 35.2), lasting 3-10 days were observed about once a month. The ALOHA site did not observe similar anomalies. High salinity patches are defined as those that exceed the mean salinity profile value by 0.2 from the surface to 50 m, with the maximum anomaly of +0.3. No near surface, high salinity anomalies were observed over the course of PacIOOS 6 (June 13 - July 30, 2011), whereas PacIOOS 7 (April 25 - July 25, 2013) had two high salinity events a month on average. The temporal salinity gradient of salinity events is quite steep, transitioning to the high salinity state over the course of hours.

Figure 4.12 shows the salinities during ALOHA 3 and PacIOOS 4 (Aug.13 - November 10, 2010). Between September 5 and 17, a high salinity anomaly of approximately +0.2 was present at the PacIOOS site. The intensity of the anomaly decreases slightly over the course of the 12 days. Both the appearance and disappearance of the anomaly is abrupt. The high salinity anomaly water is uniformly occurring from the surface down below 50 m. A second anomaly occurs later in the mission starting on October 20 which increases in strength until it reaches a maximum of +0.3. The anomaly abruptly disappeared for a day and then returned for two more days ending abruptly on October 30. This variation was found to be spatial. The abrupt change in salinity corresponded to the Seaglider traveling a latitude minimum. The anomaly consistently reached depths of 80 m. The anomalies seen during PacIOOS 4 have similar magnitude but, last longer than those seen during other missions.

A Lagrangian tracer model (Section 3.2), using velocities from 1/12 degree HYCOM+NCODA model output results showed, high salinity waters do not advect to the study region along the surface. If the water was to flow along a straight line between the high salinity pool and the study site, it would require either extremely high velocities or extensive periods of cyclonic-cyclonic eddy interaction, neither of which are observed.

Numerical studies by Merrifield et al. [2002] found island trapped waves can be created by storm events, however, the high salinity events do not correspond to wind data indicating wind or storm events. Evaporation (Section 2.1.7) does not exceed expected values during or proceeding the observed anomalies.

An initial assessment of the eddy system in the region is able to indicate if a high salinity event is occurring. Two cold core eddies on either side of the island with submesoscale interactions in the Kaiwi channel leads to anomalies. The vertical black bars on Fig. 4.12 show three unique setups:

a) High PacIOOS salinity, low ALOHA salinity (September 10, 2010)

b) High PacIOOS salinity, high ALOHA salinity (October 21, 2010)

c) Low PacIOOS salinity, high ALOHA salinity (November 2, 2010)

All three situations have cold core eddies on either side of Oahu. During periods of high salinity at the PacIOOS site, there is eddy-eddy interactions through the Kaiwi Channel shown both in SSH and the average velocities of the upper 50 m. Figures 4.13 and 4.14 (dates we see high salinity) show an upwelling eddy in the region to the south of the Seaglider and strong northward flow through the Kaiwi Channel. The flow field lacks any strong southward flow from regions of high salinity, leaving the source of high salinity water to the region immediately surrounding the PacIOOS site. The only water with high enough salinity values is that of the subsurface salinity maximum. This salty water is forced to the surface due to the outcropping of the 100-120 m isotherms (the depth of the subsurface salinity maximum) and advected into the PacIOOS study site through eddy-eddy interaction through the Kaiwi Channel. Periods of non anomalous salinity are not associated with low SSH and northward velocities through the channel. During a period of low salinity (Fig. 4.15) there was still an upwelling eddy to the south of the PacIIOS site, but unlike previous cases there was southward flow through the Kaiwi Channel. Outcropping of high salinity water was still occurring, the eddy was stronger at this point in time than the previous two snapshots (Fig. 4.13 and 4.14), the major difference was the eddy-eddy interaction through the Kaiwi Channel. The salinity at ALOHA simply corresponds to the presence of a cold core eddy at the study site. October 21 and November 1 had an eddy residing at ALOHA and high salinity was observed. On September 10 a warm core eddy was at the ALOHA site and high salinity values were not observed.

Sea surface salinity measurements from Aquarius provide a snapshot of the region once every 7 days. The measurements are thrown off by the islands and it is only available concurrently with PacIOOS 6 and ALOHA 5, April-July 2013. Although gridding is coarse, salinities above 35 in the study region during time periods corresponding to high salinity anomalies in the Seaglider data were observed.

Occasionally, but not always, a temperature anomaly corresponding to the salinity anomaly was observed. The greater the distance, between the center of the dominant eddy, defined as the eddy that dictated the SSH around Oahu, and the PacIOOS Seaglider site (21°04’ N, 157°52’ W), the less of a temperature signature was observed. During some of the missions where the eddy location was near (< 10 km) to the Seaglider position a corresponding temperature signature was visible. Temperature in the upper ocean is not conserved due to atmospheric and solar heating and although salinity is also modified at the surface they are not modified at the same rate. The longer the cold upwelled water resides at the surface or the longer the distance to the study region, the less likely a temperature anomaly will correspond to a salinity anomaly.

4.8 Extension to all missions

Throughout all of the 11 different missions, we see higher salinities above 25 σ_θ at the ALOHA site. The mission averages do maintain the same shape and general values as the long term averages. The ALOHA depth-average salinity tends to be lower in the upper portion of the water column, particularly during the summer months: PacIOOS 3, PacIOOS 6, PacIOOS 7, ALOHA 1, ALOHA 4 and ALOHA 5.

High sea surface salinity events at the PacIOOS site occur during 6 of the 7 PacIOOS missions and eddies are directly observed in the dataset twice over the five ALOHA missions. Positive sea surface salinity occur with the same frequency, as observed in PacIOOS 4, about once a month while the length of anomalies stay between 3 and 7 days for all missions except PacIOOS 7. During PacIOOS 7, high near surface salinity was observed over the majority of the mission.

All profiles during the 11 missions were split into the 25 regions identified by Lumpkin. Over the 5 ALOHA missions, the region 8 T-S curve was observed 86% of the time. Transitional T-S curves during eddies were not included in these numbers. Regions 3, and 9 are observed 5 and 9 % respectively. This is not the case for the PacIOOS missions, regions 7, 8, 9, 13 and 14 are observed during PacIOOS 2 and PacIOOS 7. Each of those regions had 5.3, 31.8, 25.5, 7.4 and 30% of the profiles, respectively from the PacIOOS missions.

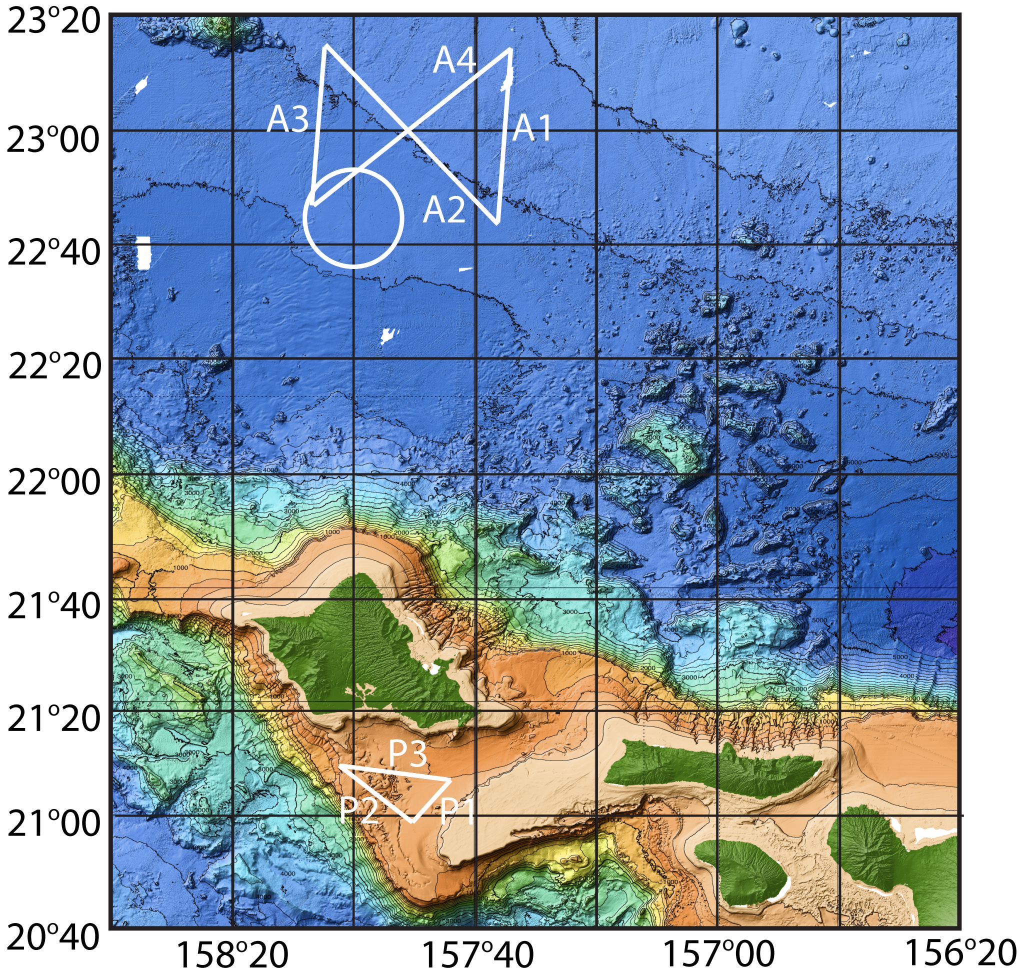

FIGURE 4.1: A bathymetric map looking at the area surrounding Oahu, showing the two Seaglider routes. To the north the ALOHA route follows a bow tie with each of the four legs labeled A1 - A4. The circle is Station ALOHA. To the south of Oahu the PacIOOS route follows a triangle with each of the three legs labeled P1 - P3.

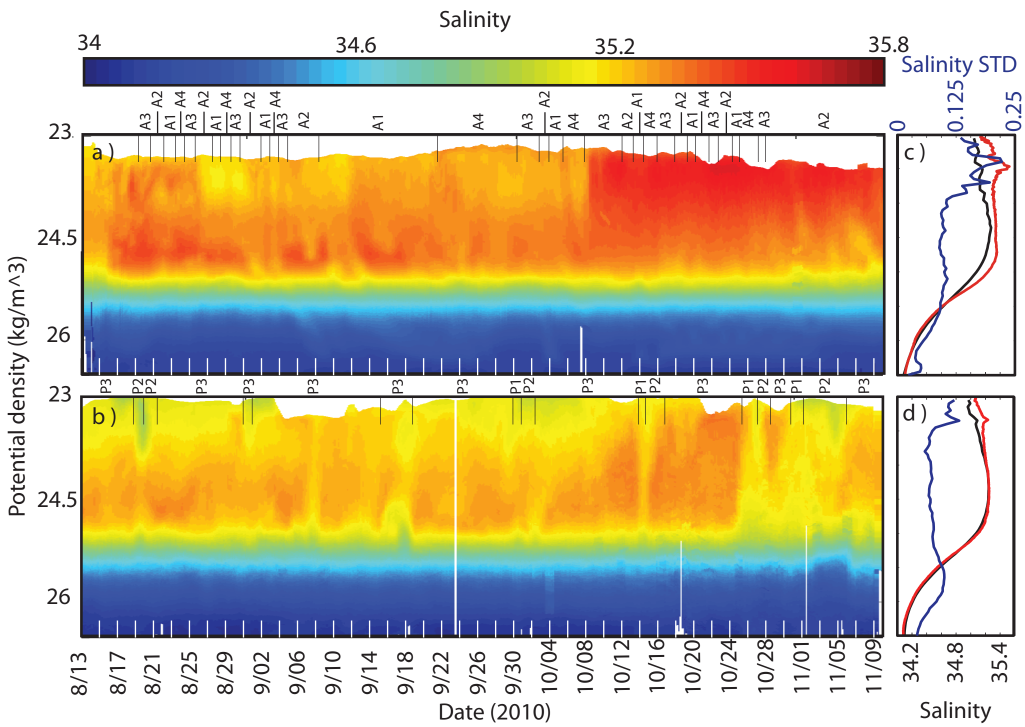

FIGURE 4.2: The potential density - time plot of the salinity at a) the ALOHA site and b) the PacIOOS site. Vertical lines across the top of each figure show the turning points of each respective route with the leg transversed denoted by A1-A4 or P1 - P3. c) and d) show the long term average of salinity in black with the red showing the mission average. The blue curve shows the STD of the salinity.

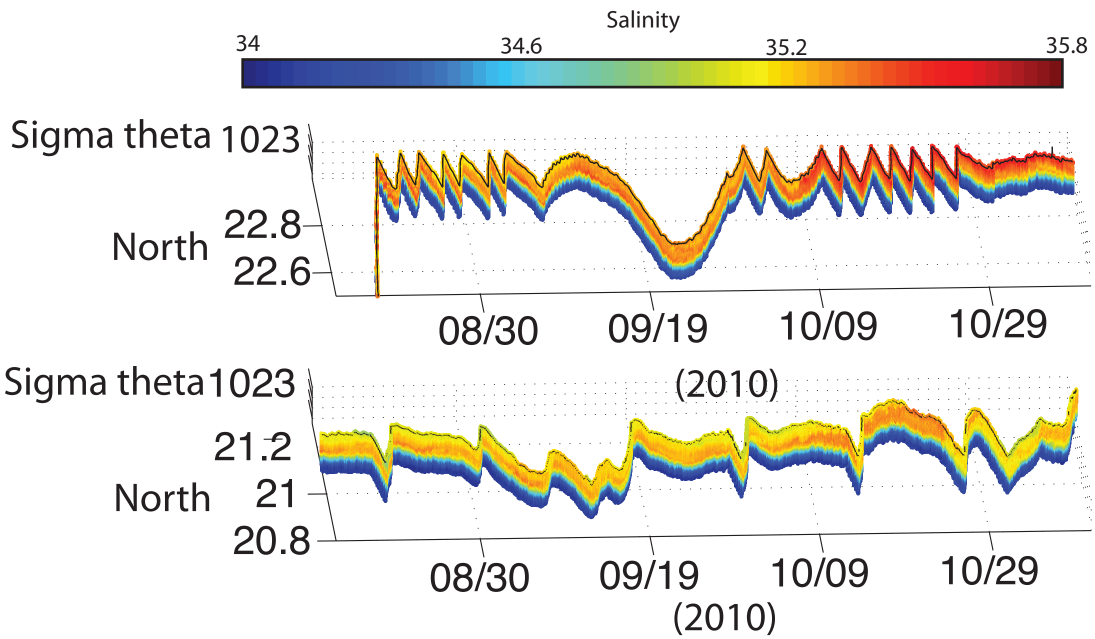

FIGURE 4.3: The salinities are plotted on a latitude - time - potential density. The black like across the top is to help delineate the changes in latitude vs. time.

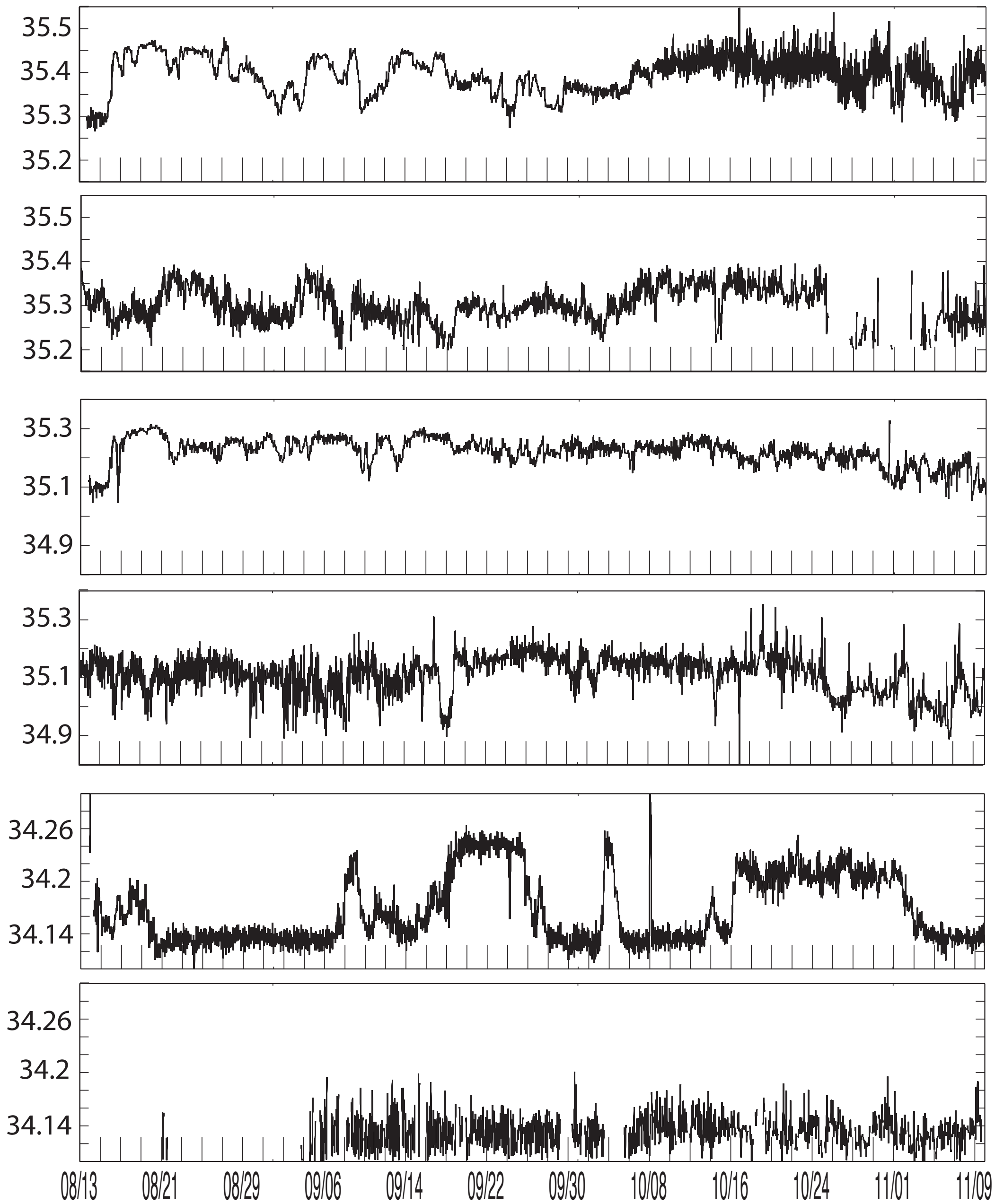

FIGURE 4.4: The salinity values are calculated from within specific σ_θ bands to look in at the different water masses and to provide a direct comparison of the two Seaglider sites. The plots in a descending manner are: ALOHA salinity maximum ($24.2 - 25\sigma_\theta$), PacIOOS salinity maximum ($24.2 - 25\sigma_\theta$), ALOHA thermocline ($25 - 26\sigma_\theta$), PacIOOS thermocline ($25 - 26\sigma_\theta$), ALOHA salinity minimum ($25.1 - 26.2\sigma_\theta$), and PacIOOS salinity minimum ($25.1 - 26.2\sigma_\theta$).

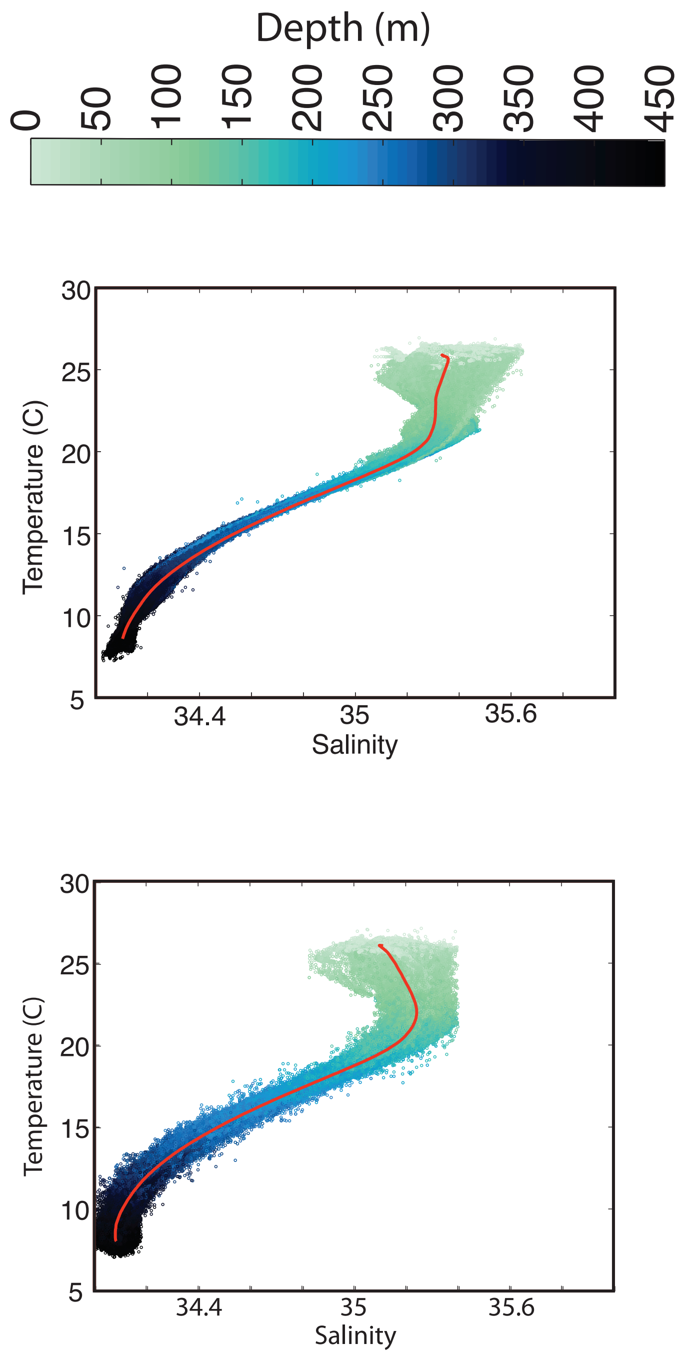

FIGURE 4.5: The TS curve for ALOHA 3 (top) and PacIOOS 4 (bottom) show the cloud of all measurements taken at each site over the course of the missions with the depth of the points shown from green (shallow) to dark blue (depths of 450 m). The red line shows the average TS plot for each of the missions.

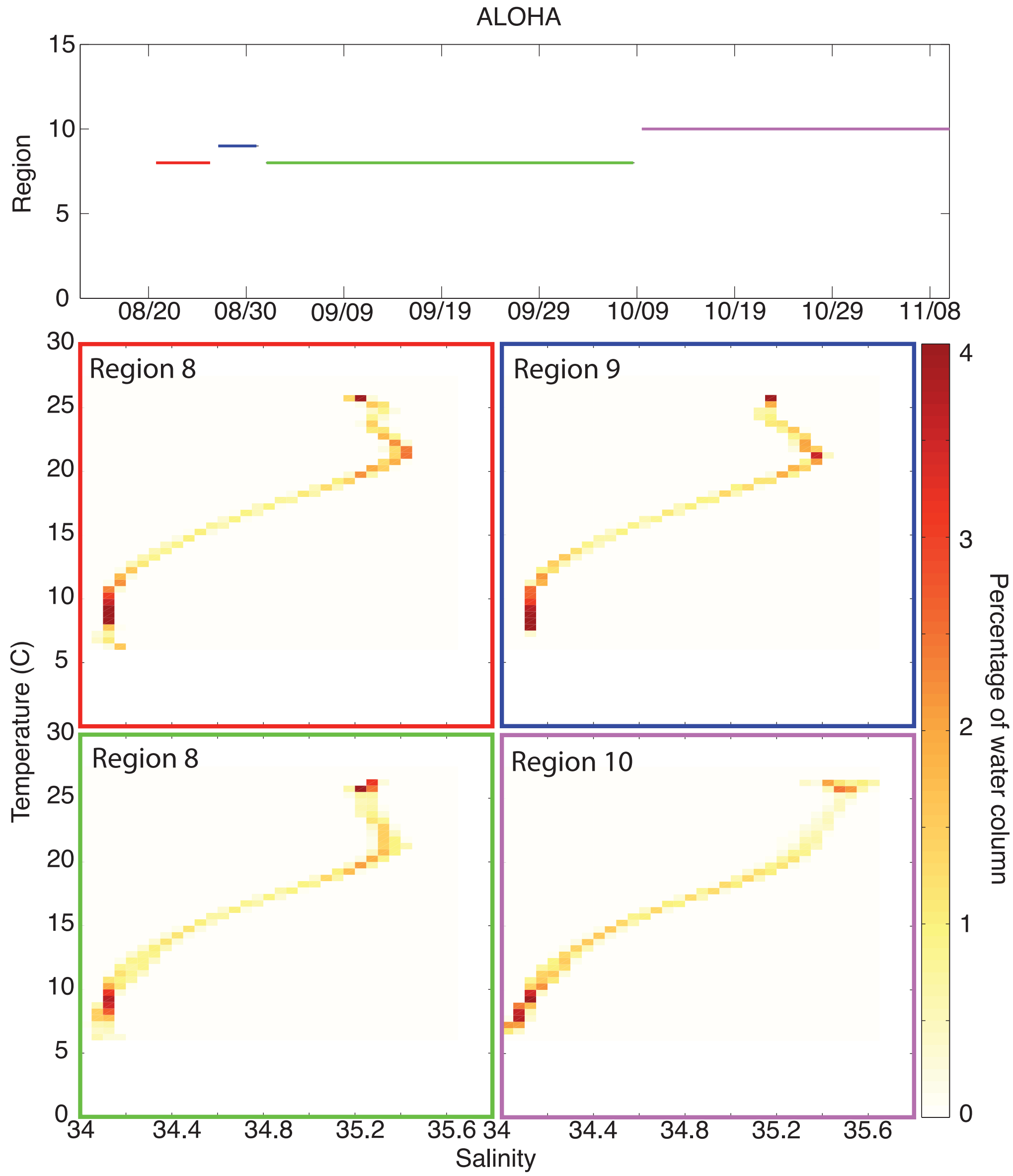

FIGURE 4.6: Top: The Lumpkin [1998] region (Fig. 2.1) of the observed TS curve during ALOHA 3. The color of the line matches the box surrounding the corresponding percentage of the water column T-S plots shown. Region 8 - (22.5 – 27.5°N, 155 – 165°W), Region 9 - (22.5 – 27.5°N, 145 – 145°W), Region 10 - (22.5 – 27.5°N, 135 – 145°W).

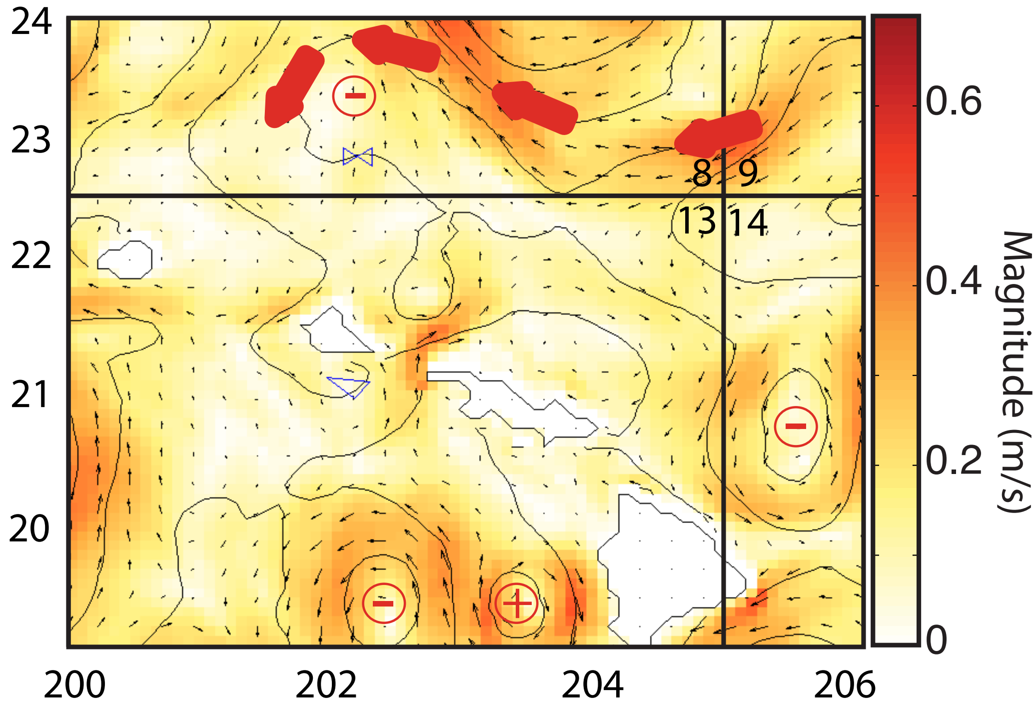

FIGURE 4.7: A plot of the average of the top 50 m velocity vectors from HYCOM 1/12 on August 28. The average flow speed for the upper 50 m is plotted in color. Contours show 2 cm intervals of SSH. The Lumpkin [1998] regions are denoted by the region number (Fig. 2.1). The PacIOOS (triangle) and ALOHA (bow tie) nominal routes are plotted in blue. The + and − indicate positive and negative SSH anomalies.

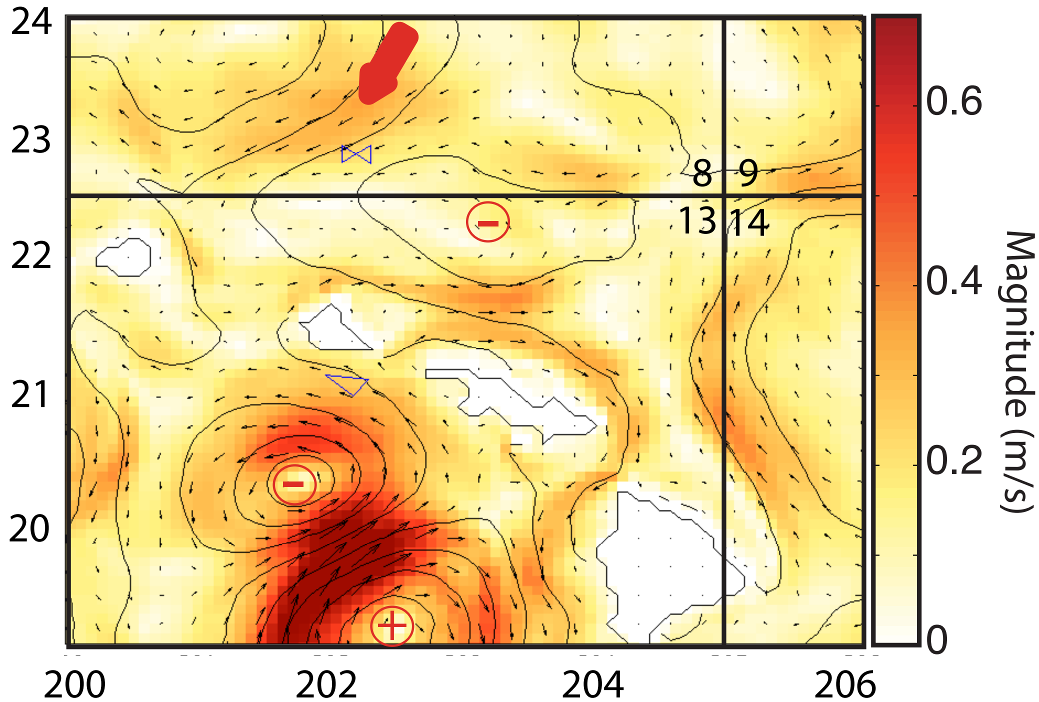

FIGURE 4.8: A plot of the average of the top 50 m velocity vectors from HYCOM 1/12 on September 30. The average flow speed for the upper 50 m is plotted in color. Contours show 2 cm intervals of SSH. The Lumpkin [1998] regions are denoted by the region number (Fig. 2.1). The PacIOOS (triangle) and ALOHA (bow tie) nominal routes are plotted in blue. The + and − indicate positive and negative SSH anomalies.

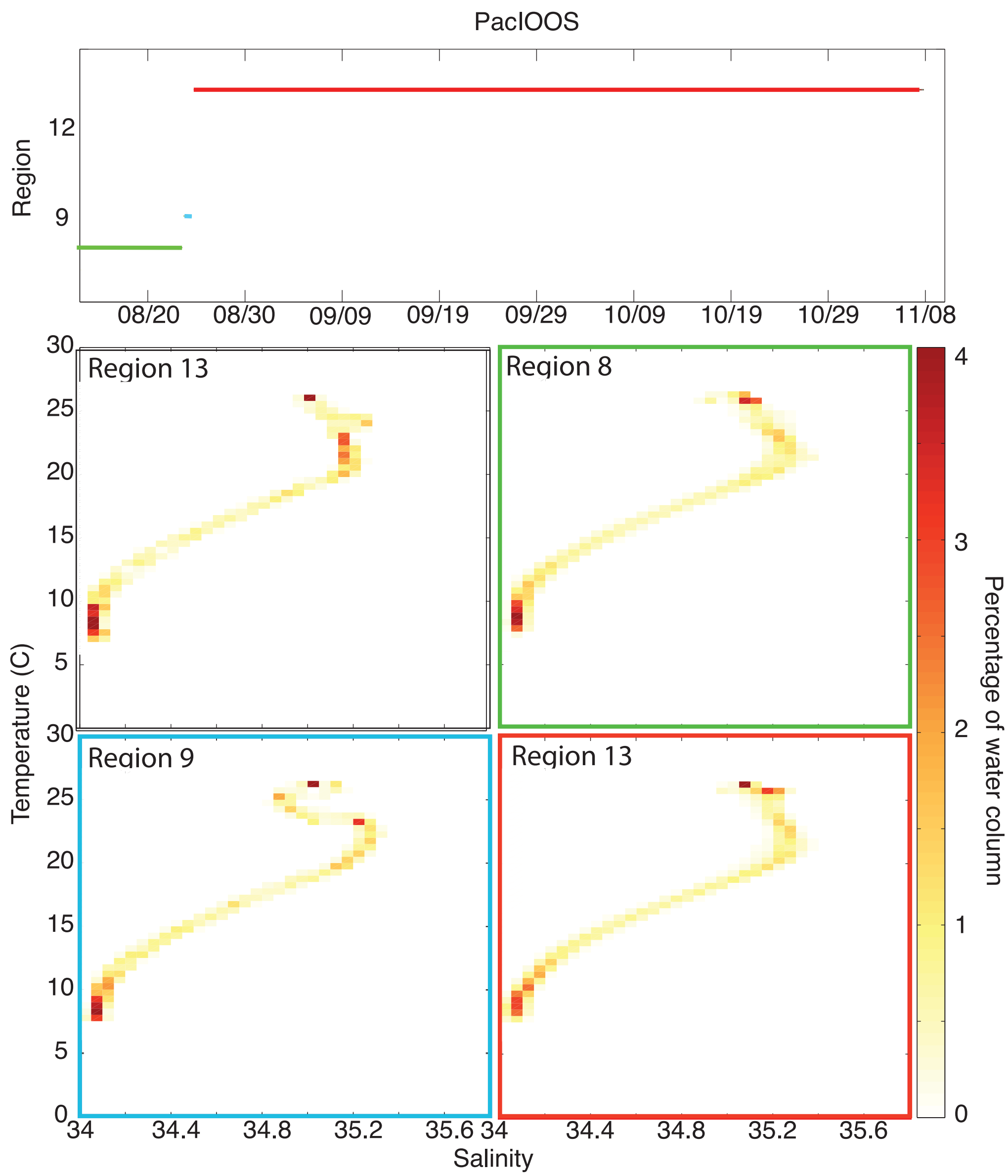

FIGURE 4.9: Top: The Lumpkin [1998] region (Fig. 2.1) of the observed TS curve during PacIOOS 4. The color of the line matches the box surrounding the corresponding percentage of the water column T-S plots shown. Region 8 - (22.5 – 27.5°N, 155 – 165°W), Region 9 - (22.5 – 27.5°N, 145 – 145°W), Region 13 - (17.5 – 22.5°N, 155 – 165°W).

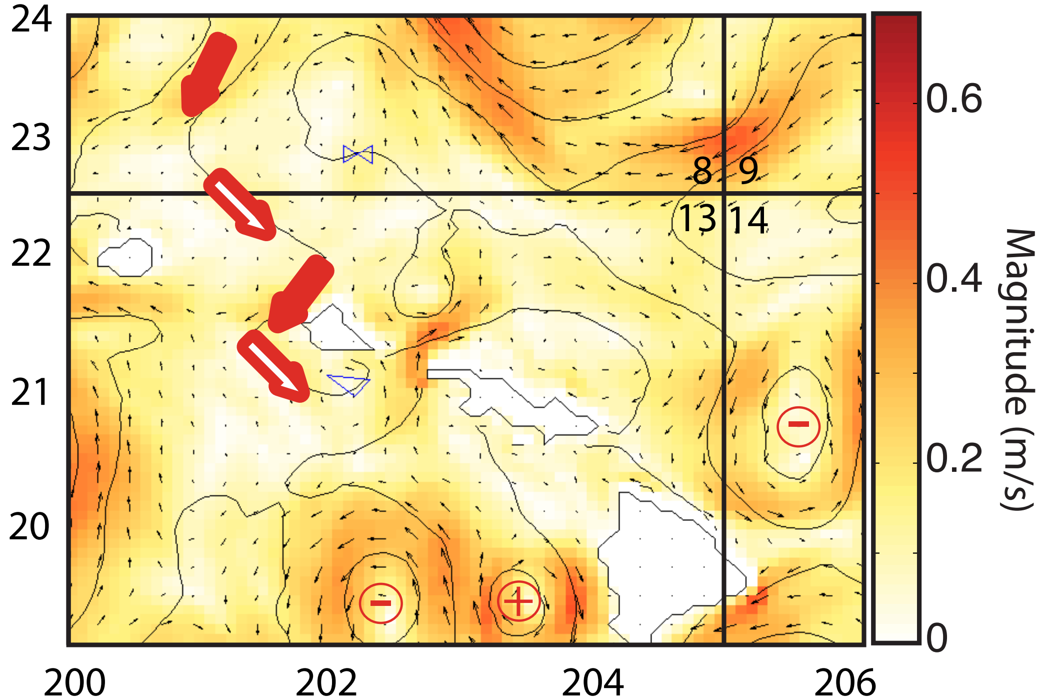

FIGURE 4.10: A plot of the average of the top 50 m velocity vectors from HYCOM 1/12 on August 23. The average flow speed for the upper 50 m is plotted in color. Contours show 2 cm intervals of SSH. The Lumpkin [1998] regions are denoted by the region number (Fig. 2.1). The PacIOOS (triangle) and ALOHA (bow tie) nominal routes are plotted in blue. The + and − indicate positive and negative SSH anomalies.

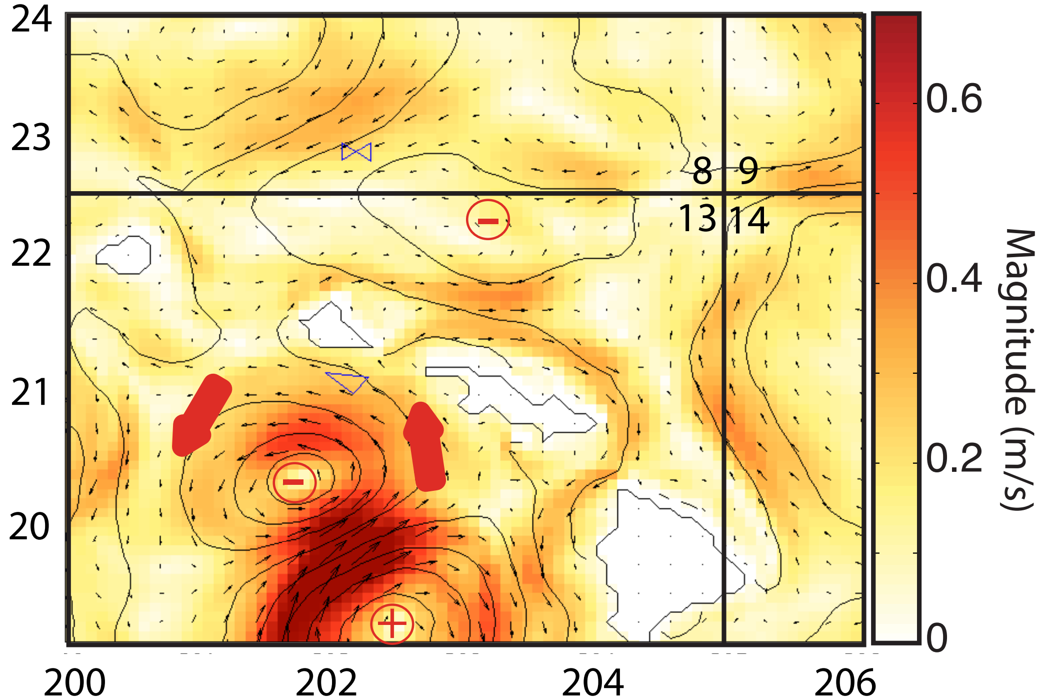

FIGURE 4.11: A plot of the average of the top 50 m velocity vectors from HYCOM 1/12 on September 30. The average flow speed for the upper 50 m is plotted in color. Contours show 2 cm intervals of SSH. The Lumpkin [1998] regions are denoted by the region number (Fig. 2.1). The PacIOOS (triangle) and ALOHA (bow tie) nominal routes are plotted in blue. The + and − indicate positive and negative SSH anomalies.

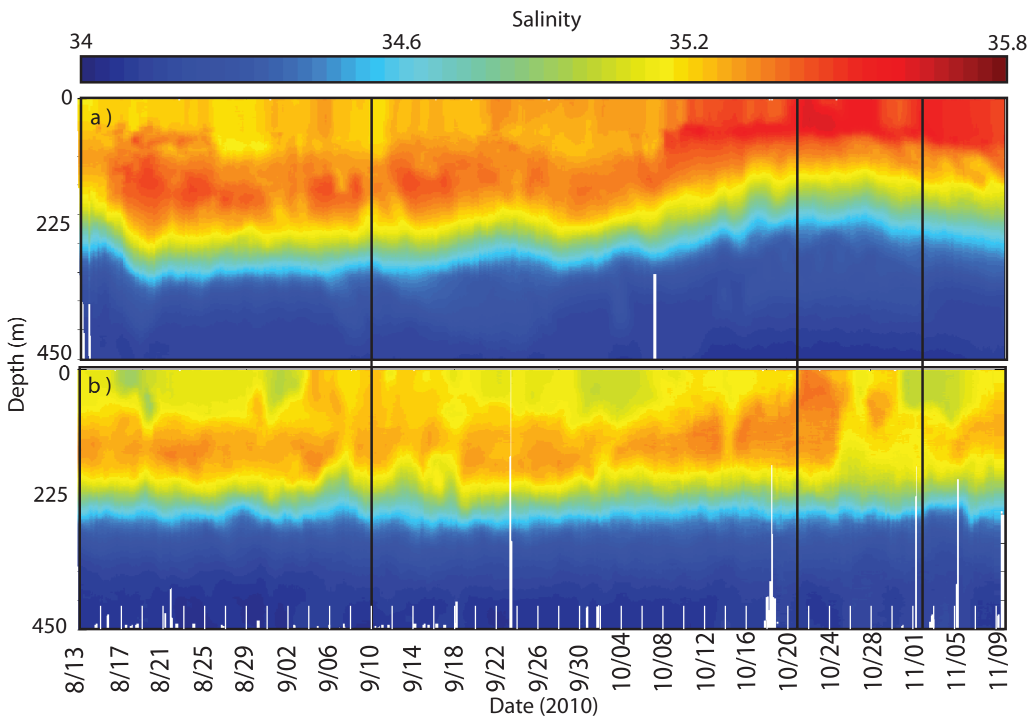

FIGURE 4.12: Salinity vs depth for a) ALOHA 3, b) PacIOOS 4. Vertical lines show the day in the time series corresponding to the SSH and sea surface velocity snapshots (Fig. 4.13, 4.14, 4.15) from left to right. September 10, Fig. 4.13. A salinity anomaly is observed in the PacIOOS dataset while no anomaly is observed in the ALOHA dataset. October 21, Fig. 4.14. A positive salinity anomaly is observed in both the PacIOOS and ALOHA datasets. November 2, Fig. 4.15. A positive salinity anomaly is observed at ALOHA while an average salinity is observed at PacIOOS.

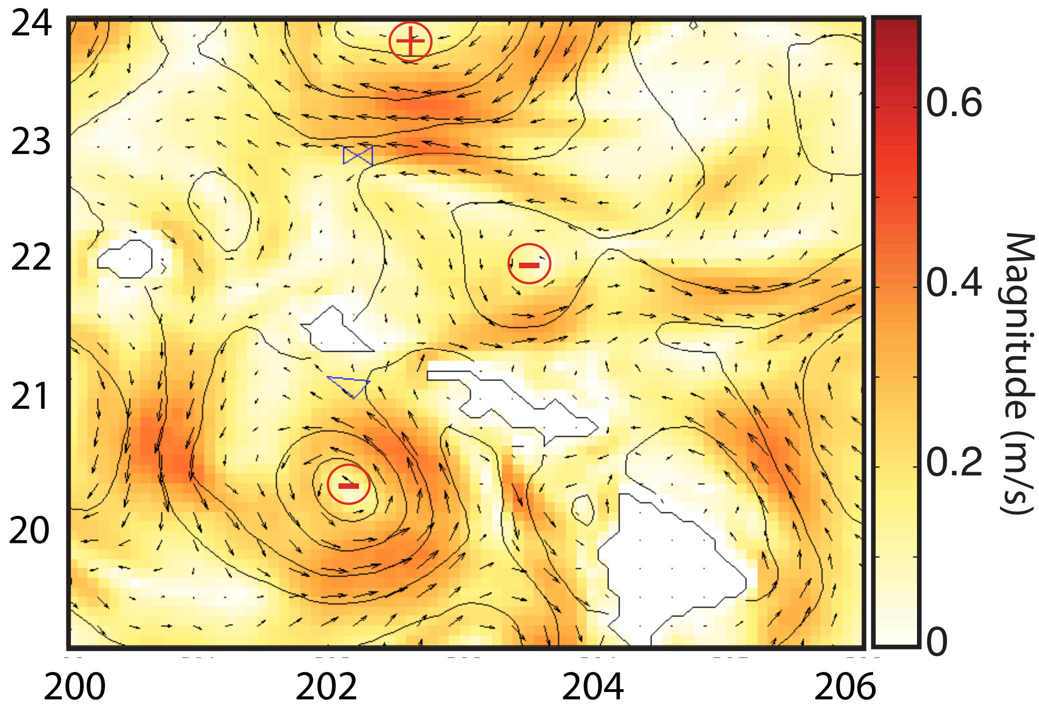

FIGURE 4.13: September 10. The average of the upper 50 m velocity vectors from HYCOM 1/12 are plotted (vectors) with the flow speed plotted in color. Contours plot 2 cm intervals of SSH from HYCOM 1/12.

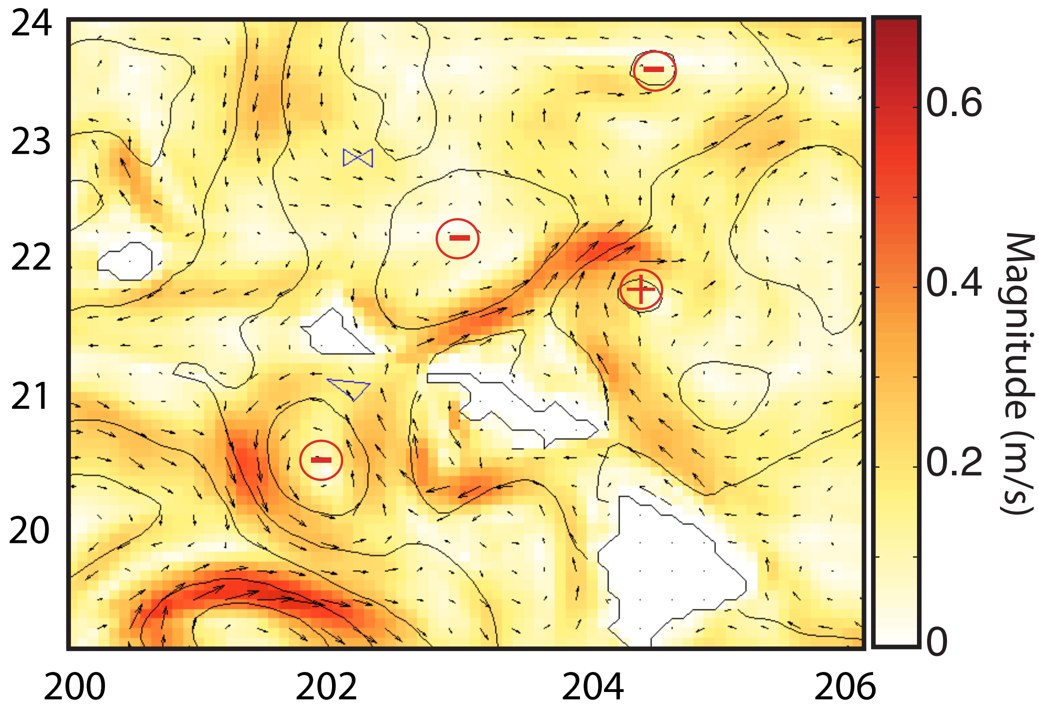

FIGURE 4.14: October 21. The average of the upper 50 m velocity vectors from HYCOM 1/12 are plotted (vectors) with the flow speed plotted in color. Contours plot 2 cm intervals of SSH from HYCOM 1/12.

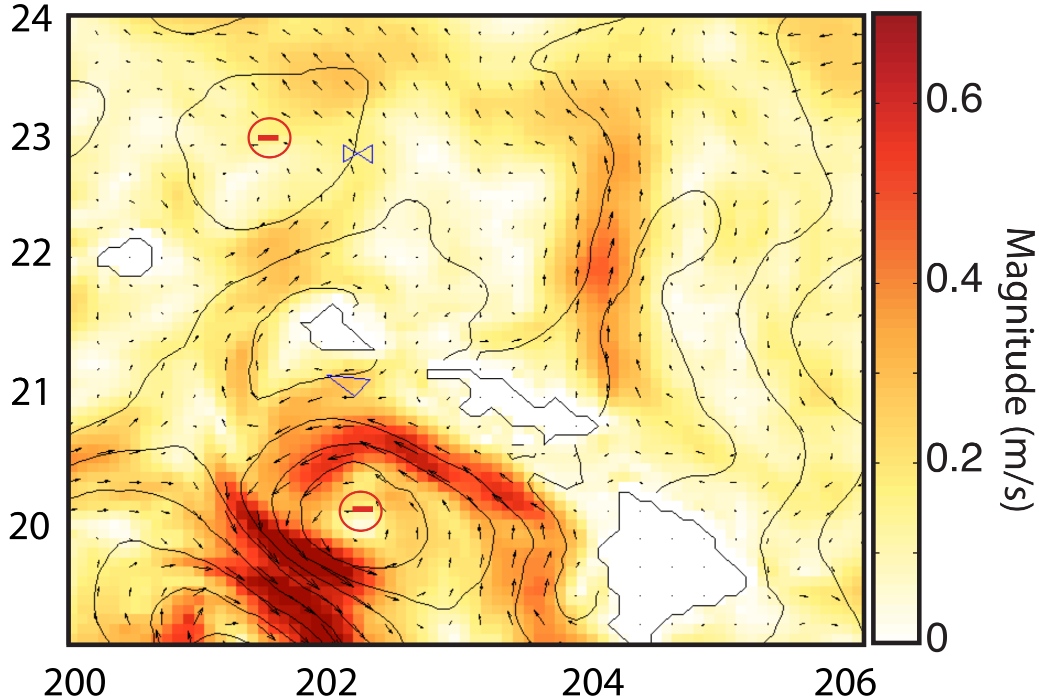

FIGURE 4.15: November 2. The average of the upper 50 m velocity vectors from HYCOM 1/12 are plotted (vectors) with the flow speed plotted in color. Contours plot 2 cm intervals of SSH from HYCOM 1/12.

Chapter 5

Discussion

5.1 North and south of Oahu

Comparing the variation of T-S relationships to the circulation patterns around Hawaii suggested that northward flow through the Kaiwi Channel corresponded to T-S curves most similar to the T-S curve of region 8. Southward flow through the channel corresponded to the average T-S curves north of the islands. Flow through the adjacent channels plays a role in determining water mass properties. In support of this theory, Price et al. [1994] found cold intrusions extending from Alenuihaha channel west-southwest, the extent of the intrusions with depth is not described.

Lumpkin [1998] found the average T-S curve for a grid of 5° by 10° cells. CTD data was compiled from the January 1991 NODC archives, the Global Temperature-Salinity Pilot Project archives, and the World Ocean Atlas 1994. Differences between curves are observed longitudinally and latitudinally. By using RMS to compare each Seaglider profile and the average curves found by Lumpkin [1998]. The PacIOOS T-S curves matched up with six of the regional average profiles. Most of the T-S relationships (62.6%) observed matched those found north of the Islands. Indicating that a strong connection between north and south of the islands. Most of the T-S variation (61.8%) stays within the same longtudinal band, $155 - 165$°W. The T-S curves from the $145 - 155$°W band are observed (25.5%).

5.2 Sea surface salinity anomalies

Agreement amongst available datasets confirms the existence of salinity anomalies with values up to 0.3 and the average positive anomaly of 0.16. High surface salinity was observed in the Aquarius dataset that corresponding to the cyclonic eddies south of the islands. Due to resolution issues near the islands, it is impossible to observe advection of high salinity anomalies into the study site. Argo profiles show positive salinity events, above 35, occurred in the upper 50 m 58% of the time and high salinity events, above 35.2, 22% of the time. In comparison, we see positive salinity events, above 35, occurring over 59% and high salinity events, defined as above 35.2, 14% of the Seaglider missions. Model results for the region vary dramatically. HYCOM predicted, from January 1, 2008 through December 31, 2013, that 22% of the time salinities above 35 would be observed and salinities above 35.2 are predicted to be observed 5% of the time, not matching PacIOOS Seaglider or Argo observations.

The distribution of PacIOOS Seaglider missions is biased heavily towards the summer months whereas the Argo dives, generally, are spread out over the entire year. PacIOOS 7 has the highest percentage of occurrence of salinity anomalies followed by PacIOOS 4. PacIOOS 4 occurred during the later parts of the summer and fall into the early winter months. PacIOOS 2, 3, 5, 6 and 7 are all in the spring and summer months and show similar low percentages of salinity anomalies. PacIOOS 4 and 5 show a slight increase in the number of salinity anomalies over PacIOOS 2 and 6. PacIOOS 4 and 5 occurred at least partially in the late spring whereas PacIOOS 2 and 6 occurred solely in the summer months. The Seaglider data suggests that the number of salinity anomalies is variable based on the season with high numbers of events occurring during the winter with a gradual ramp down of events through the spring resulting in a low number of events over the summer followed by a ramp up through the fall to winter. Data spanning all seasons is needed to confirm this hypothesis

All available Argo missions from January 1, 2008 through December 31, 2013 spanning from 19°N to 21.366°N and 157°W to 159°W were used to provide seasonal coverage (Appendix C). Analysis showed high salinity occurs for a larger percentage of time during the late fall and winter months. More data is needed to confirm high salinity events.

Eddies are formed through the interaction of the trade winds with the Big Island of Hawaii. The consistency of eddies in the region is attributed to the consistency of trade winds across the Big Island. There is an annual cycle to the persistence of the wind with a low (0.6 of the time) in winter and a maximum of 0.98 in the summer [Garza et al., 2012]. The decrease in persistence during the winter months results in a decrease of the westward propagation speed of the eddies as well as an increase in the spin-up time. It was observed during this study (in SSH satellite observations) that during the winter months the newly formed eddies reside in the region of the Hawaiian Islands longer than during the summer months. It is suspected that the residence time or speed of westward propagation is inversely related to the persistence of the wind. That leads to the belief, the increased residence time allows for more interaction through the channels and results in increased occurrence of salinity anomalies.

Based on HYCOM SSH the PacIOOS study region is in a negative sea surface anomaly state approximately 52% of the time period from January 1, 2008 through December 31, 2013. We see a spike in the number of negative SSH days in 2009 which has a corresponding to the increase in the number of salinity anomaly. 2009 was skewed due to the heavy sampling in the early part of the year where a strong negative SSH height dominated. When the SSH is broken down into months, the lowest percentage of negative SSH days occurs during the late summer months, June through September, while the highest percentage of negative SSH days occurs during the late winter months, January through April.

The source of anomalous water appears to be the subsurface salinity maxima, water formed in the warm saline pool north of the islands (just south of 30°N, where evaporation exceeds precipitation). This water is advected along the subtropical gyre to the southwest, and subducted under the warmer, less dense waters found to the south. South of the Hawaiian Islands the subsurface salinity maxima is observed at a depth of 100-120 m. HYCOM showed a high salinity event always corresponds to a lee cyclonic eddy but a lee cyclonic eddy does not always imply a high salinity event. Big Island lee cyclonic eddies cause outcropping of the $100 - 120$ m isotherms allowing high salinity water from the subsurface salinity maximum to be lifted to the surface. A corresponding northern eddy interacts with the lee eddy causing deformation and a loss or transfer of mass. Advection of the high salinity waters occurs through the Kaiwi channel.

Over the course of this research, 2008-2013, a low SSH though the Kaiwi channel occurred 52% of the time in SSH data, 59% of the time in Seaglider data, and 58% of the time in Argo data while high salinity anomalies occur 14% of the time in Seaglider data and 22% of the time in Argo data. Over a year, the anomalies occurred inconsistently through the seasons in both Seaglider and Argo profiles with more positive and high positive events occurring in the fall and early winter months. Summer missions showed the least amount of positive and extreme positive events and late spring missions showed a moderate amount of positive and extreme positive events. The more even temporal distribution of Argo profiles clearly show an increase in events during the fall and winter and a lessening of events during the spring into the summer.

There are nine channels in the main Hawaii Island chain (Alalakeiki, Kealaikahiki, Auau, Pailolo, Kaulakahi, Ka'ie'ie, Kaiwi, Kawai and Alenuihaha channels, Fig. 2.12), all possible pathways for eddy-eddy interaction to occur. The Kaiwi, Kawai and Alenuihaha are the widest channels and hence should allow the most eddy-eddy interaction. The glider path is located at the base of the Kaiwi channel. Satellite sea surface contours as well as model output of velocities show eddies interacting in the Kaiwi channel causing the high salinity water to advect northwest from the cold cores of Big Island lee eddies into the study site.

5.3 Seaglider usage

Comparisons of Seaglider data with models indicate a high degree of difficulty in predicting temperature and salinity profiles for the region south of Oahu. Variability occurs at all depths with no dominant seasonal forcing. Model-Seaglider comparisons show minimal success, especially in the upper 50 m. The ROMS model does not provide an accurate description of any of the observed variables at the PacIOOS site. HYCOM provides similar surface velocity measurements but does not provide similar profiles of measured variables (salinity and temperature).

Seagliders are an excellent tool to observe anomalies, T-S relationships, water mass variation, eddies, etc. The duration of a mission allows for concentrated observations of infrequent anomalies. Care is required in the processing of Seaglider data due to the variable sampling rate and unpumped conductivity sensor. The region surrounding the Hawaiian Islands is constantly changing, a multi-month mission of a Seaglider provides a useful snapshot of the variation not available through other observational methods.

Chapter 6

Conclusion

- The water properties and variation of water properties at ALOHA and in the PacIOOS areas do not appear to be related with each location being distinct at all depths. The T-S curves identified for each region vary throughout the course of a mission as well as between missions. STD calculations indicate the largest variations in the T-S curve (at both ALOHA and PacIOOS sites) occur in the upper portion of the water column, with a secondary component at the salinity minimum occurring at the PacIOOS site.

- High salinity anomalies are observed during periods of time where two cyclonic eddies are located on either side (north and south) of Oahu and submesoscale interaction occurs between the two eddies through the Kaiwi channel. The spin up of cyclonic eddies in the lee of the Big Island cause the 120 m isotherms to outcrop forcing high salinity water to the surface. As the eddies interact, this water is advected through the channel, and as a result through the PacIOOS study site.

6.1 Improved sampling

Seagliders are an excellent tool to observe T-S relationships, water mass variation, eddies, etc. The variable sampling rate and extended length of data sets allow for concentrated observations of infrequent anomalies. The region surrounding the Hawaiian Islands is constantly changing, a multi-month mission of a Seaglider provides a useful snapshot of the variation not available through other observational methods. However, this data has room for improvement. At both sites, the Seaglider data would be greatly improved by taking a CTD profile upon deployment and recovery. The Seaglider is deployed off a small boat making a hand lowered CTD (SBE 19) necessary. Another improvement would be pre and post calibrations. The pressure sensor could be calibrated in house while the temperature and conductivity sensors would have to be calibrated at Seabird.

Future missions should require a log of time and pressure upon deployment and recovery of the Seaglider. Also, it has been requested that future OTG tests take place at 21°N, 158°W, providing CTD profiles for the PacIOOS site.

Less variation occurs at deeper depths. A deeper dive, 800 - 1000 m, coinciding with HOT cruises would provide an better representation of differences between dives as well as a larger data set to compare against HOT CTD profiles. If the Seaglider travelled near the WHOTS buoy, we could compare the simultaneous temperature measurements for the upper 150 m.

6.2 Possible Further Work

Three other channels have potential eddy interaction that could result in similar salinity anomalies. A hypothesis is, if observations were made near the southern end of the Alenuihaha, Pailolo, or Kaieiewaho channels, similar variations and anomalies would be observed. It would follow that observations at the northern mouth of these same channels and Kaiwi channel would see similar variations. If future missions were to be flown, observations in a nearby channel would provide data to confirm the horizontal spatial degree of interactions and flow through the channels.

A more complete description of the region would be possible if PacIOOS missions flew through the winter months. Current hypothesis for winter events and variability are based on the HYCOM 1/12 degree model output. Seaglider data indicated a high degree of difficulty in predicting temperature and salinity profiles for the region south of Oahu. Variability occurs at all depths with no dominant seasonal character. Model and Seaglider comparisons show little agreement, especially in the upper 50 m. Because of the lack of winter Seaglider observations, winter model predictions are highly suspect.

6.3 A proposed experiment

In order to observe the extent of salinity anomalies, I would propose an experiment consisting of 4 Seagliders. One Seaglider would be nominally transversing the PacIOOS site triangle while a second Seaglider would concurrently be traveling back and forth between the northern tip of Oahu and Molokai. Upon observation of a cyclonic eddy off the south shore of Oahu, a Seaglider would be deployed to take cross sections of the width of the eddy. When a salinity anomaly is observed in the PacIOOS site Seaglider, the PacIOOS Seaglider would be directed to follow the high salinity by traveling up the Kaiwi channel in a zig-zag pattern. The fourth Seaglider would be deployed to continue data collection at the PacIOOS site.

Appendix A

Comparison of Seaglider profiles to Argo Profiles

This appendix simply compares individual glider profiles to profiles from the Argo dataset. The Argo profiles listed in tables 1-6 are between 19°N and 22°N, 157°W and 159°W, and are within the time frame of a glider mission. Each figure shows a comparison of all available Argo float profiles (temperature - black, salinity - gray, TS - black) with the closest glider mission in time (temperature - red, salinity - dark blue, TS - red) and the glider legs immediately proceeding and following (temperature - cyan, salinity - magenta). At times due to glider errors a leg is not available or not available for the full 500m profile. These are not plotted or plotted as much as possible, respectfully. Each table shows the distance from the glider's GPS latitude and longitude to the Argo float. The angle describes the direction from north.

Table A.1: Argo profiles during Mission 2.

Mission 2 July 09, 2008 - August 20, 2008				
Panel	Date	Float Number	Distance	Angle
a	11-Jul-2008 15:55:31	5900584	159.9366	349.0043
b	22-Jul-2008 04:37:05	5900584	117.4964	731.0021
c	01-Aug-2008 18:32:16	5900584	79.731	1113.002
d	12-Aug-2008 07:13:55	5900584	87.9534	1495.002
e	01-Aug-2008 10:51:07	2900829	163.7218	1877.0024
f	05-Aug-2008 11:47:22	2900829	132.2614	2259.002
g	03-Aug-2008 02:56:21	2900831	71.1702	2641.002
h	07-Aug-2008 02:58:32	2900831	80.3762	3023.002
i	11-Aug-2008 02:58:58	2900831	102.7646	3405.002

Table A.2: Argo profiles during Mission 3.

Mission 3 April 12, 2010 - July 14, 2010				
Panel	Date	Float Number	Distance	Angle
a	08-Jul-2010 01:10:39	5900584	216.0813	349.005

Table A.3: Argo profiles during Mission 4.

Mission 4				
July 27, 2010 - November 10, 2010				
Panel	Date	Float Number	Distance	Angle
a	31-Oct-2010 23:21:06	5900584	153.0189	349.0057
b	26-Jul-2010 02:51:48	2900828	221.5726	731.0028
c	30-Jul-2010 02:53:37	2900828	190.898	1111.0026
d	08-Sep-2010 02:53:22	2900828	129.551	1493.0026
e	12-Sep-2010 02:51:42	2900828	84.7656	1875.0032
f	16-Sep-2010 02:50:43	2900828	103.1067	2257.0026

Table A.4: Argo profiles during Mission 5.

Mission 5 April 5, 2011 - May 24, 2011				
Panel	Date	Float Number	Distance	Angle
a	03-Apr-2011 19:31:10	5900947	151.0119	349.0065
b	14-Apr-2011 11:09:39	5900947	112.0042	729.0034
c	24-Apr-2011 23:55:35	5900947	98.4872	1111.0032
d	05-May-2011 12:55:48	5900947	73.9433	1493.0032
e	16-May-2011 01:51:56	5900947	50.4638	1875.0039
f	03-Apr-2011 00:10:30	5902155	107.0691	2257.0032
g	07-Apr-2011 00:18:40	5902155	87.2117	2637.0026
h	11-Apr-2011 00:07:47	5902155	86.9635	3019.0026
i	06-Apr-2011 04:06:08	5902157	13.9803	3401.0026
j	10-Apr-2011 16:07:06	5902157	25.9668	3783.0011
k	14-Apr-2011 03:47:16	5902157	2.2874	4165.0007
l	18-Apr-2011 03:59:08	5902157	11.4907	4547.0007
m	22-Apr-2011 03:54:07	5902157	9.6794	5102.0007
n	26-Apr-2011 04:00:06	5902157	28.484	5484.0012
o	30-Apr-2011 05:12:03	5902157	16.7736	5866.0007
p	04-May-2011 05:20:14	5902157	47.2787	6248.0007
q	08-May-2011 05:09:22	5902157	37.5161	6630.0007
r	12-May-2011 05:15:20	5902157	27.9811	7012.0012
s	16-May-2011 03:53:19	5902157	25.7197	7394.0002
t	20-May-2011 03:47:34	5902157	39.6513	7776.0001
u	03-Apr-2011 15:35:39	5902158	173.1844	8158.0001
v	07-Apr-2011 04:58:38	5902158	157.6506	8538.0002
w	11-Apr-2011 04:51:05	5902158	122.4156	8920.0001
x	15-Apr-2011 04:53:30	5902158	104.8752	9302.0001
y	19-Apr-2011 04:56:41	5902158	101.681	9857.0001
z	23-Apr-2011 04:43:47	5902158	84.8969	10239.0001
aa	27-Apr-2011 04:49:16	5902158	71.1379	10621.0005
bb	01-May-2011 04:55:30	5902158	57.523	11003.0001
cc	05-May-2011 04:44:07	5902158	40.2363	11385.0001
dd	09-May-2011 04:46:32	5902158	52.8839	11767.0001
ee	13-May-2011 04:42:03	5902158	36.0315	12149.0005
ff	17-May-2011 14:32:29	5902158	28.2384	12531.0001
gg	21-May-2011 04:53:01	5902158	56.4041	12913.0001

Table A.5: Argo profiles during Mission 6.

Mission 6 June 13, 2011 - July 30, 2011				
Panel	Date	Float Number	Distance	Angle
a	16-Jun-2011 16:51:29	5900947	41.2116	349.0072
b	27-Jun-2011 05:50:39	5900947	37.5855	731.004
c	07-Jul-2011 20:15:56	5900947	91.5432	1113.0038
d	13-Jun-2011 05:10:22	5902157	94.4348	1495.0038
e	17-Jun-2011 05:22:55	5902157	88.3769	1875.0046
f	21-Jun-2011 05:20:50	5902157	89.5001	2257.0038
g	25-Jun-2011 05:25:21	5902157	122.9056	2639.0032
h	29-Jun-2011 05:16:40	5902157	118.6119	3021.0032
i	14-Jun-2011 04:50:37	5902158	91.3762	3403.0032
j	18-Jun-2011 14:16:32	5902158	50.8366	3785.0017
k	22-Jun-2011 04:57:46	5902158	55.7847	4167.0013
l	26-Jun-2011 04:54:03	5902158	29.8692	4549.0013
m	30-Jun-2011 04:54:56	5902158	50.2865	5104.0013
n	04-Jul-2011 04:46:37	5902158	49.3373	5486.0021
o	08-Jul-2011 04:52:05	5902158	105.2084	5868.0013

Table A.6: Argo profiles during Mission 7.

Mission 7 April 25, 2013 - July 26, 2013				
Panel	Date	Float Number	Distance	Angle
a	26-Apr-2013 03:25:55	5901041	138.0635	349.0079
b	06-May-2013 21:36:04	5901041	94.3213	731.0046
c	17-May-2013 15:39:31	5901041	87.266	1113.0044
d	28-May-2013 08:41:37	5901041	115.4871	1495.0044
e	08-Jun-2013 03:48:31	5901041	138.7847	1877.0054
f	29-Jun-2013 12:44:59	5901041	172.065	2259.0044
g	10-Jul-2013 09:38:14	5901041	114.5262	2641.0038

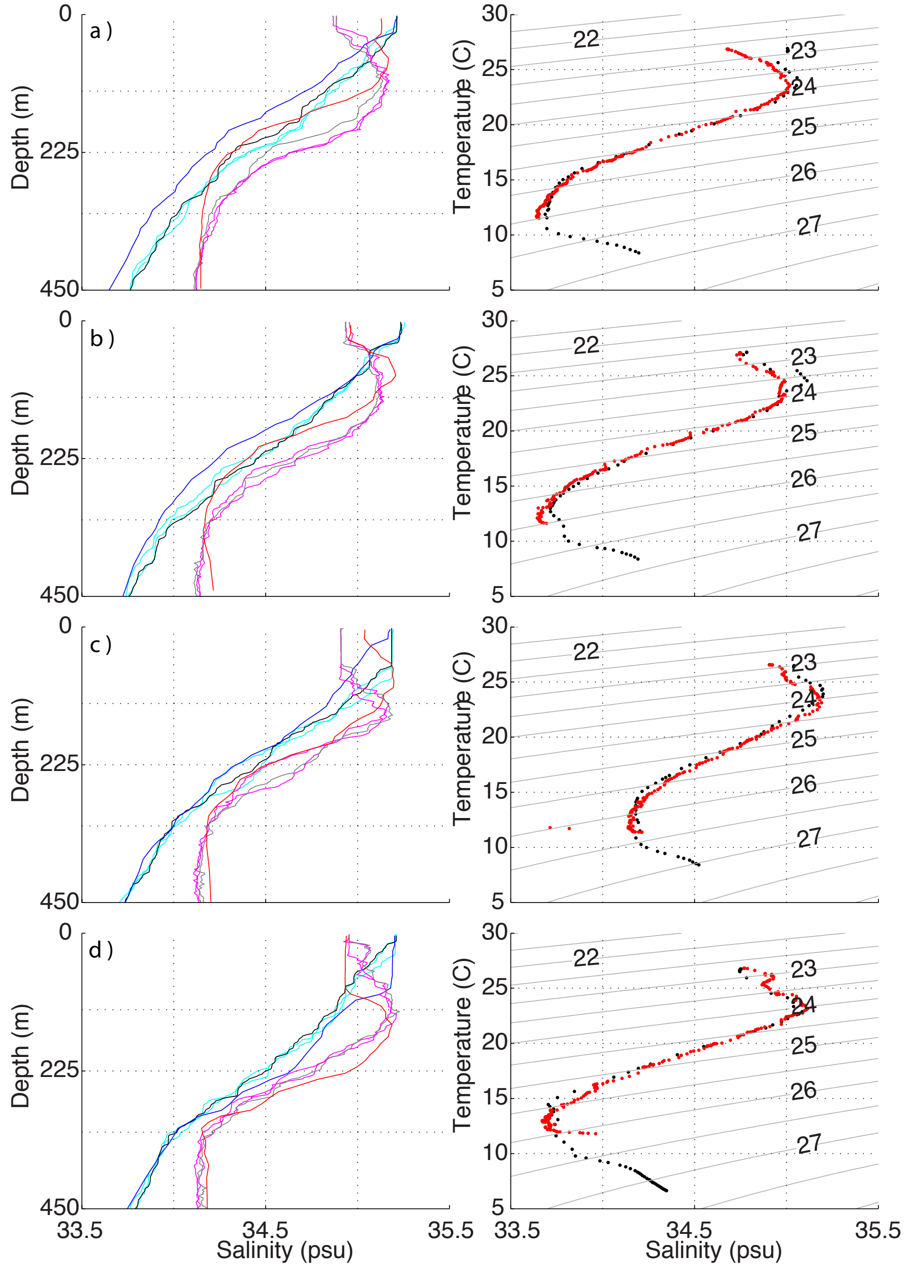

FIGURE A.1: Mission 2

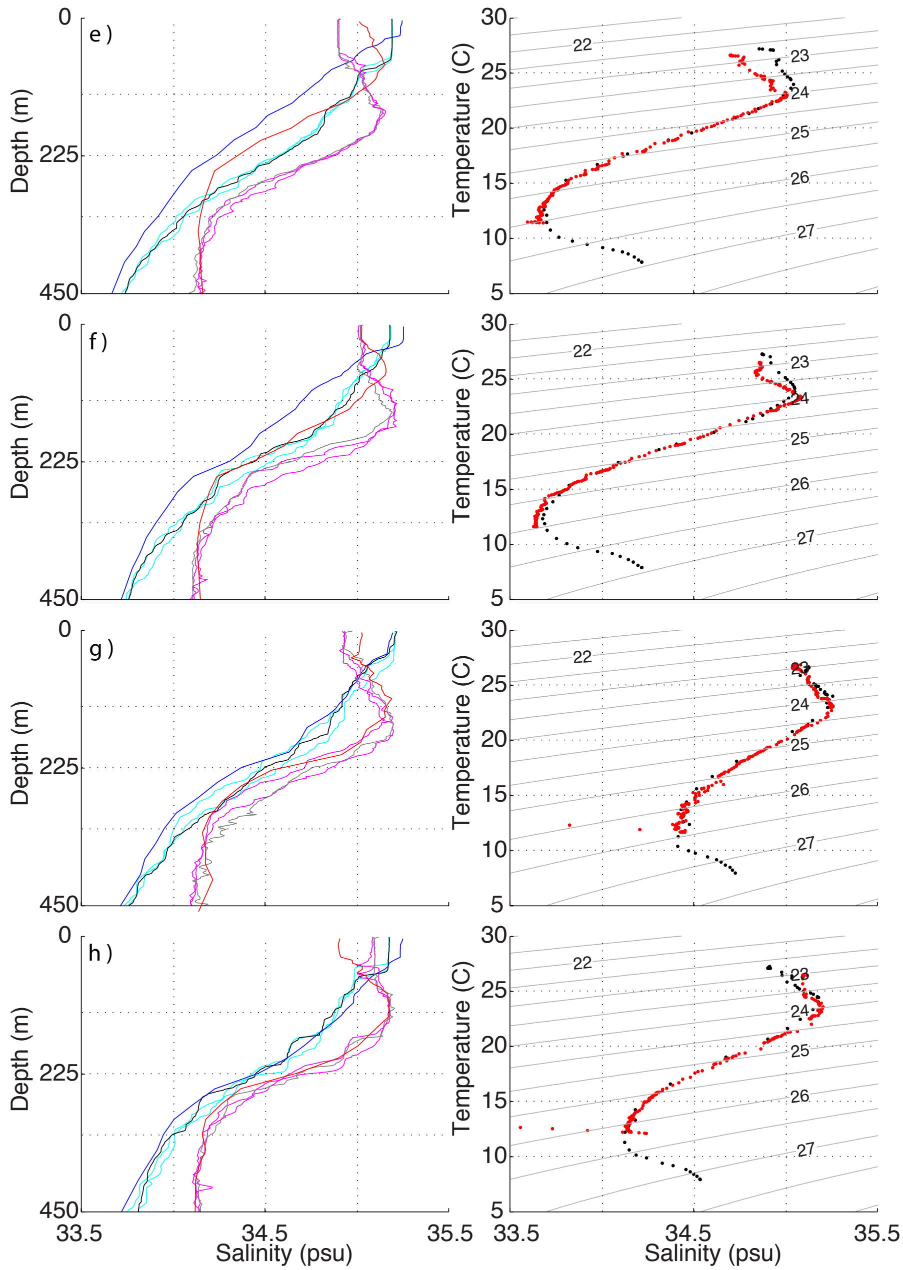

FIGURE A.2: Mission 2 continued

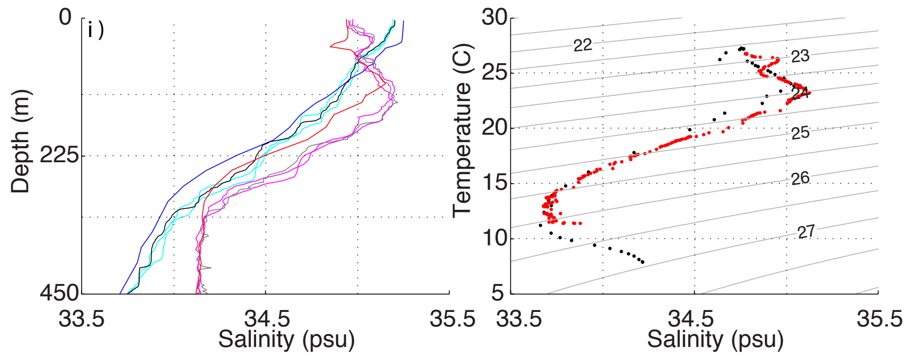

FIGURE A.3: Mission 2 continued

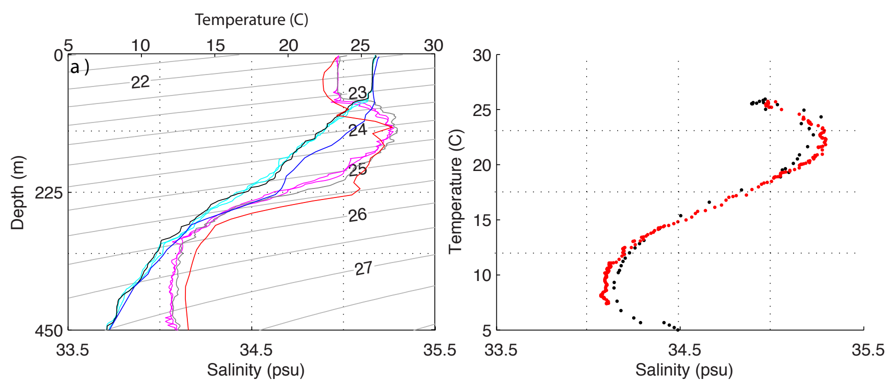

Figure A.4: Mission 3

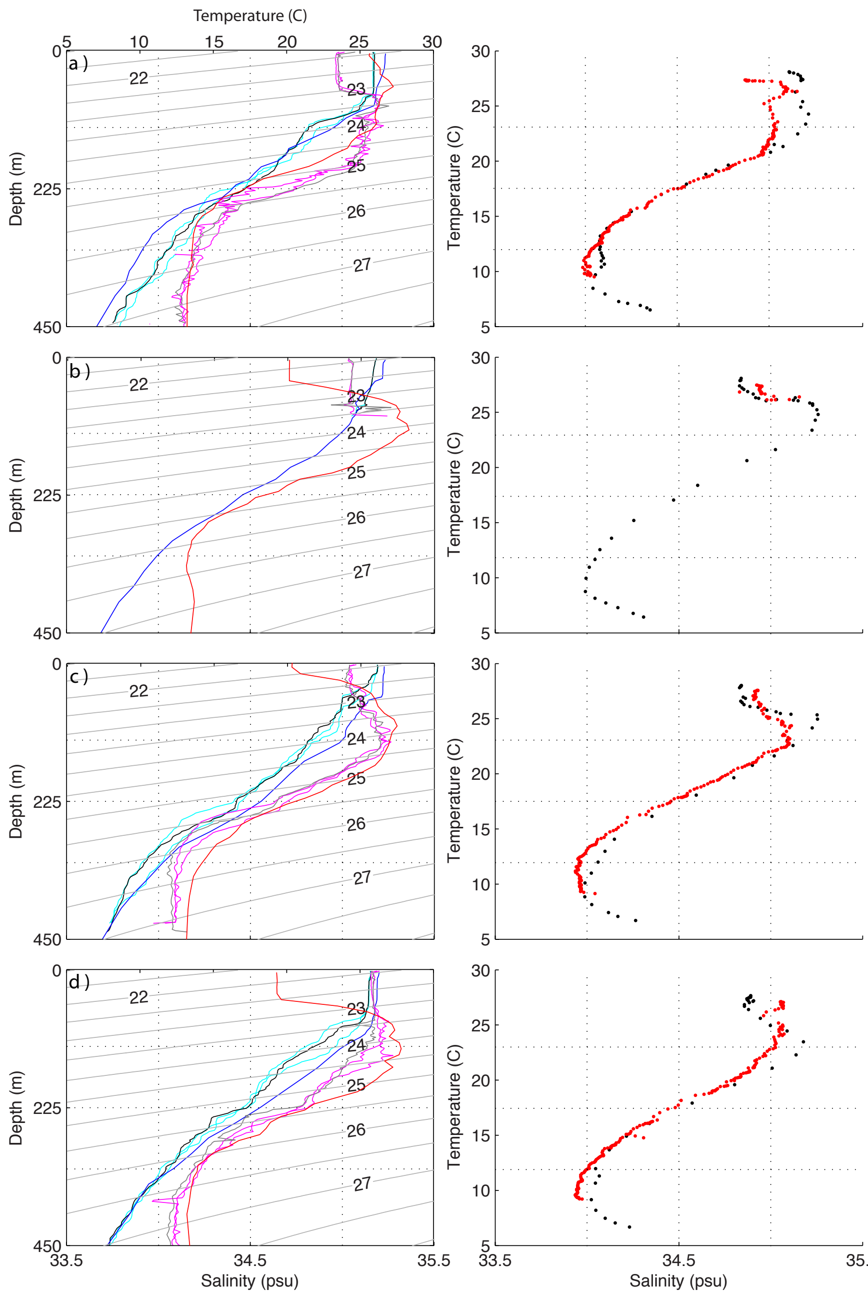

FIGURE A.5: Mission 4

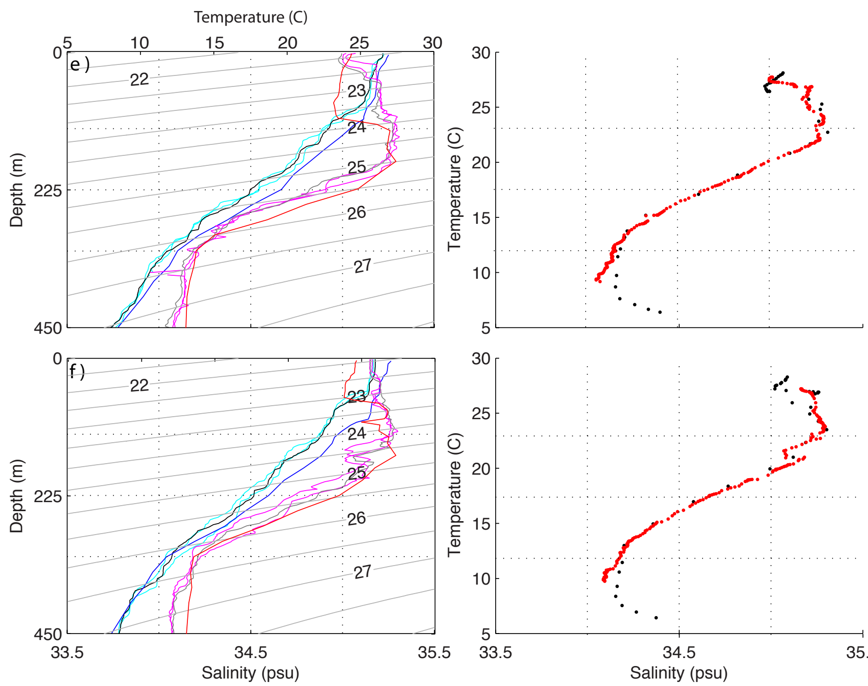

FIGURE A.6: Mission 4 continued

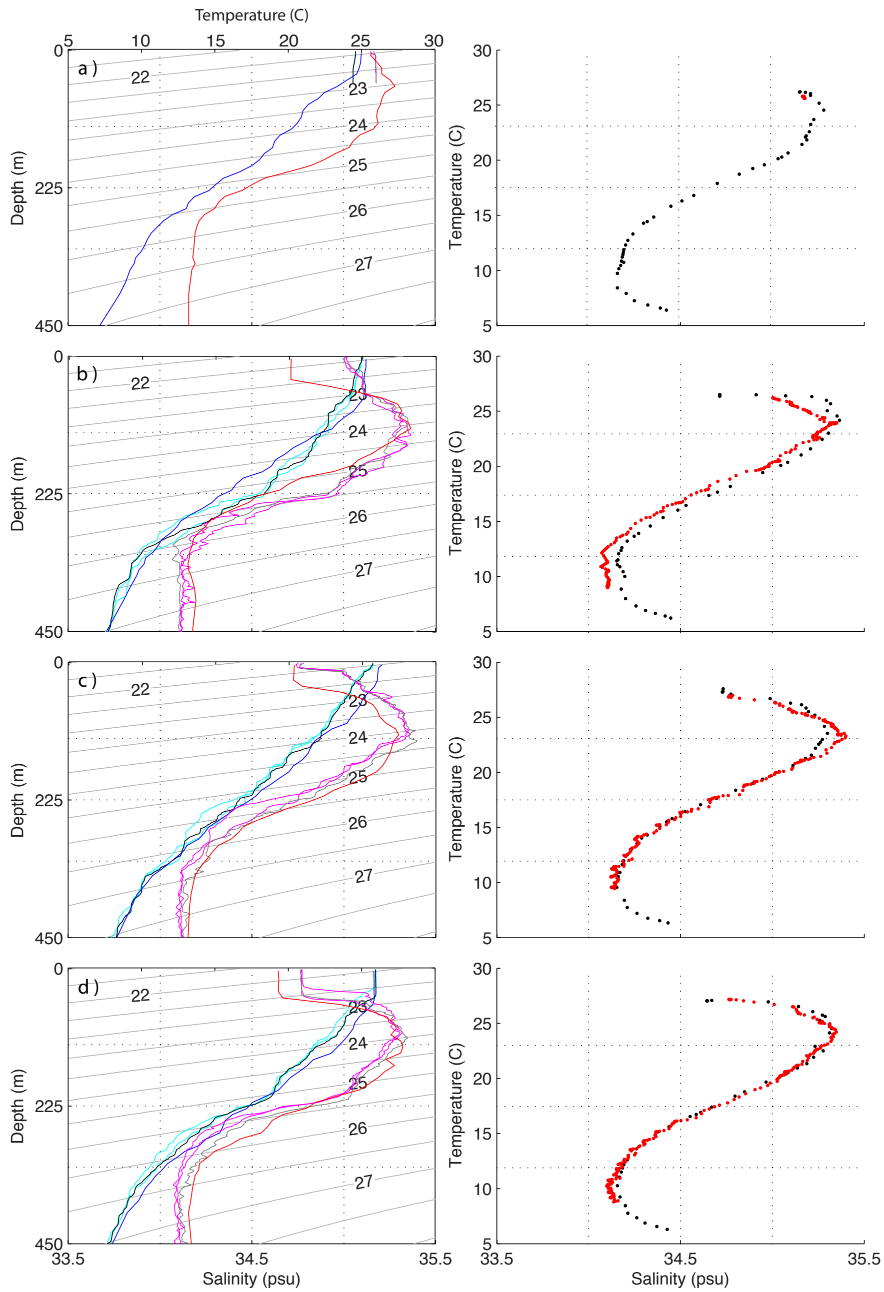

FIGURE A.7: Mission 5

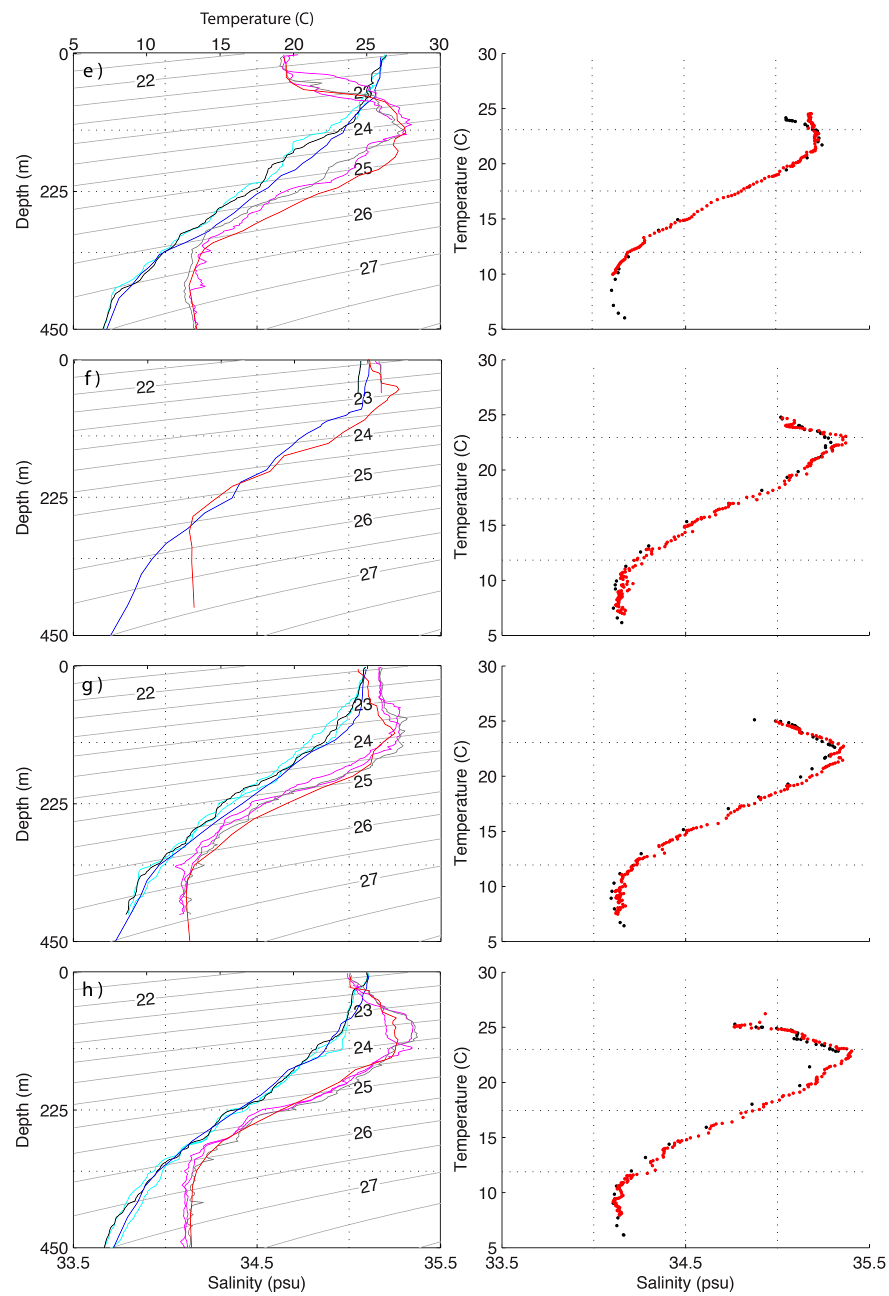

FIGURE A.8: Mission 5 continued

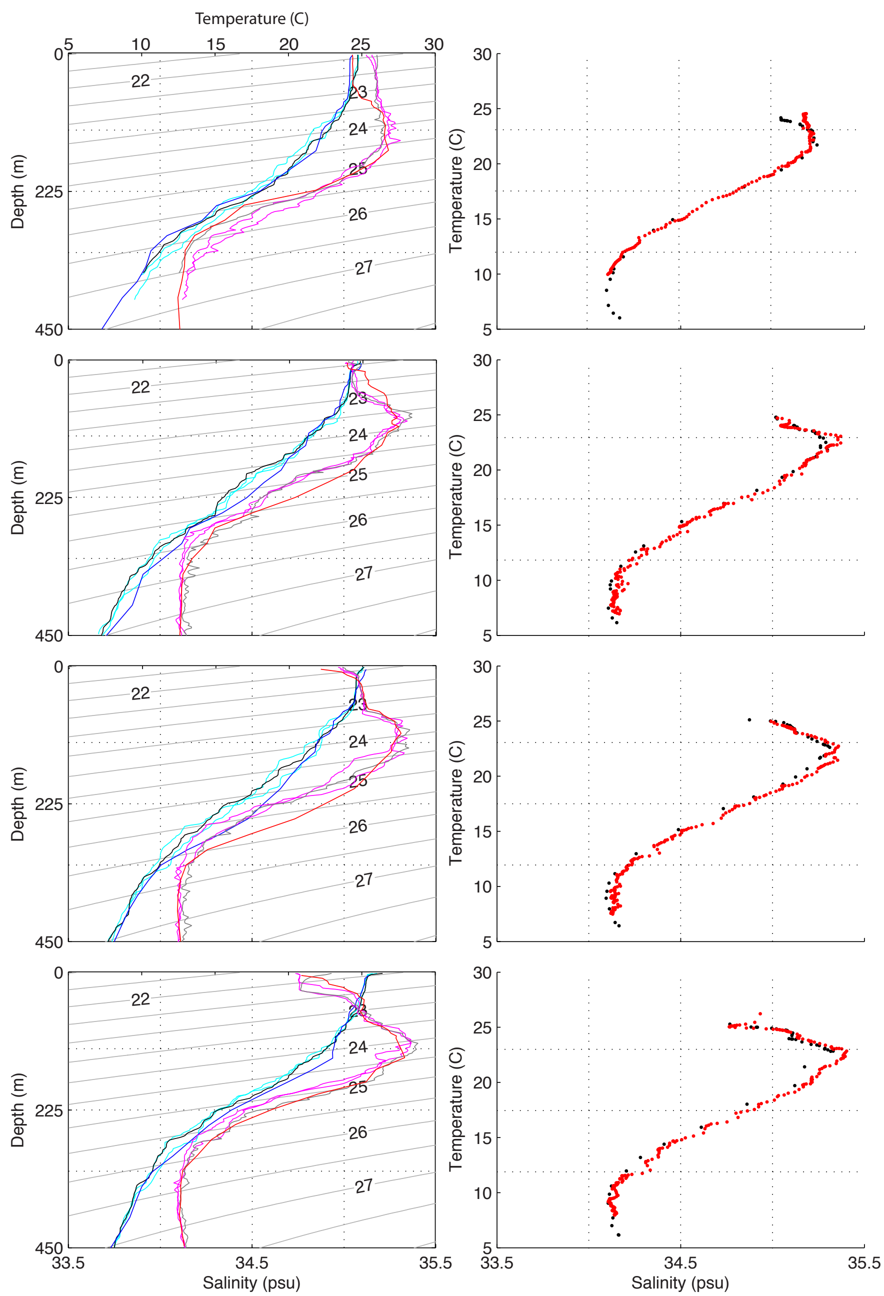

FIGURE A.9: Mission 5 continued

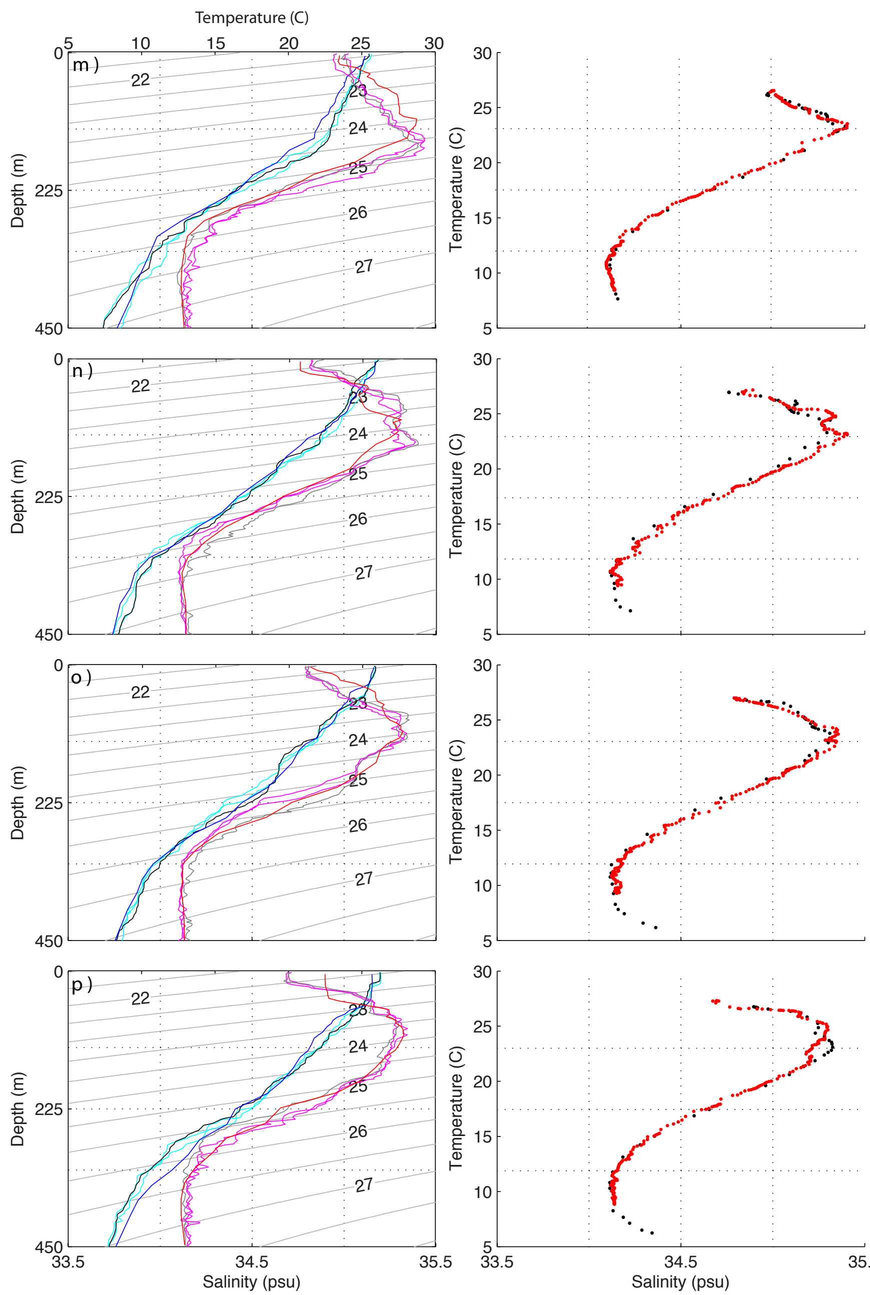

FIGURE A.10: Mission 5 continued

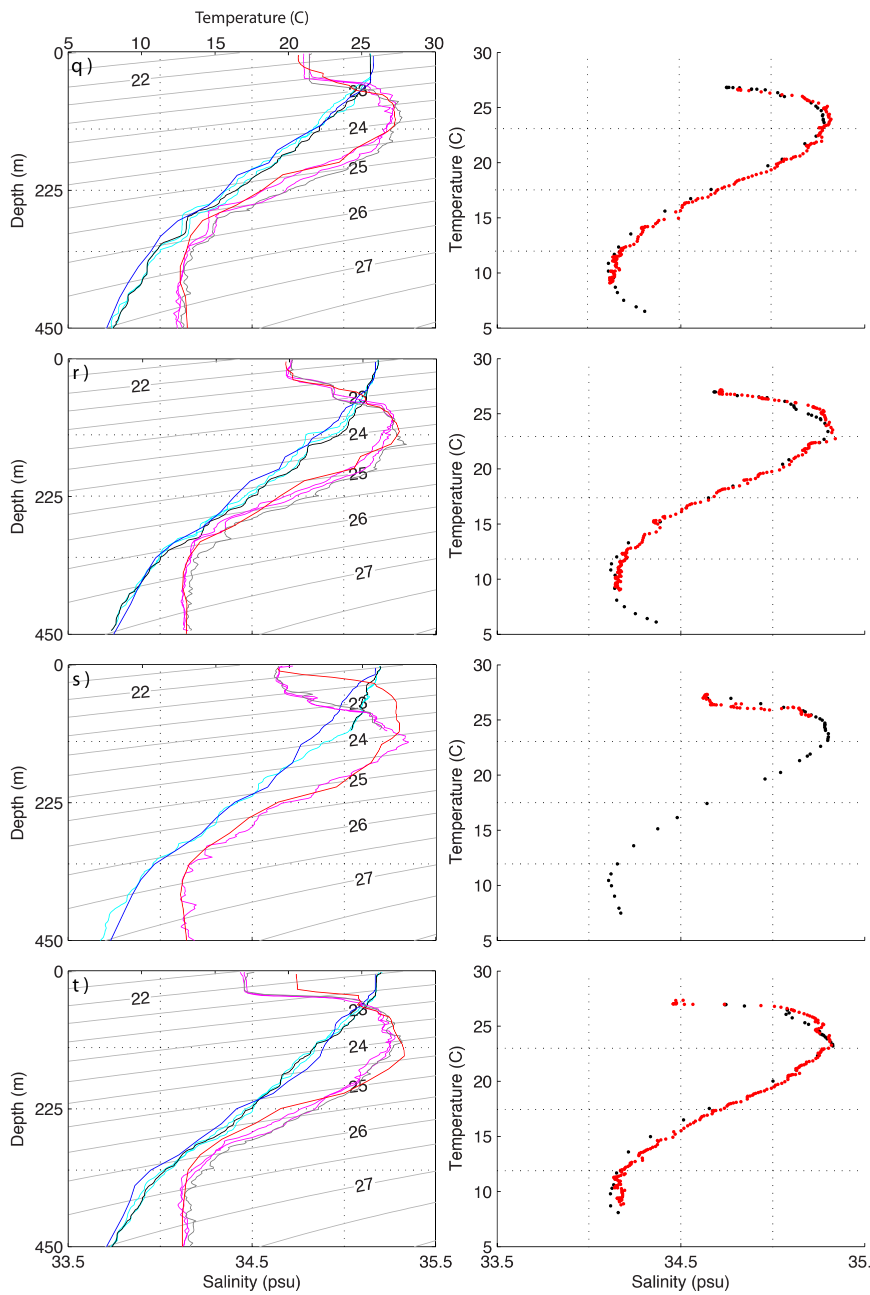

FIGURE A.11: Mission 5 continued

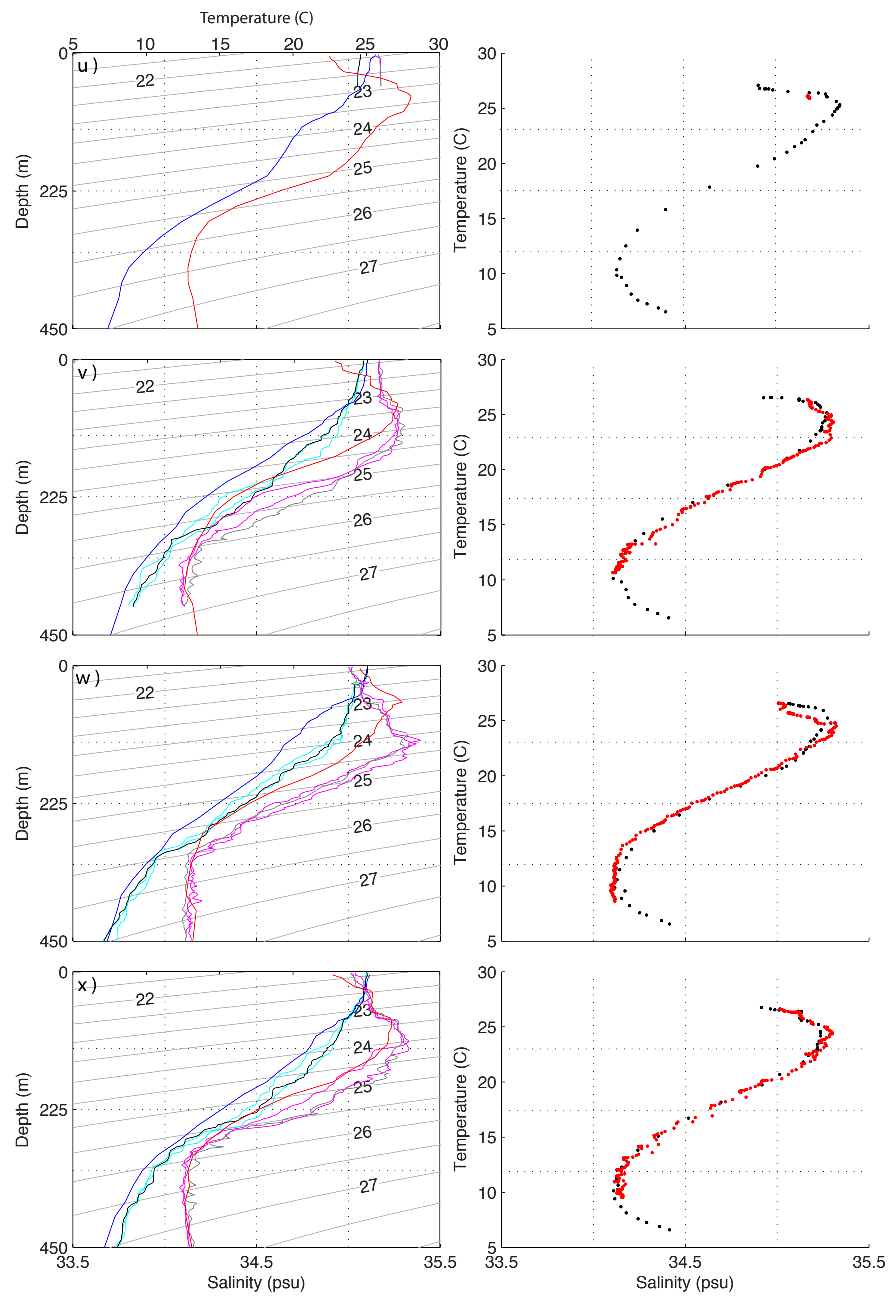

FIGURE A.12: Mission 5 continued

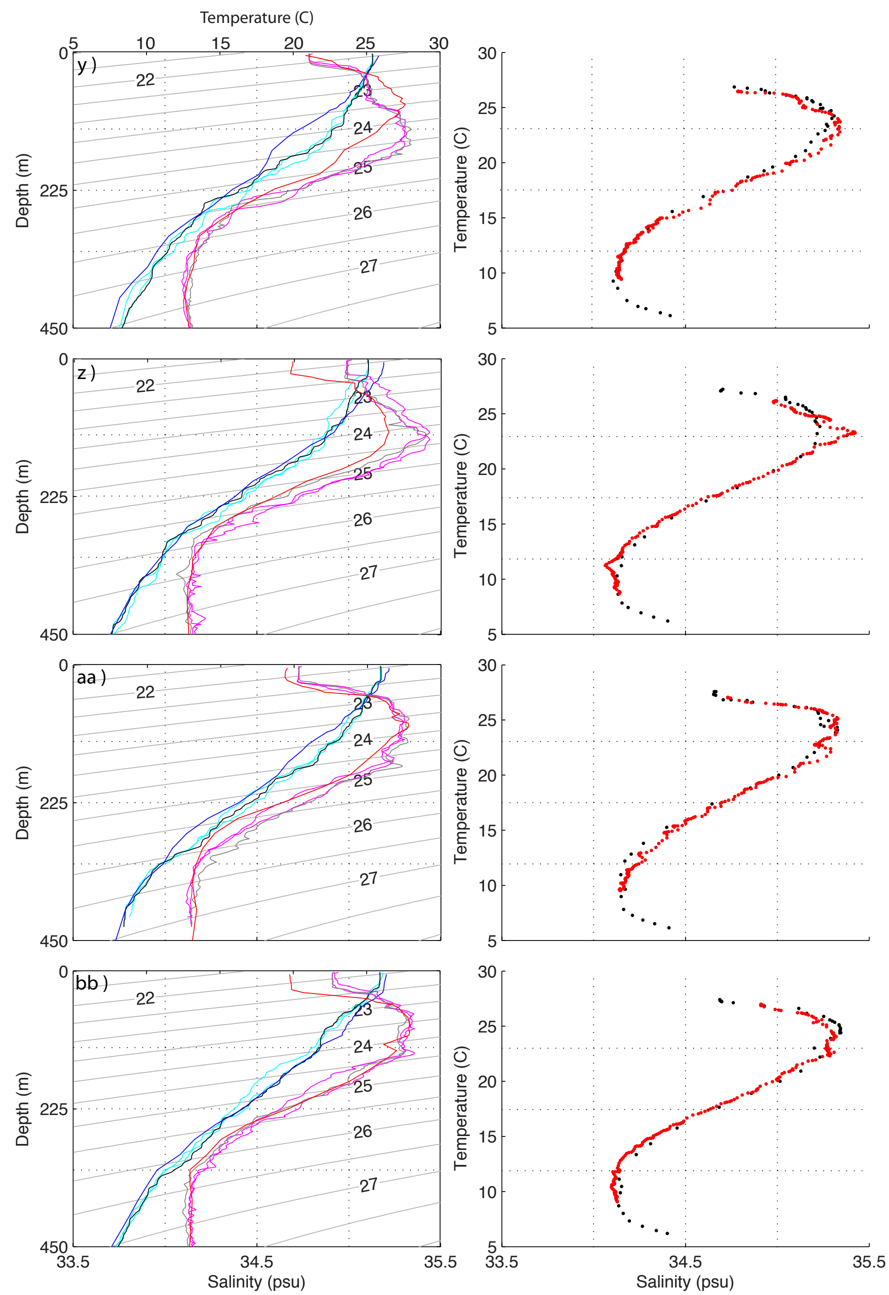

FIGURE A.13: Mission 5 continued

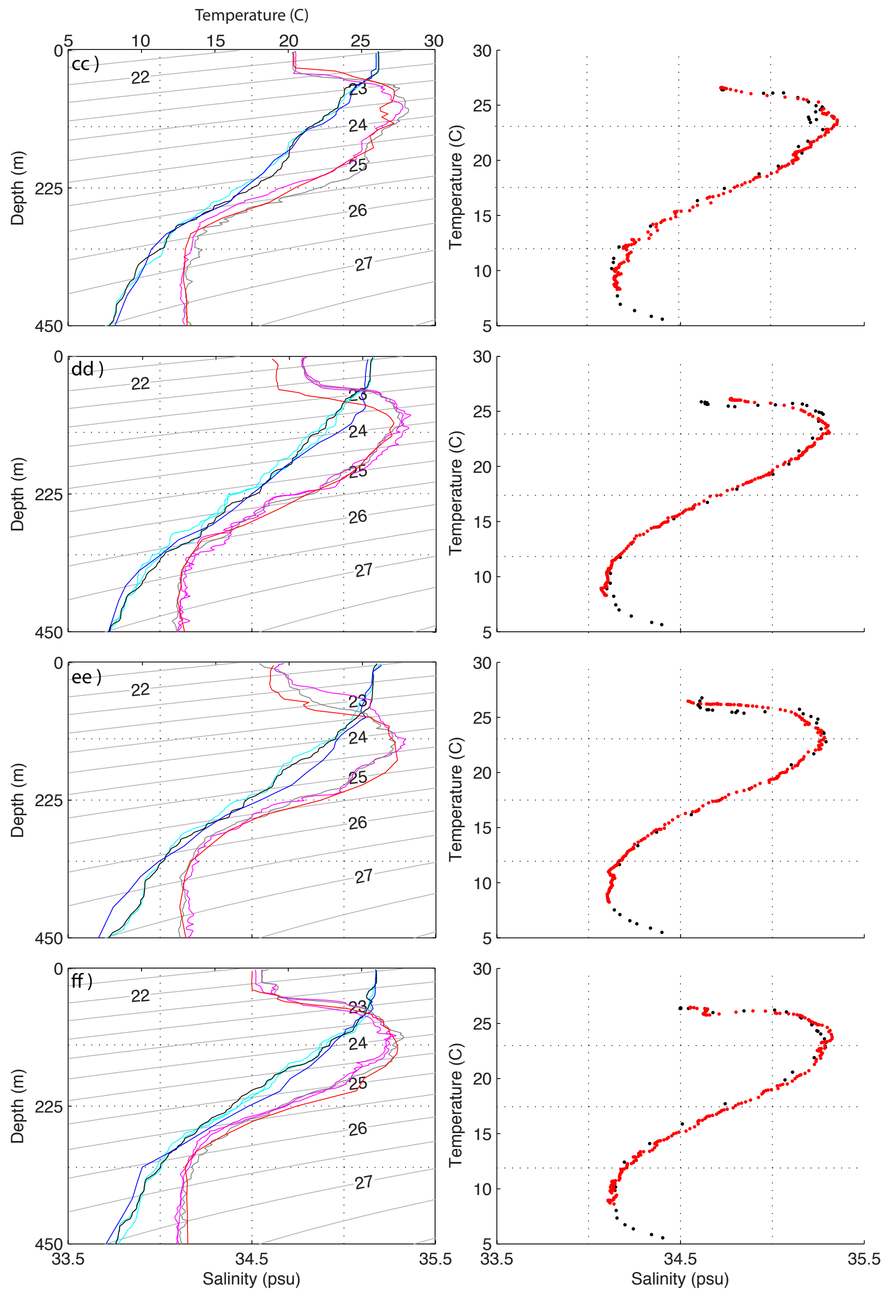

FIGURE A.14: Mission 5 continued

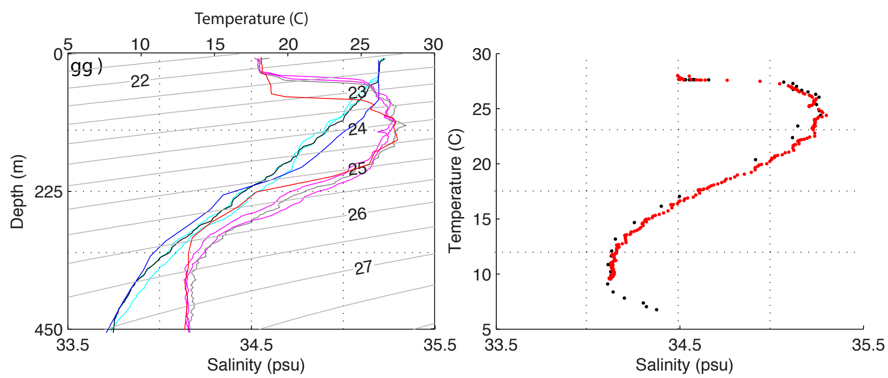

FIGURE A.15: Mission 5 continued

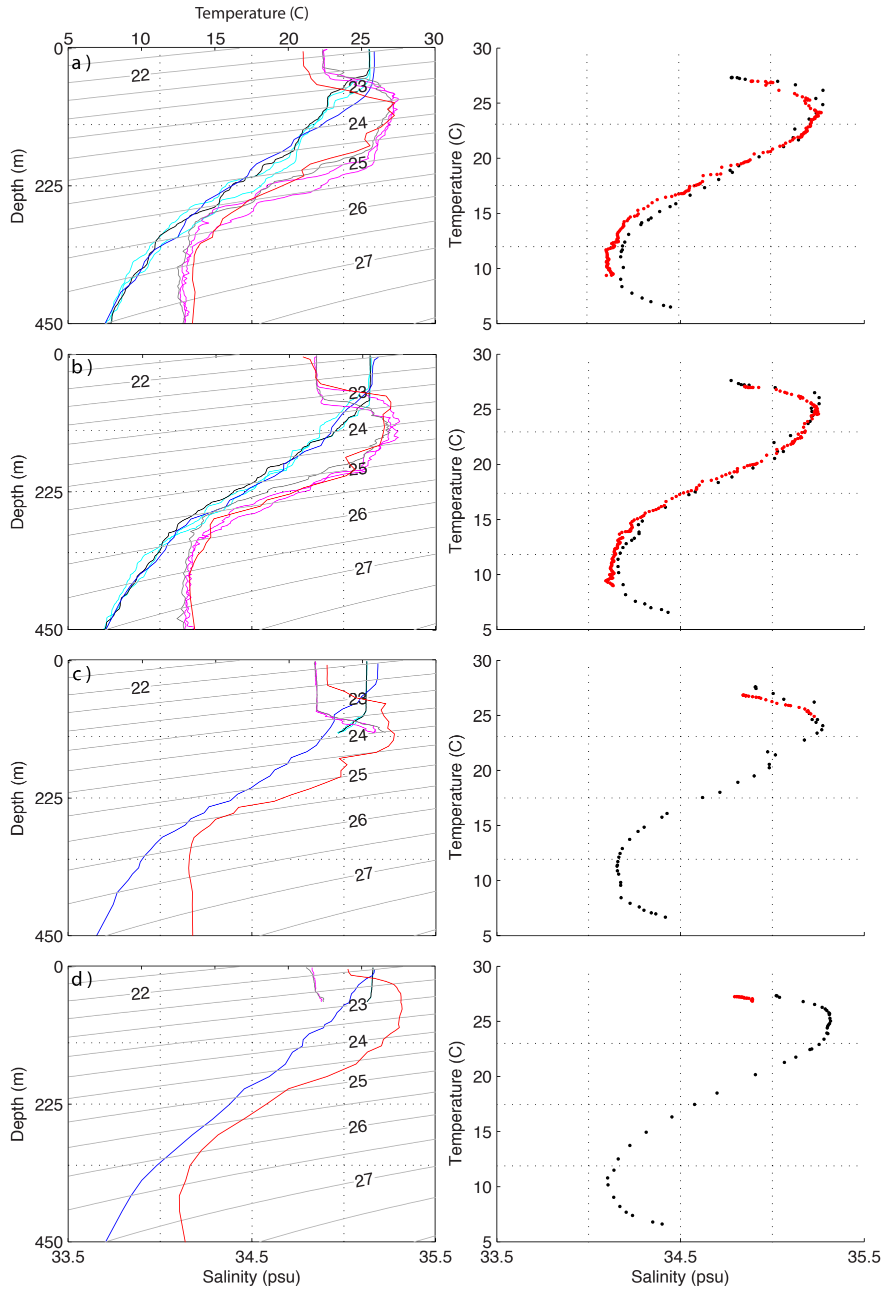

FIGURE A.16: Mission 6

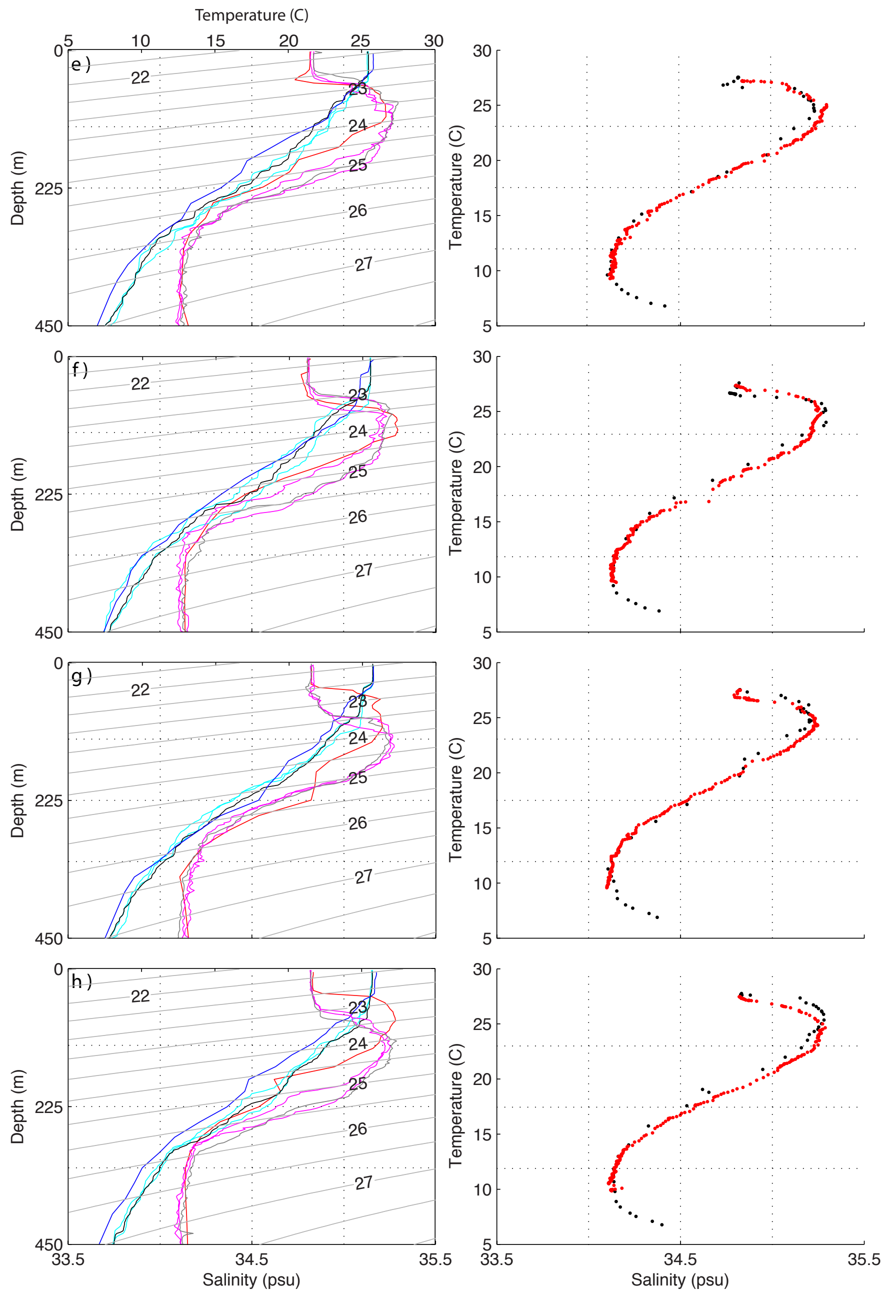

FIGURE A.17: Mission 6 continued

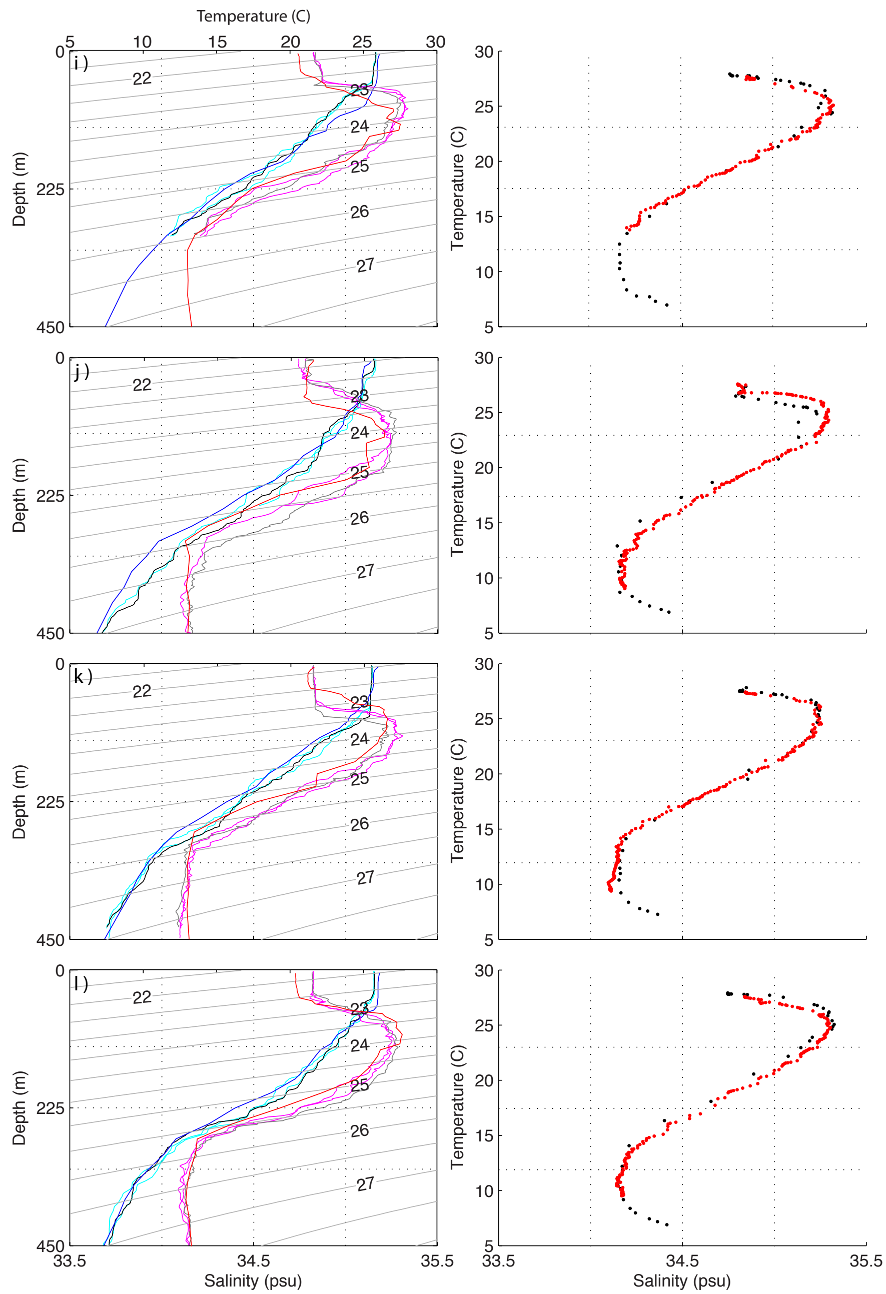

FIGURE A.18: Mission 6 continued

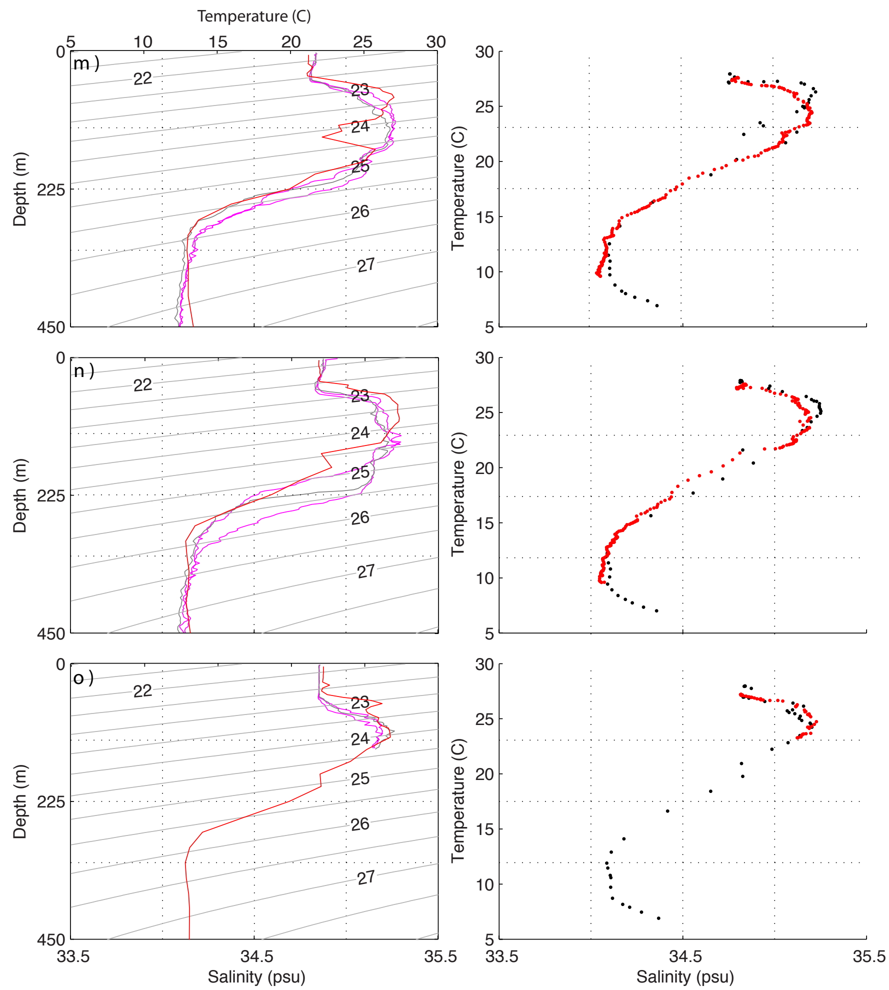

FIGURE A.19: Mission 6 continued

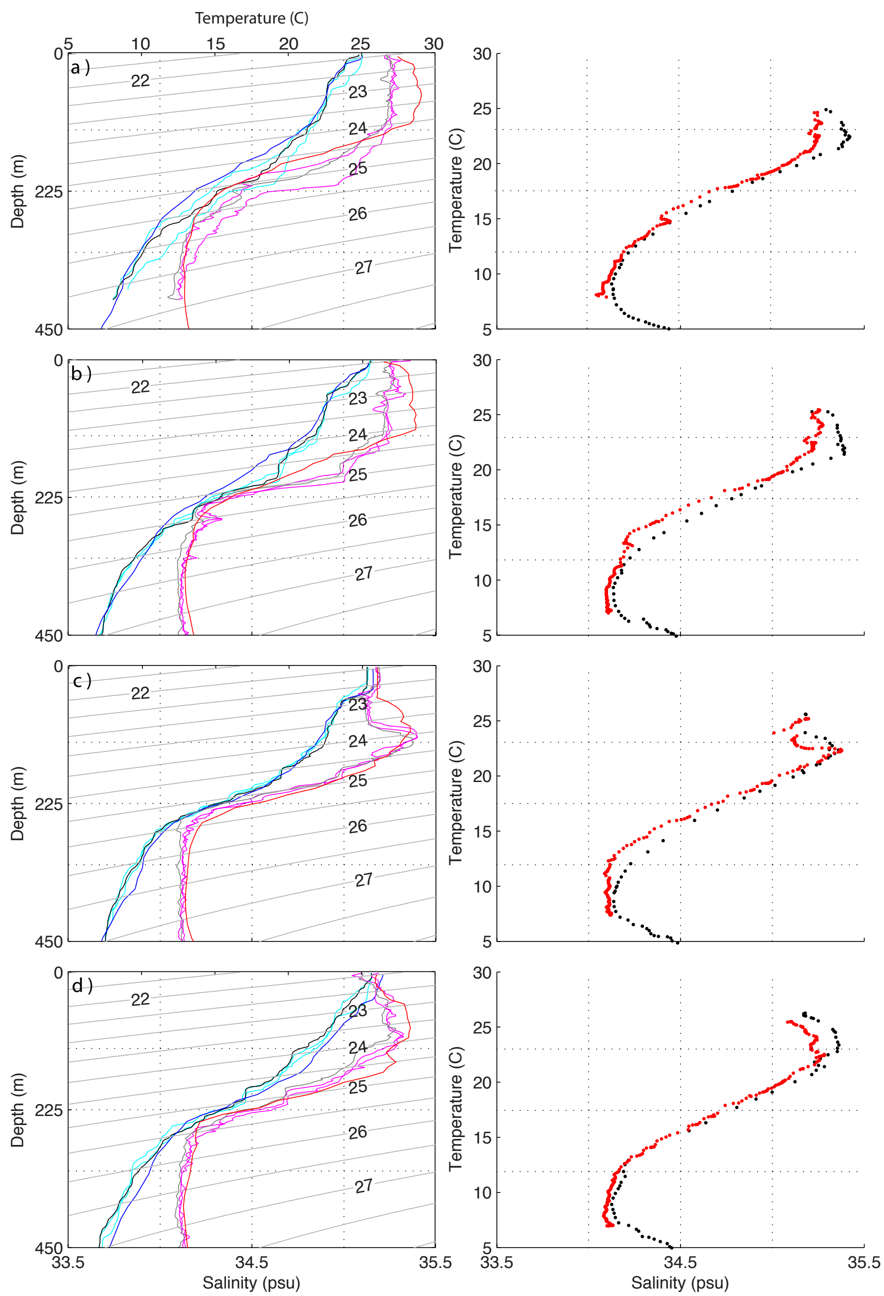

FIGURE A.20: Mission 7

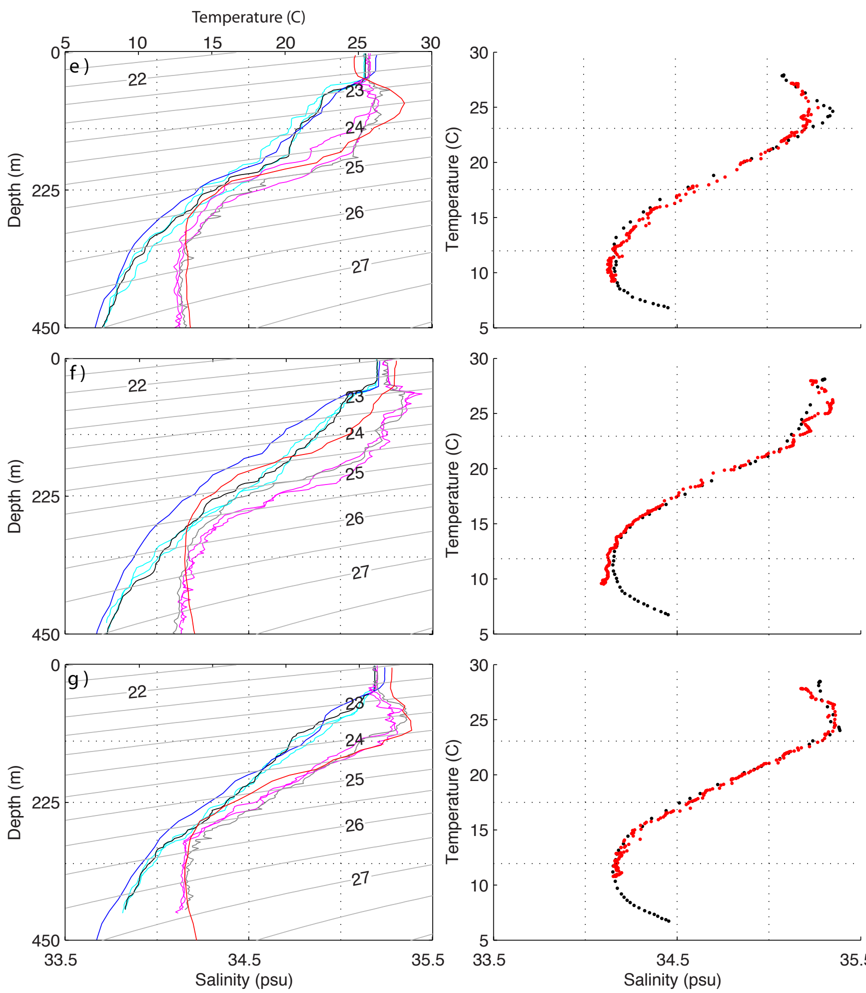

FIGURE A.21: Mission 7 continued

Appendix B

Argo profiles

Table B.1: All Argo profiles in the Seaglider region from 2008 through 2013

Float Number	Date	Latitude	Longitude
5900584	09-May-2008 14:27:17	19.088	-158.444
5900584	19-May-2008 23:13:26	19.5	-158.146
5900584	30-May-2008 11:46:15	19.733	-157.914
5900584	10-Jun-2008 00:39:22	19.62	-157.711
5900584	20-Jun-2008 14:23:02	19.535	-157.664
5900584	01-Jul-2008 06:43:30	19.482	-157.561
5900584	11-Jul-2008 15:55:31	19.621	-157.557
5900584	22-Jul-2008 04:37:05	19.992	-157.536
5900584	01-Aug-2008 18:32:16	20.305	-157.684
5900584	12-Aug-2008 07:13:55	20.429	-157.568
5900584	22-Aug-2008 19:36:38	20.165	-157.15
5900584	18-Oct-2009 12:00:29	19.073	-158.854
5900584	08-Jul-2010 01:10:39	19.028	-158.018
5900584	31-Oct-2010 23:21:06	19.8	-158.591
5900584	11-Nov-2010 04:57:57	19.407	-157.802
5900947	28-Nov-2010 09:49:41	19.561	-158.735
5900947	09-Dec-2010 01:49:36	19.402	-158.328
5900947	19-Dec-2010 11:50:44	19.356	-157.986
5900947	30-Dec-2010 00:59:47	19.402	-157.401
5900947	13-Mar-2011 19:47:28	19.475	-157.1
5900947	24-Mar-2011 08:54:18	19.679	-157.455
5900947	03-Apr-2011 19:31:10	19.888	-157.8
5900947	14-Apr-2011 11:09:39	20.102	-157.76
5900947	24-Apr-2011 23:55:35	20.301	-157.786
5900947	05-May-2011 12:55:48	20.36	-157.747
5900947	16-May-2011 01:51:56	20.363	-157.732

Continued on next page.

Table B.1 – *Continued from previous page*

Float Number	Date	Latitude	Longitude
5900947	26-May-2011 14:14:40	20.337	-157.768
5900947	06-Jun-2011 03:55:15	20.503	-157.872
5900947	16-Jun-2011 16:51:29	20.768	-158.06
5900947	27-Jun-2011 05:50:39	20.888	-158.292
5900947	07-Jul-2011 20:15:56	21.051	-158.673
5900947	29-Aug-2011 11:54:45	21.164	-158.953
5900947	09-Sep-2011 00:49:51	20.763	-158.891
5900947	19-Sep-2011 13:58:03	20.579	-158.838
5900947	14-Feb-2012 03:48:00	21.189	-158.711
5900947	24-Feb-2012 16:44:20	20.922	-158.857
5900947	07-Mar-2012 03:57:11	20.815	-158.852
5900947	17-Mar-2012 20:32:54	20.832	-158.802
5900947	28-Mar-2012 07:45:47	20.734	-158.891
5900947	07-Apr-2012 20:52:40	20.663	-158.788
5900947	18-Apr-2012 09:48:46	20.515	-158.905
5900960	17-Mar-2010 08:44:10	19.686	-158.951
5900960	24-Mar-2010 09:13:10	19.56	-158.565
5900960	31-Mar-2010 09:43:40	19.198	-158.193
2900828	22-Nov-2008 03:27:27	19.511	-158.992
2900828	26-Nov-2008 03:07:05	19.345	-158.739
2900828	30-Nov-2008 03:35:34	19.165	-158.189
2900828	04-Dec-2008 03:12:44	19.076	-157.636
2900828	08-Dec-2008 03:44:40	19.198	-157.181
2900828	01-Jan-2009 02:54:39	20.325	-157.082
2900828	05-Jan-2009 03:38:48	20.171	-157.55
2900828	09-Jan-2009 02:57:58	19.565	-157.656
2900828	13-Jan-2009 03:44:46	19.386	-157.223
2900828	29-Jan-2009 03:00:53	20.192	-157.007
2900828	02-Feb-2009 03:04:11	20.195	-157.712
2900828	06-Feb-2009 03:11:55	20.068	-158.256
2900828	10-Feb-2009 03:13:32	19.967	-158.592
2900828	14-Feb-2009 03:22:23	19.8	-158.944
2900828	26-Jul-2010 02:51:48	19.545	-158.991
2900828	30-Jul-2010 02:53:37	19.684	-158.984
2900828	08-Sep-2010 02:53:22	20.375	-158.885
2900828	12-Sep-2010 02:51:42	20.559	-158.638
2900828	16-Sep-2010 02:50:43	20.393	-158.782
2900829	01-Aug-2008 10:51:07	19.659	-158.42
2900829	05-Aug-2008 11:47:22	20.114	-158.716
2900831	03-Aug-2008 02:56:21	20.537	-158.127
2900831	07-Aug-2008 02:58:32	20.678	-158.598

Continued on next page.

Table B.1 – *Continued from previous page*

Float Number	Date	Latitude	Longitude
2900831	11-Aug-2008 02:58:58	20.79	-158.904
5900063	01-Oct-2011 01:19:09	20.522	-157.008
5900063	05-Oct-2011 01:16:12	20.587	-157.016
5900063	09-Oct-2011 01:23:13	20.537	-157.056
5900063	25-Oct-2011 02:30:22	20.105	-157.043
5900063	29-Oct-2011 02:22:49	20.122	-157.063
5900063	02-Nov-2011 02:28:18	20.213	-157.265
5900063	06-Nov-2011 02:18:27	20.281	-157.557
5900063	10-Nov-2011 02:21:37	20.254	-157.834
5900063	14-Nov-2011 02:26:20	20.129	-158.062
5900063	18-Nov-2011 02:27:13	19.925	-158.249
5900063	22-Nov-2011 02:27:20	19.894	-158.519
5900063	26-Nov-2011 02:26:41	19.934	-158.441
5900063	30-Nov-2011 02:29:51	19.982	-158.346
5900063	04-Dec-2011 02:23:50	20.019	-158.241
5900063	08-Dec-2011 02:31:37	20.116	-158.146
5900063	12-Dec-2011 02:27:54	20.241	-157.926
5900063	16-Dec-2011 02:24:57	20.348	-157.778
5900063	20-Dec-2011 02:25:04	20.379	-157.717
5900063	24-Dec-2011 11:30:16	20.431	-157.472
5900063	28-Dec-2011 02:27:35	20.498	-157.263
5900063	01-Jan-2012 02:30:00	20.518	-157.189
5900063	05-Jan-2012 01:19:35	20.525	-157.09
5900063	17-Jan-2012 02:18:11	20.499	-157.144
5900063	21-Jan-2012 02:25:58	20.519	-157.169
5900063	25-Jan-2012 02:35:17	20.664	-157.166
5900063	29-Jan-2012 02:24:40	20.769	-157.181
5900063	02-Feb-2012 02:25:32	20.831	-157.163
5900063	10-Feb-2012 01:49:44	20.797	-157.101
5900063	14-Feb-2012 01:39:53	20.804	-157.111
5900063	18-Feb-2012 01:20:49	20.759	-157.063
5900063	22-Feb-2012 00:35:42	20.797	-157.027
5900063	26-Feb-2012 01:22:35	20.798	-157.064
5900063	02-Mar-2012 00:25:12	20.88	-157.144
5900063	06-Mar-2012 02:45:37	20.949	-157.314
5900063	10-Mar-2012 02:21:58	20.947	-157.352
5900063	14-Mar-2012 00:13:16	21.167	-157.47
5900063	18-Mar-2012 01:14:43	21.219	-157.541
5900063	22-Mar-2012 01:21:44	21.331	-157.522
5900064	17-Oct-2011 08:28:59	19.067	-158.574
5900064	21-Oct-2011 08:27:41	19.199	-158.384

Continued on next page.

Table B.1 – *Continued from previous page*

Float Number	Date	Latitude	Longitude
5900064	25-Oct-2011 08:27:48	19.152	-158.112
5900064	14-Nov-2011 08:29:04	19.154	-157.461
5900064	18-Nov-2011 08:35:29	19.56	-157.229
5900064	26-Mar-2012 08:28:36	20.044	-157.202
5900064	30-Mar-2012 08:23:08	19.856	-157.285
5900064	03-Apr-2012 08:35:09	19.665	-157.339
5900064	07-Apr-2012 08:38:46	19.388	-157.174
5900064	11-Apr-2012 08:33:16	19.156	-157.001
5900064	05-May-2012 08:32:34	20.417	-157.247
5900064	09-May-2012 08:33:22	20.433	-157.546
5900064	13-May-2012 18:33:22	20.198	-157.924
5900064	17-May-2012 08:29:24	19.883	-158.046
5900064	21-May-2012 08:35:49	19.758	-157.934
5900064	25-May-2012 08:40:07	19.896	-157.81
5900064	29-May-2012 08:30:26	20.243	-157.86
5900064	02-Jun-2012 08:37:33	20.492	-158.051
5900064	06-Jun-2012 08:32:46	20.623	-158.257
5900064	10-Jun-2012 08:41:59	20.779	-158.479
5900064	14-Jun-2012 08:44:11	20.835	-158.711
5900064	18-Jun-2012 08:36:36	20.793	-158.877
5900064	22-Jun-2012 08:36:01	20.805	-158.96
5900064	01-Nov-2012 08:42:29	19.225	-158.905
5900064	05-Nov-2012 08:42:36	19.013	-158.849
5900064	15-Dec-2012 08:40:12	19.123	-158.903
5900064	19-Dec-2012 08:40:19	19.2	-158.924
5900065	02-Sep-2011 22:10:52	20.207	-157.516
5900065	06-Sep-2011 22:09:40	20.383	-157.807
5900065	10-Sep-2011 22:14:42	20.33	-158.076
5900065	14-Sep-2011 22:04:19	20.122	-158.175
5900065	18-Sep-2011 22:12:50	20.09	-158.043
5900065	22-Sep-2011 22:07:21	20.212	-157.878
5900065	26-Sep-2011 22:11:40	20.463	-157.813
5900065	30-Sep-2011 22:11:47	20.644	-158.003
5900065	04-Oct-2011 22:11:11	20.788	-158.23
5900065	08-Oct-2011 22:08:29	20.778	-158.418
5900065	12-Oct-2011 22:16:19	20.892	-158.664
5900065	16-Oct-2011 22:07:20	20.726	-158.679
5900065	20-Oct-2011 22:08:51	20.621	-158.687
5900065	24-Oct-2011 22:22:16	20.506	-158.682
5900065	28-Oct-2011 22:20:59	20.487	-158.714
5900065	01-Nov-2011 22:17:36	20.51	-158.801

Continued on next page.

Table B.1 – *Continued from previous page*

Float Number	Date	Latitude	Longitude
5900065	05-Nov-2011 22:17:00	20.569	-158.841
5900065	09-Nov-2011 22:09:25	20.57	-158.953
5901041	04-Apr-2012 03:38:44	19.807	-158.887
5901041	14-Apr-2012 21:34:20	19.698	-158.563
5901041	25-Apr-2012 15:25:27	19.535	-158.311
5901041	06-May-2012 20:00:06	19.319	-158.096
5901041	17-May-2012 03:27:59	19.306	-157.937
5901041	27-May-2012 21:30:39	19.522	-157.716
5901041	07-Jun-2012 15:34:07	19.745	-157.666
5901041	18-Jun-2012 09:25:39	19.827	-157.681
5901041	29-Jun-2012 03:35:22	19.776	-157.648
5901041	09-Jul-2012 21:38:28	19.821	-157.846
5901041	20-Jul-2012 15:23:21	19.851	-158.086
5901041	31-Jul-2012 09:35:11	19.719	-157.824
5901041	11-Aug-2012 03:33:30	19.756	-157.602
5901041	21-Aug-2012 21:36:51	19.855	-157.477
5901041	01-Sep-2012 15:33:48	19.753	-157.28
5901041	03-Oct-2012 21:23:15	19.899	-157.631
5901041	14-Oct-2012 15:25:38	19.235	-157.766
5901041	25-Oct-2012 08:43:38	19.099	-157.695
5901041	05-Nov-2012 03:22:46	19.486	-157.969
5901041	15-Nov-2012 21:29:15	19.719	-158.468
5901041	26-Nov-2012 15:28:21	19.844	-158.736
5901041	18-Dec-2012 03:43:06	20.412	-158.518
5901041	28-Dec-2012 21:35:00	20.556	-158.342
5901041	08-Jan-2013 15:38:10	20.32	-158.414
5901041	19-Jan-2013 09:24:29	20.334	-158.537
5901041	30-Jan-2013 03:38:21	20.423	-158.636
5901041	09-Feb-2013 21:31:03	20.337	-158.827
5901041	20-Feb-2013 14:19:07	20.517	-158.719
5901041	03-Mar-2013 09:17:01	20.808	-158.703
5901041	14-Mar-2013 03:38:03	20.677	-158.684
5901041	24-Mar-2013 21:39:55	20.383	-158.883
5901041	15-Apr-2013 09:43:46	19.807	-158.975
5901041	26-Apr-2013 03:25:55	20.257	-158.784
5901041	06-May-2013 21:36:04	20.585	-158.68
5901041	17-May-2013 15:39:31	20.643	-158.593
5901041	28-May-2013 08:41:37	20.489	-158.636
5901041	08-Jun-2013 03:48:31	20.219	-158.841
5901041	29-Jun-2013 12:44:59	19.954	-158.857
5901041	10-Jul-2013 09:38:14	20.359	-158.792

Continued on next page.

Table B.1 – *Continued from previous page*

Float Number	Date	Latitude	Longitude
5901041	04-Oct-2013 09:33:59	19.807	-158.984
5901041	15-Oct-2013 00:01:58	19.931	-158.42
5901041	25-Oct-2013 21:47:51	20.369	-158.046
5901041	05-Nov-2013 12:08:16	20.434	-157.57
5901041	16-Nov-2013 09:40:41	20.463	-157.378
5901041	26-Nov-2013 23:57:07	20.687	-157.367
5901041	07-Dec-2013 21:33:37	20.809	-157.344
5901041	18-Dec-2013 14:27:38	20.888	-157.363
5901041	29-Dec-2013 08:39:57	20.917	-157.357
5901469	11-Dec-2008 08:04:07	20.023	-157.136
5901469	21-Dec-2008 15:01:04	19.768	-157.509
5901469	31-Dec-2008 21:40:10	19.875	-157.906
5901469	11-Jan-2009 04:03:53	19.54	-158.034
5901469	21-Jan-2009 11:00:47	19.715	-158.313
5901469	31-Jan-2009 16:58:02	19.354	-158.611
5901469	10-Feb-2009 23:26:04	19.705	-158.765
5902155	22-Mar-2011 00:13:36	20.28	-158.355
5902155	26-Mar-2011 00:09:32	20.342	-158.329
5902155	30-Mar-2011 00:15:31	20.478	-158.422
5902155	03-Apr-2011 00:10:30	20.564	-158.596
5902155	07-Apr-2011 00:18:40	20.753	-158.681
5902155	11-Apr-2011 00:07:47	20.726	-158.85
5902156	21-Mar-2011 20:31:12	20.763	-158.379
5902156	25-Mar-2011 20:39:31	20.824	-158.616
5902156	29-Mar-2011 20:35:48	20.926	-158.868
5902157	21-Mar-2011 12:46:06	20.825	-157.587
5902157	25-Mar-2011 03:10:47	21.045	-157.619
5902157	29-Mar-2011 15:55:45	21.144	-157.654
5902157	02-Apr-2011 04:03:05	21.204	-157.624
5902157	06-Apr-2011 04:06:08	21.199	-157.758
5902157	10-Apr-2011 16:07:06	21.157	-157.848
5902157	14-Apr-2011 03:47:16	21.106	-157.998
5902157	18-Apr-2011 03:59:08	21.124	-157.95
5902157	22-Apr-2011 03:54:07	21.127	-157.945
5902157	26-Apr-2011 04:00:06	21.05	-157.99
5902157	30-Apr-2011 05:12:03	21.124	-158.133
5902157	04-May-2011 05:20:14	21.19	-158.177
5902157	08-May-2011 05:09:22	21.158	-158.229
5902157	12-May-2011 05:15:20	21.031	-158.063
5902157	16-May-2011 03:53:19	21.01	-157.909
5902157	20-May-2011 03:47:34	21.03	-157.844

Continued on next page.

Table B.1 – *Continued from previous page*

Float Number	Date	Latitude	Longitude
5902157	24-May-2011 03:53:32	21.046	-157.934
5902157	28-May-2011 05:14:19	21.08	-158.116
5902157	01-Jun-2011 05:18:50	21.054	-158.279
5902157	05-Jun-2011 05:21:08	20.94	-158.546
5902157	09-Jun-2011 05:23:27	20.68	-158.689
5902157	13-Jun-2011 05:10:22	20.676	-158.55
5902157	17-Jun-2011 05:22:55	20.773	-158.623
5902157	21-Jun-2011 05:20:50	20.704	-158.691
5902157	25-Jun-2011 05:25:21	20.816	-158.879
5902157	29-Jun-2011 05:16:40	20.703	-158.995
5902158	22-Mar-2011 13:36:42	20.096	-158.025
5902158	26-Mar-2011 00:24:37	19.867	-158.214
5902158	30-Mar-2011 04:51:31	19.76	-158.29
5902158	03-Apr-2011 15:35:39	19.734	-158.283
5902158	07-Apr-2011 04:58:38	19.77	-158.265
5902158	11-Apr-2011 04:51:05	19.935	-158.2
5902158	15-Apr-2011 04:53:30	20.15	-158.196
5902158	19-Apr-2011 04:56:41	20.324	-158.219
5902158	23-Apr-2011 04:43:47	20.495	-158.313
5902158	27-Apr-2011 04:49:16	20.576	-158.262
5902158	01-May-2011 04:55:30	20.664	-158.205
5902158	05-May-2011 04:44:07	20.699	-158.085
5902158	09-May-2011 04:46:32	20.67	-158.004
5902158	13-May-2011 04:42:03	20.588	-157.768
5902158	17-May-2011 14:32:29	20.531	-157.629
5902158	21-May-2011 04:53:01	20.526	-157.467
5902158	25-May-2011 04:47:46	20.609	-157.328
5902158	29-May-2011 04:54:01	20.608	-157.17
5902158	02-Jun-2011 03:30:34	20.51	-157.095
5902158	06-Jun-2011 04:55:47	20.404	-157.248
5902158	10-Jun-2011 04:59:42	20.503	-157.329
5902158	14-Jun-2011 04:50:37	20.492	-157.491
5902158	18-Jun-2011 14:16:32	20.571	-157.602
5902158	22-Jun-2011 04:57:46	20.619	-157.717
5902158	26-Jun-2011 04:54:03	20.764	-157.958
5902158	30-Jun-2011 04:54:56	20.78	-158.171
5902158	04-Jul-2011 04:46:37	20.887	-158.416
5902158	08-Jul-2011 04:52:05	21.04	-158.766
5902159	29-Oct-2011 10:08:04	20.571	-157.032
5902159	02-Nov-2011 09:57:55	20.606	-157.09
5902159	06-Nov-2011 11:12:07	20.726	-157.17

Continued on next page.

Table B.1 – *Continued from previous page*

Float Number	Date	Latitude	Longitude
5902159	10-Nov-2011 11:04:10	20.63	-157.195
5902159	14-Nov-2011 11:07:56	20.775	-157.297
5902159	18-Nov-2011 11:03:39	20.718	-157.301
5902159	22-Nov-2011 11:12:34	20.81	-157.398
5902159	26-Nov-2011 11:15:36	20.764	-157.659
5902159	30-Nov-2011 11:04:43	20.758	-157.973
5902159	04-Dec-2011 11:12:54	20.651	-158.12
5902159	08-Dec-2011 11:01:17	20.528	-158.107
5902159	12-Dec-2011 11:07:15	20.557	-158.042
5902159	16-Dec-2011 11:05:10	20.699	-157.922
5902159	20-Dec-2011 11:04:33	20.694	-157.877
5902159	24-Dec-2011 10:57:19	20.697	-157.971
5902159	28-Dec-2011 11:05:30	20.611	-158.13
5902159	01-Jan-2012 10:52:25	20.338	-158.221
5902159	05-Jan-2012 11:09:24	19.864	-158.233
5902159	09-Jan-2012 11:03:38	19.278	-158.02
5902159	07-Apr-2012 11:15:38	19.345	-158.796
5902159	11-Apr-2012 11:09:08	19.193	-158.62
5902159	02-Jun-2012 11:14:59	19.064	-157.581
5902159	06-Jun-2012 11:02:38	19.254	-157.335
5902159	03-Dec-2012 11:16:28	20.059	-157.114
5902159	15-Dec-2012 11:19:44	19.343	-157.396
5902159	19-Dec-2012 11:08:50	19.279	-157.343
5902159	23-Dec-2012 11:14:49	19.395	-157.246
5902159	27-Dec-2012 11:20:04	19.492	-157.284
5902159	31-Dec-2012 11:22:23	19.659	-157.232
5902159	04-Jan-2013 11:22:29	19.951	-157.447
5902159	08-Jan-2013 11:24:47	19.971	-157.954
5902159	12-Jan-2013 11:22:43	19.71	-158.259
5902159	16-Jan-2013 11:23:33	19.41	-158.47
5902159	18-Dec-2013 11:29:16	20.35	-158.99
5902159	22-Dec-2013 11:27:11	20.411	-158.873
5902159	26-Dec-2013 11:28:45	20.456	-158.838
5902159	30-Dec-2013 11:33:16	20.415	-158.844
5902160	25-Oct-2011 05:17:01	19.402	-158.859
5902160	29-Oct-2011 05:17:09	19.319	-158.556
5902160	02-Nov-2011 05:20:19	19.064	-158.326
5902160	18-Nov-2011 05:20:46	19.284	-157.538
5902160	22-Nov-2011 05:21:39	19.57	-157.322
5902160	26-Nov-2011 05:34:02	19.895	-157.112
5903465	26-Aug-2013 06:27:55	19.028	-158.98

Continued on next page.

Table B.1 – *Continued from previous page*

Float Number	Date	Latitude	Longitude
5903465	20-Nov-2013 02:31:20	19.085	-158.938
5903465	01-Dec-2013 00:04:53	19.03	-158.652
5904201	10-Oct-2013 19:51:03	20.622	-157.993
5904201	14-Oct-2013 19:30:07	20.721	-158.033
5904201	18-Oct-2013 19:37:34	20.766	-158.077
5904201	22-Oct-2013 19:39:09	20.743	-157.976
5904201	26-Oct-2013 19:33:22	20.709	-157.781
5904201	30-Oct-2013 19:40:06	20.652	-157.533
5904201	03-Nov-2013 19:32:09	20.565	-157.424
5904201	07-Nov-2013 19:33:44	20.443	-157.141
5904201	11-Nov-2013 18:15:22	20.5	-157.108
5904201	15-Nov-2013 18:47:00	20.545	-157.13
5904201	19-Nov-2013 19:37:44	20.615	-157.144
5904201	23-Nov-2013 19:37:06	20.545	-157.197
5904201	27-Nov-2013 19:43:49	20.784	-157.19
5904201	01-Dec-2013 18:47:27	20.903	-157.188
5904201	05-Dec-2013 19:37:27	20.94	-157.256
5904201	09-Dec-2013 19:30:57	20.958	-157.356
5904201	13-Dec-2013 17:54:15	20.968	-157.483
5904201	17-Dec-2013 17:26:30	21.001	-157.399
5904201	21-Dec-2013 17:00:12	20.995	-157.474
5904201	25-Dec-2013 16:58:51	20.983	-157.569
5904201	29-Dec-2013 16:58:15	20.908	-157.711
5904203	09-Oct-2013 16:32:46	19.228	-157.48
5904203	13-Oct-2013 16:20:59	19.293	-157.26
5904203	17-Oct-2013 16:31:37	19.016	-157.028
5904204	03-Dec-2013 15:18:05	20.385	-158.956
5904204	07-Dec-2013 15:22:04	20.508	-158.858
5904204	11-Dec-2013 15:21:27	20.612	-158.767
5904204	15-Dec-2013 15:26:59	20.691	-158.748
5904204	19-Dec-2013 15:16:23	20.725	-158.716
5904204	23-Dec-2013 15:19:36	20.759	-158.725
5904204	27-Dec-2013 15:16:42	20.8	-158.695
5904207	10-Oct-2013 18:03:33	20.072	-157.466
5904207	14-Oct-2013 18:17:40	20.105	-157.345
5904207	18-Oct-2013 18:21:17	20.081	-157.264
5904207	22-Oct-2013 18:25:38	20	-157.117
5904207	26-Oct-2013 18:23:39	19.858	-157.054
5904207	30-Oct-2013 18:20:59	19.703	-157.041
5904207	07-Nov-2013 18:31:44	19.413	-157.015
5904207	15-Nov-2013 18:24:17	19.067	-157.004

Continued on next page.

Table B.1 – *Continued from previous page*

Float Number	Date	Latitude	Longitude
5904207	13-Dec-2013 18:27:57	19.097	-157.097
5904207	17-Dec-2013 18:25:18	19.056	-157.199
5904207	21-Dec-2013 18:21:54	19.096	-157.226
5904329	10-Oct-2013 20:16:07	19.634	-158.046
5904329	14-Oct-2013 20:03:09	19.835	-158.055
5904329	18-Oct-2013 20:01:46	19.836	-157.967
5904329	22-Oct-2013 20:05:00	19.926	-157.844
5904329	26-Oct-2013 19:56:43	19.949	-157.823
5904329	30-Oct-2013 19:54:38	19.946	-157.782
5904329	03-Nov-2013 19:59:25	19.927	-157.701
5904329	07-Nov-2013 20:01:51	19.798	-157.704
5904329	11-Nov-2013 20:08:09	19.622	-157.581
5904329	15-Nov-2013 19:59:06	19.388	-157.514
5904329	19-Nov-2013 20:01:33	19.251	-157.481
5904329	23-Nov-2013 19:58:39	19.081	-157.491

Bibliography

Alford, M.H.; Gregg, M.C., and Merrifield, M.A. Structure, propagation, and mixing of energetic baroclinic tides in Mamala Bay, Oahu, Hawaii. *J. Phys. Oceanography*, 36:997–1018, 2006.

Antonov, J.I.; Seidov, D.; Locarnini, R.A.; Mishonov, A.V.; Garcia, H.E.; Baranova, O.K.; Zweng, M.M., and Johnson, D.R. *World Ocean Atlas 2009, Volume 2: Salinity.* U.S. Government Printing Office, 2010.

Aoki, S. and Imawaki, S. Eddy activities of the surface layer in the western North Pacific detected by satellite altimeter and radiometer. *J. Oceanogr.*, 52:457–474, 1996.

Berfloff, P.S.; McWilliams, J.C., and Bracco, A. Material transport in oceanic gyres. Part I: Phenomenology. *J. Phys. Oceanography*, 32:764–796, 2002.

Bernstein, R.L. and White, W.B. Time and length scales of baroclinic eddies in the Central North Pacific Ocean. *J. Phys. Oceanography*, 4:613–624, October 1974.

Bingham, F.M. Evidence for the existence of a North Hawaiian Ridge Current. *J. Phys. Oceanography*, 1997.

Bleck, R. and Benjamin, S. Regional weather prediction with a model combining terrain-following and isentropic coordinates. Part I:Model description. *Mon. Wea. Rev.*, 121:1770–1785, 1993.

Calil, H.R.; Richards, K.; Jia, Y., and Bridigare, R.R. Eddy activity in the lee of the Hawaiian Islands. *Deep-Sea Research Part II*, 2007.

Carmack, E.C. and Foster, T.D. Water masses and circulation in the Weddell Sea. *Polar Oceans*, pages 151–165, 1977.

Carstoiu, I. Vorticity and deformation in fluid mechanics. *J. Rational Mech.*, 3: 691–717, 1954.

Carter, G.S.; Merrifield, M.A.; Becker, J.M.; Katsumata, K.; Gregg, M.C.; Luther, D.S.; Levine, M.D.; Boyd, T.J., and Firing, Y.L. Energetics of m2 barotropic-to-baroclinic tidal conversion at the hawaiian islands. *J. Phys. Oceanography*, 38(10):2205–2223, 2008.

Chavanne, C.; Flament, P.; Lumpkin, R.; Dousset, B., and Bentamy, A. Scatterometer observations of wind variations induced by oceanic islands: Implications for wind-driven ocean circulation. *Canadian Journal of Remote Sensing*, 28:466–474, 2002.

Chelton, D.B.; Schlax, M.G.; Samelson, R.M., and de Szoeke, R.A. Global observations of large oceanic eddies. *Geophys. Res. Lett.*, 34(15), August 2007.

Commision, Intergovernmental Oceanographic. *IOC, SCOR and IAPSO, 2010: The international thermodynamic equation of seawater - 2010: Calculation and use of thermodynamic properties.* UNESCO, 56 edition, 2010.

Cresswell, G.R. The coalescences of two East Australian Current warm-core eddies. *Science*, 215:161–164, 1982.

Cushman-Roisin, B. *Introduction to Geophysical Fluid Dynamics*. Prentice Hall, New Jersey, 1994.

Davis, R.E.; Eriksen, C.E., and Jones, C.P. *Autonomous buoyancy-Driven Underwater Gliders*, volume Technology and applications of autonomous underwater vehicles. Taylor & Francis, London, 2003.

Davis, R.E.; Ohman, M.D.; Rudnick, D.L., and Sherman, J.T. Glider surveillance of physics and biology in the Southern California Current System. *Limnol. Oceanogr.*, 53(5):2151–2168, 2008.

Dickey, T.D.; Nencioli, F.; Kuwahara, V.S.; Leonard, C.L.; Black, W.; Bridigare, R.R.; Rii, Y.M., and Zhang, Q. Physical and bio-optical observations of oceanic cyclones west of the island of Hawai'i. *Deep-Sea Research Part II*, 2007.

Dickson, B.; Yashayaev, I.; Meincke, J.; Turrell, B.; Dye, S., and Holfort, J. Rapid freshening of the deep North Atlantic Ocean over the past four decades. *Nature*, 416(6883):832–837, 2002.

Eich, M.L.; Merrifield, M.A., and Alford, M.H. Structure and variability of semidiurnal internal tides in Mamala Bay. *J. Geophys. Res.*, 109(C5), 2004.

Emery, W.J. Water types and water masses. *Ocean Circulation*, pages 1556–1567, 2003.

Emery, W.J. and Dewar, J.S. Mean temperature-salinity, salinity-depth, and temperature-depth curves for the North Atlantic and the North Pacific. *Progress in Oceanography*, II(3):219–256, 1982.

Eriksen, C.C.; Osse, T.J.; Light, R.D.; Wen, T.; Lehman, T.W.; Sabin, P.L.; Ballad, J.W., and Chiodi, A.M. Seaglider: A long-range autonomous underwater vehicle for oceanographic research. *IEEE Journal of Oceanic Engineering*, 26 (4):424–436, October 2001.

Fiedler, P.C. and Talley, L. Hydrography of the eastern tropical Pacific: A review. *Progress in Oceanography*, 69:143–180, 2006.

Firing, E. Currents observed north of Oahu during the first five years of HOT. *Deep-Sea Research Part II*, 43(2):281–303, 1996.

Firing, Y.L. and Merrifield, M.A. Extreme sea level events at Hawaii:Influence of mesoscale eddies. *Geophys. Res. Lett.*, 31:L24306, 2004.

Frajka-Williams, E.; Eriksen, C.C.; Rhines, P.B., and Harcourt, R.R. Determining vertical water velocities from Seaglider. *Journal of Atmospheric and Oceanic Technology*, 28:1641–1656, December 2011.

Garau, B.; Ruiz, S.; Zhang, W.G.; Pascual, A.; Heslop, E.; Kerfoot, J., and Tintore, J. Thermal lag correction on Slocum CTD glider data. *Journal of Atmospheric and Oceanic Technology*, 28:1065–1071, September 2011.

Garmin, Inc. Garmin gps 25 lp series. Technical report, 1200 East 151st Street, Olathe, KS 66062, 2000.

Garza, J.A.; Chu, P.; Norton, C.W., and Schroeder, T.A. Changes of the prevailing trade winds over the islands of Hawaii and the North Pacific. *J. Geophys. Res.*, 117, 2012.

Gill, A.E. *Atmosphere-Ocean Dynamics.* Elsevier Academic Press, San Diego, 1982.

Hamilton, J.P.; Singer, J., and Waddell, E. Mamala Bay study, ocean current measurements: A report to the Mamala Bay Commission. Technical report, Sci. Appl. Int. Corp., 1995.

Hatun, H.; Eriksen, C.C., and Rhines, P.B. Buoyant eddies entering the Labrador Sea observed with gliders and altimetry. *J. Phys. Oceanography*, 37:2838–2854, December 2007.

Hautala, S.L. and Roemmich, D.H. Subtropical mode water in the Northeast Pacific Basin. *J. Geophys. Res.*, 103(C6):13055–13066, 1998.

Helland-Hansen, B. Nogen hydrografiske metoder. *Forh. Skand. Naturforskeres*, 16, 1916.

Hosoda, S.; Xie, S.P.; Takeuchi, K., and Nonaka, M. Eastern North Pacific Subtropical Mode Water in a general circulation model: formation mechanism and salinity effects. *J. Geophys. Res.*, 106(C9):19671–19681, 2001.

Jia, Y.; Calil, P.H.R.; Chassignet, E.P.; Metzger, E.J.; Potemra, J.T.; Richards, K.J., and Wallcraft, A.J. Generation of mesoscale eddies in the lee of the Hawaiian Islands. *J. Geophys. Res.*, 116, 2011.

Johnson, G.C.; Toole, J.M., and Larson, N.G. Sensor corrections for Sea-Bird SBE-41CP and SBE-41 CTDs. *J. Atmos. Oceanic Technol.*, 24:1117–1130, 2007.

Jones, C.K.R.T. and Winkler, S. *Handbook of Dynamical Systems III: Towards Applications*, chapter Do invariant manifolds hold water? Elsevier Scientific Pub. Co., New York, 2000.

Kobashi, F. and Kawamura, H. Seasonal variation and instability nature of the North Pacific Subtropical Countercurrent and the Hawaiian Lee Countercurrent. *J. Geophys. Res.*, 107(C11):3185, 2002.

Kundu, P.K. and Cohen, I.M. *Fluid Mechanics*. Elsevier Academic Press, San Diego, 3 edition, 2004.

Latham, R.C. Kauai Channel Currents. Master's thesis, School of Ocean and Earth Sciences and Technology University of Hawaii at Manoa, 1967.

Leonardi, A.P.; Hurlburt, H.E., and O'Brien, J.J. The circulation in the lee of the Hawaiian Archipelago. *Research activities in atmospheric and oceanic modelling*, 8:27–28, 1998.

Letelier, R.M.; Karl, D.M.; Abbott, M.R.; Flament, P.; Freilich, M.; Lukas, R., and Strub, P.T. Role of late winter mesoscale events in the biogeochemical variability of the upper water column of the North Pacific Subtropical Gyre. *J. Geophys. Res.*, 105(28):723–739, 2000.

Levy, M.; Ferrari, R.; Franks, P.; Martin, A.P., and Riviere, P. Bringing physics to life at the submesoscale. *Geophys. Res. Lett.*, 2012.

Locarnini, R.A.; Mishonov, A.V.; Antonov, J.I.; Boyer, T.P.; Garcia, H.E.; Baranova, O.K.; Zweng, M.M., and Johnson, D.R. *World Ocean Atlas 2009, Volume 1: Temerature*. U.S. Government Printing Office, 2010.

Lueck, R.G. and Picklo, J.J. Thermal inertia of conductivity cells: observations with a Sea-Bird cell. *J. Atmos. Oceanic Technol.*, 7:756–768, 1990.

Lukas, R. and Santiago-Mandujano, F. Extreme water mass anomaly observed in the Hawaii Ocean Time-series. *J. Geophys. Res. Lett.*, 28:2931–2934, 2001.

Lukas, R. and Santiago-Mandujano, F. Interannual to interdecadal salinity variations observed near Hawaii. *Oceanography*, 21(1):52–61, 2008.

Lumpkin, C.F. *Eddies and Currents of the Hawaiian Islands*. PhD thesis, University of Hawaii, 1000 Pope Road., Honolulu HI, December 1998.

Lumpkin, R. and Flament, P.J. Extent and energetics of the Hawaiian Lee Countercurrent. *Oceanography*, 26(1):58–65, 2013.

Mamayev, O.I. *Temperature-salinity analysis of world ocean waters*, volume 11 of *Elsevier Oceanography Series*. Elsevier Scientific Pub. Co., Amsterdam, 1975.

Martini, K.I.; Alford, M.H.; Nash, J.D.; Kunze, E., and Merrifield, M.A. Diagnosing a partly standing internal wave in Mamala Bay, Oahu. *Geophys. Res. Lett.*, 34, 2007.

Matthews, D.; Powell, B.S., and Janekovic, I. Analysis of four-dimensional variational state estimation of the Hawaiian Waters. *J. Geophys. Res.*, 117(C03013), 2012.

McCartney, M.S. Subantarctic Mode Water. *A voyage of Discovery*, 24:103–119, 1977.

McDonald, R. The motion of geophysical vortices. *Phil. Trans. R. Soc. Lond.*, 357:3427–3444, 1999.

McGary, J.W. Hawaiian offshore waters Dec. 1949-Nov. 1951. Technical report, Mid-Pacific oceanography. Part VI., U.S. Fish Wildl. Serv. SSRF-152, 1951.

McWilliams, J.C. *Fundamentals of Geophysical Fluid Dynamics*. Cambridge Univ. Press, 2006.

Mensah, V.; Menn, M. Le, and Morel, Y. Thermal mass correction for the evaluation of salinity. *J. Atmos. Oceanic Technol.*, 26:665–672, March 2009.

Merrifield, M.A.; Yang, L., and Luther, D.S. Numerical simulations of a storm-generated island-trapped wave event at the Hawaiian Islands. *J. Geophys. Res.*, 107(C10), 2002.

Mied, R.P. and Lindemann, G.J. Mass transfer between gulf stream rings. *J. Geophys. Res.*, 39:1–29, 1982.

Mitchum, G.T. On using satellite altimetric heights to provide a spatial context for the Hawaii Ocean Time-series measurements. *Deep-Sea Research Part II*, 43:257–280, 1996.

Montgomery, R.B. Water characteristics of Atlantic Ocean and of World Ocean. *Deep-Sea Res.*, 6(2):55, 1958.

Morison, J.; Andersen, R.; Larson, N.; D'Asaro, E., and Boyd, T. The correction for thermal-lag effects in Sea-Bird CTD data. *J. Atmos. Oceanic Technol.*, 11: 1151–1164, 1994.

Mysak, L.A. and Magaard, L. Rossby wave driven eulerian mean flows along non-zonal barriers, with application to the Hawaiian Ridge. *J. Phys. Oceanography*, 13:1716–1725, 1983.

Nencioli, F.; Dickey, T.D.; Kuwahara, V.S.; Bridigare, R.R., and Rii, Y.M. Physical dynamics and biological implications of a mesoscale eddy in the lee of Hawaii:

cyclone Opal observations during E-Flux III. *Deep-Sea Research Part II*, 55: 1252–1274, 2008.

Nof, D. and Simon, L.M. Laboratory experiments on the merging of nonlinear anticyclonic eddies. *J. Phys. Oceanography*, 17:343–357, March 1987.

Nolan, Kellee. Characteristics and water properties of mesoscale eddies in the region of Station ALOHA. Master's thesis, University of Hawaii, 1000 Pope Road., Honolulu HI, August 2008.

Oka, E. and Ando, K. Stability of temperature and conductivity sensors of Argo profiling floats. *J. Oceanogr.*, 60:253–258, 2004.

Patzert, W.C. Eddies in Hawaiian waters. Technical Report 69-8, Hawaii Institute of Geophysics, University of Hawaii, April 1968.

Price, J.M.; Woert, M.L. Van, and Vitousek, M. On the possibility of a ridge current along the Hawaiian Islands. *J. Geophys. Res.*, 99(14):101–111, 1994.

Qiu, B. Seasonal eddy field modulation of the North Pacific Subtropial Counter-current: TOPEX/Poseidon observations and theory. *J. Phys. Oceanography*, 29: 2471–2486, October 1999.

Qiu, B.; Koh, D.A.; Lumpkin, C., and Flament, P. Existance and formation mechanism for the North Hawaii Ridge Current. *J. Phys. Oceanography*, 27: 431–444, 1997.

Roden, G.I. On the subtropical frontal zone north of Hawaii during winter. *J. Phys. Oceanography*, 10:342–362, 1980.

Roden, G.I. Effects of the Hawaiian ridge upon oceanic flow and thermohaline structure. *Deep-Sea Res.*, 38, 1991.

Roemmich, D. and Gilson, J. Eddy transport of heat and thermocline waters in the North Pacific: A key to interannual/decadal climate variability. *J. Phys. Oceanography*, 31:675–687, March 2001.

Rudnick, D.L.; Davis, R.E.; Eriksen, C.C.; Fratantoni, D.M., and Perry, M.J. Underwater gliders for ocean research. *Marine Technology Society Journal*, 38 (1):48–59, 2004.

Sanderson, M. *Prevailing Trade winds: Climate and weather in Hawaii*. University of Hawaii Press, 1993.

Seckel, G.R. Vertical sections of temperature and salinity in the Trade Wind Zone of the Central North Pacific, February 1964 to June 1965. Technical report, United States Department of the Interior, U.S. Fish and Wildlife Service, Bureau of Commercial Fisheries, 1969.

Shchepetkin, A.F. and McWilliams, J.C. Correction and commentary for "Ocean forecasting in terrain-following coordinates: Formulation and skill assessment of the Regional Ocean Modeling System". *J. Comput. Phys.*, 228:8985–9000, 2009.

Shimizu, Y.; Iwao, T.; Yasuda, I.; Ito, S.; Watanabe, T.; Uehara, K.; Shikama, N., and Nakano, T. Formation process of North Pacific intermediate water revealed by profiling floats set to drift on 26.7 sigmatheta isopycnal surface. *J. Oceanogr.*, 60:453–462, 2004.

Stommel, H. On the cause of the temperature-salinity curve in the ocean. *Geophysics*, 48:764–766, March 1962.

Stommel, Henry. The Slocum Mission. *Oceanography*, 2(1):22–25, April 1989.

Suga, T.; Kato, A., and Hanawa, K. North pacific tropical water: Its climatology and temporal changes associated with the climate regime shift in the 1970s. *Progress in Oceanography*, 47:223–256, 2000.

Sverdrup, H.U.; Johnson, M.W., and Fleming, R.H. *The oceans, their physics, cheistry and general biology*. Prentice Hall, New York, 1947.

Talley, L.; Nagata, Y.; Fujimura, M.; Kono, T.; Inagake, D.; Hirai, M., and Okuda, K. North Pacific intermediate water in the Kuroshio/Oyashio mixed water region. *J. Phys. Oceanography*, 25:475–501, 1995.

Talley, L.D. Salinity patterns in the ocean. In MacCracken, M.C. and Perry, J.S., editors, *Encyclopedia of Global Enviromental Change*, volume 1, The Earth system: physical and chemical dimensions of global environmental change, pages 629–640. John Wiley & Sons, 2002.

Talley, L.D. and de Szoeke, R.A. Spatial Fluctuations north of the Hawaiian Ridge. *J. Phys. Oceanography*, 16:981–984, 1986.

Thomas, L.N.; Tandon, A., and Mahadevan, A. Submesoscale processes and dynamics. *Ocean Modelling in an Eddying Regime*, 177, 2008.

Tomczak, M. and Godfrey, J.S. *Regional Oceanography: An Introduction.* Pergamon, 1994.

Toner, M.; Kirwan, A.D.; Poje, A.C.; Kantha, L.H., and Muller-Karger, F.E. Chlorophyll dispersal by eddy-eddy interactions in the Gulf of Mexico. *J. Geophys. Res.*, 108(C4), 2003.

Tropea, C.; Yarin, A.L., and Foss, J.F. *Springer handbook of experimental fluid mechanics*, volume 1. Springer Science and Business Media, 2007.

Trujillo, A.C. Castillo. Wind driven currents south of Oahu. Master's thesis, University of Hawaii, 1000 Pope Road., Honolulu HI, June 2014.

Uffelen, L.J. Van; Nosal, E.M.; Howe, B.M.; Carter, G.S.; Worcester, P.F.; Dzieciuch, M.A.; Heaney, K.D.; Campbell, R.L., and Cross, P.S. Estimating uncertainty in subsurface glider position using transmissions from fixed acoustic tomography sources. *J. Acoust. Soc. Am.*, 134(4):3260–71, October 2013.

Vine, D.M. Le; Lagerloef, G.S.E.; Colomb, F.R.; Yueh, S.H., and Pellerano, F.A. Aquarius: An instrument to monitor sea surface salinity from space. *Geoscience and Remote Sensing*, 45(7), 2007.

White, W. A narrow boundary current along the eastern side of the Hawaiian Ridge; the North Hawaiian Ridge Current. *J. Phys. Oceanography*, 13:1726–1731, 1983.

Wust, G. Meridionale schichtung und tiefenzirkulation in den westhalfen der drei ozeane. *J. Cons. Int. I'Explor. Mer*, 5:7–21, 1930.

Wyrtki, K. Fluctuations of the dynamic topography in the Pacific Ocean. *J. Phys. Oceanography*, 5(3):450–459, 1975.

Wyrtki, K. *Water masses in the oceans and adjacent seas*, volume International Dictionary of Geophysics. Pergamon Press, 1977.

Wyrtki, K. Eddies in the Pacific North Equatorial Current. *J. Phys. Oceanography*, 12:746–749, July 1982.

Xie, S.; Liu, W.T.; Liu, Q., and Nonaka, M. Far-reaching effects of the Hawaiian Islands on the Pacific ocean-atmosphere system. *Science*, 292:2057–2060, 2001.

Yoshida, S.; Qiu, B., and Hacker, P. Wind-generated eddy characteristics in the lee of the island of Hawaii. *J. Geophys. Res.*, 115, 2010.

Yoshida, S.; Qiu, B., and Hacker, P. Low-frequency eddy modulations in the Hawaiian Lee Countercurrent: Observations and connection to the Pacific Decadal Oscillation. *J. Geophys. Res.*, 116, 2011.

Yu, Z.; Maximenko, N.; Xie, S., and Nonaka, M. On the termination of the Hawaiian Lee Countercurrent. *Geophys. Res. Lett.*, 30:2015, 2003.

Yuan, X. and Talley, L.D. Shallow salinity minima in the North Pacific. *J. Phys. Oceanography*, 22, 1992.